MICROSTRUCTURAL EVOLUTION AND PHYSICAL BEHAVIOR OF A LITHIUM DISILICATE GLASS-CERAMIC

Wen Lien

Submitted to the faculty of the University Graduate School
in partial fulfillment of the requirements
for the degree
Master of Science
in the School of Dentistry,
Indiana University

May 2014

Accepted by the Graduate Faculty, Indiana University, in partial fulfillment of the requirements for the degree of Master of Science.

Master's Thesis Committee

Tien-Min G. Chu, D.D.S., Ph.D., Chair

Jeffrey A. Platt, D.D.S, M.S.

John A. Levon, D.D.S, M.S.

David T. Brown, D.D.S., M.S.

Dong Xie, Ph.D.

ACKNOWLEDGEMENTS

I believe that **God** predestined everything, and none of us got to where we are today alone. Specifically, for the past 19 months, my training in the field of dental materials at the Indiana University, School of Dentistry, have been professionally very rewarding, and this thesis would not has been possible without the help, support, and patience of my thesis advisor, **Professor Chu**. Thank you, **Dr. Chu**, for allowing me the opportunity to work with you, for permitting me the freedom to express my own individuality, and for providing me a challenging environment to foster creative learning. I appreciate all your time, ideas, and teaching to make my learning experience stimulating. Most importantly, I thank you for your friendship!

Throughout my training, dozens of people have taught me immensely. My gratitude goes to **Professor Platt**; your dedication in dental materials and occasionally humorous musings bring me joy and inspire me to continue asking questions. Also, thank you, **Professor Bottino**, for your assistance in my research; your suggestions have been invaluable. Furthermore, on many occasions, your mere presence in the lab have saved me valuable time since I do not have a key and always require someone to open the lab door – or to the grad-student break room or to the printer room. To **Mrs. Aranjo**, thank you for the courtesies extended to me and for providing a warm and welcome atmosphere. In addition, I would like to thank my committee members, **Professor Levon**, **Professor Brown**, and **Professor Xie**, for reading and commenting on my thesis.

I am especially grateful for **Colonel (Dr.) Roberts**; the differential-scanning-calorimetry and x-ray diffraction parts of this thesis would not have been possible without the help from **Dr. Roberts**. Sir, thank you so much for "going above and beyond" to help me gather data for my thesis – I can't thank you enough for your willingness to support me. Also, I extend my sincerest

appreciations to my mentor and dear friend, **Colonel (Dr.) Vandewalle**, for all his guidance, professional support, and advice as well as friendship! Furthermore, I would like to thank **Dr. You** and **Lieutenant Colonel (Dr.) Lincoln** for their help on the scanning electron microscopy images.

I would also like to express my gratitude to **Professor Jettpace** for her wonderful help in proofreading my thesis.

With countless people teaching and helping me every step, a special group from the Air Force Research Laboratory's Materials and Manufacturing Directorate deserves singularly distinctive recognition. Thank you, **Dr. Campbell**, **Dr. Ehlert**, and **Dr. Anderson** for letting me use the nanoindenter – I will never forget your warm hospitality and generosity.

Unquestionably, throughout my life's journey, I will be forever indebted to my **wife**, **daughter**, and **parents** for their love, support, and patience.

Last but not least, I've finally discovered – sadly wasn't any sooner – that what really got me through the deepest and darkest times in my life journey was just a prayer away, for there is a lot of difference between just saying prayers and actually praying to **God** for a moment, and then, I would be in touch with **Him** all day.

Table of Contents

List of Tables

List of Figures

1. Introduction

1.1. Past and present of glass-ceramics

What is it about studying ceramics and glass that make them so attractive? Even though glass-ceramic materials have been known to most cultures since earliest times, the advancement in glass-ceramic technology has never ceased. Glass-ceramic research has been and continues to be an indicator for human progress. Although glass-ceramics have led to a multitude of benefits that affect human lives, often the importance of glass-ceramics has been underestimated since some of these benefits are embodied in mere conveniences of a relatively trivial sort. For example, one could not help but conjure thoughts of their classical usages like potteries, stained-glass windows, or simply decorations. Today, apart from the centuries-old crudeness of the glass-ceramic technology and the imagery of the men who used such tools, glass-ceramics are a diverse and thriving sector that overlaps with many industries, spanning from advanced manufacturing to renewable engineering and from medical biotechnology to clinical dentistry.

Modern glass-ceramics encompass both traditional and advanced glass-ceramics [1]. The traditional glass-ceramics are generally derived from common, naturally occurring raw materials like clay minerals, quartz sands, and silicate glasses, which are then made into familiar, domestic products such as tableware, bricks, tiles, refractories, and cements through industrial processes that have been practiced for centuries. The advanced glass-ceramics consist of carbides, oxides, nitrides, and non-silicate glasses (e.g., alumina or zirconia), whose applications come in many new façades like the electrical-thermal insulators, lightweight armors, aerospace frameworks, and biomimetic composites. However, many of the most pressing materials' problems that we face today are driven by the demands placed on performance. How can we design a glass-ceramic that balances the scale between the intrinsic limits of its engineering tolerance and our application needs, such that our glass-ceramics are able to resist the environmental challenges put forth by humanity or nature?

1.2. Defining modern glass-ceramics

What is a glass-ceramic and how is it different than a glass? In this thesis, a glass-ceramic is defined as an inorganic, nonmetallic, silica-based, matter derived from the manipulation of a glass-based solidified melt. The solidified melt is capable of evolving into a variety of microstructural configurations. Whether the solidified melt remains a glass or becomes a glass-ceramic depends on tailoring its intrinsic chemical composition and imposed thermal treatment. Glass-ceramic development can be generalized in three steps. First, a unique formulation of glass powders and frits is thermally processed to produce a melt. Second, a glass-forming step is executed by quenching the melt in a mold to allow creation of complex designs. Third, the solidified glass precursor undergoes "controlled-crystallization" heat treatments in which the precipitations of crystalline or polycrystalline structures within the solidified melt is modulated by the thermodynamic interaction between the molecular kinetics of the glass and the action of heat, pressure, and subsequent cooling. Furthermore, the genesis of a glass-ceramic is predicated on the addition of nucleating agents, whose function is to reduce the energy barrier of crystalline formation and to act as perturbations for initiating controlled crystallization and for seeding the glassy network with nuclei for subsequent epitaxy. Therefore, the process of forming a crystalline network within a glassy matrix depends on how the amorphous nature of glass is able to compositionally segregate into an ordered molecular arrangement.

1.3. Glass and glass-ceramic comparison

A glass differs from a glass-ceramic by means of its molecular and microstructural configuration. Depending upon the degree of the atomic or molecular ordering, a solidified melt may be comprised solely of an amorphous entity (e.g., glass) or evolve into a partially crystalline structure interspersed with residual glasses (e.g., glass-ceramic). A glass also differs from a ceramic (synonymous with ceramic composite in some literatures) in which the ceramic contains practically 99% singly- or poly-crystalline conformation such as Yttria Stabilized Zirconia (3Y-TZP) [2]. Here, the terms, "amorphous" and "glass", are synonymous and describe nature's way of preserving a frozen image of the melt's structure. By definition, glass is the product of a super cooled liquid, whose atomic arrangement is random and lacks translational symmetry. Because of this atomic disorder and asymmetry, the bond energies, coupling from one atom to another slightly vary when contrasting with the fixed or matching bond energies within an ideal crystal; therefore, during thermal breakdown, a glass solid typically displays a gradual softening into a liquid (glass-transition) rather than having a strict melting point. Additionally, all glasses exhibit a transformation behavior that depends on temperature and pressure. In contrast, glass-ceramics are composed of medium to high percentages of crystals, which are known for their medium- and long-range atomic ordering and predictable symmetry.

To understand why some glasses desire to form crystals but fail to crystallize while other solidified melts crystallize with ease and without vitrification, it is necessary to consider the thermodynamics of glass. Under rapid quenching, the immediate reduction of thermal and radiant energies causes the average translational kinetic energy associated with the disorder motion of silica atoms to decline. This phenomenon not only augments the restriction and localization of silica atoms but also supplant the externally disruptive thermal forces by the interatomic attractive forces between the silica atoms since the forces of interatomic attraction are slowly exceeding the externally disruptive thermal forces. From a thermodynamic perspective, the energy and vibration of the silica atoms is now confined within the local minimum of its respective potential well, creating a barrier that must be overcome in order for the atoms to move amongst each other, thereby “jamming” the silica atoms in a disordered fashion and preventing the melt from forming a regular lattice. If a melt is to avoid crystallization, the rate of cooling and its structural relaxation needs to be relatively faster than its rate of compositional segregation. Furthermore, if viscous flow under shear forces is present in the melt, the probability of vitrification is increased since the mobility and collisional reactivity of atoms and molecules are impeded through the action of densification by viscous sintering. Therefore, controlling the thermal treatments of a glass allows greater flexibility to modulate its microstructure and physical properties.

1.4. Dental glass-ceramics

In dentistry, modern glass-ceramic fixed dental prostheses (FDPs) utilize the advantages derived from combining properties of crystalline ceramics with those of glasses to restore structural support, protection, and physical integrity to enamel, dentin, and pulpal tissues. They play a critical role in oral rehabilitation while bridging the chasm between synthetic and naturalistic aesthetics. Unlike polymer-based restorations, for which hydrolysis, oxidation, and leachable monomers are a concern, glass-ceramics are chemically and thermally oxidized, forming stable hydroxide- and oxide-based compounds. Under *in vivo* environments, they have greater corrosive and microbial resistance, better biocompatibility, much higher melting points, and higher yield strengths than most polymeric restorations [2]. Although glass-ceramics tend to be brittle with no inherent ability for plastic deformation when subject to tensile stresses, they have the capacity for withstanding high compressive stresses. Typically, they demonstrate greater elastic modulus and less thermal expansion under oral conditions than most metal alloys. More importantly, glass-ceramics provide excellent aesthetic results relative to polymer and metal restorations. Because of these benefits, glass-ceramics are highly favored for many dental applications.

1.5. Classification of dental glass-ceramics

Current fixed dental prostheses (FDP) can be divided into three main types of restorations: (1) all-metal, (2) metal-ceramic, and (3) all-ceramic [2]. See Figure 1. The all-ceramic FDPs can be further classified according to either of the two attributes, (a) microstructural phases or (b) fabricating techniques [2]. Based on the ratio of glassy-to-crystalline components, the "microstructural phases" attribute can be subcategorized into three groups: (i) predominantly glass-based, (ii) glassy-crystalline, and (iii) polycrystalline [3]. For the "fabricating techniques" attribute, it can be subcategorized into the following groups: (i) powder-liquid condensation, (ii) slip casting, (iii) heat-pressed, and (iv) CAD-CAM machined [4, 5]. See Figure 2. Because of the ever-evolving ceramic innovations, these classifications by no means remain stagnant.

1.6. Microstructural phases

1.6.1. The predominantly glass-based group

A predominantly glass-based system typically exhibits greater than 50% of amorphous, glassy network [3]. The two most popular vitreous networks in the predominantly glass-based group are silicate and aluminosilicate liquids, and both can be derived from the melt of silicate [SiO_2], alumina [Al_2O_3], and feldspathic minerals [$X_nAlSi_3O_8$, where X can be sodium (Na), calcium (Ca), or potassium (K)], which surprisingly are the three most abundant minerals found in the earth's crust. Even though the atomic-scale structures for most glasses are still a mystery, the atomic-scale structure for silicates or aluminosilicates is thought to be well-understood. Today, the widely accepted atomic-scale structure for these two melts originates from the continuous network theory of glasses postulated by Zachariasen [6].

The silicate melt contains silicon and oxygen ions, and its basic building block is the silicon-oxygen tetrahedron, where the silicon ion is positioned at the center of the tetrahedron and is bonded to four oxygen ions, located at the four corners of the tetrahedron. Each tetrahedron is "cross-linked" by bridging oxygen ions to form a long-range order of tetrahedral network. In the presence of network-modifying cations (Na^+, Ca^{2+}, and K^+), the ionic forces of the cations break the bridging oxygen ions and form non-bridging oxygen ions. Because of this, the long-range-ordered silicate network is depolymerized into random clusters of short-range-ordered and medium-range-ordered structures. In this thesis, a long-range-ordered network is defined as a crystalline solid, whose atomic arrangement shows periodicity and translational symmetry. The modifying ions can also lower the glass transition temperature and alter the thermal expansion or contraction behavior of the network. An example of a long-range-ordered silicate network is crystalline silicates or quartz, and a silicate network composed of random short-range-ordered clusters is an amorphous glass. Other polymorphs of silicates include cristobalite or tridymite.

The aluminosilicates are solidified melts that contain silicon and aluminum ions tetrahedrally coordinated by the oxygen ions to form a three-dimensional (3D) network. Specifically, the aluminum-oxygen or silicon-oxygen tetrahedrons serve as the basic building blocks of the aluminosilicate network. Unlike the silicon ions, the aluminum ions like to have a coordination number of six and tend to be bonded to six oxygen ions in an octahedral fashion.

The aluminum ion plays a double role. It can substitute for the silicon ion in the tetrahedron. Or, the aluminum ion can function as an independent cation, serving as a network modifier that can reduce the number of network crosslinks and can decrease viscosity by producing non-bridging oxygen ions. If the aluminum ion is to be a substitute of the silicon ion, for every Si^{4+} that is replaced by an Al^{3+} in a tetrahedron, the charge is balanced by the modifying cations such as Na^{+}, Ca^{2+}, and K^{+} ions. The 3D network of aluminosilicates is formed by linking the tetrahedra to each other or to an octahedron via a bridging oxygen ion. After solidification, the aluminosilicate melt can be amorphous or crystalline. An example of a crystalline aluminosilicate is feldspar, and an aluminosilicate network composed of random short-range-ordered clusters is an analogue of amorphous glass. However, in dentistry, feldspathic porcelain is defined as an amorphous aluminosilicate network that is interspersed with feldspar or leucite crystals and is classified as a predominantly glass-based structure [3]. The major advantage of a “predominantly glass-based” prosthesis like feldspathic porcelain is its inherent translucency and enamel-like luster, but its disadvantage is its strength, which is much weaker than the glassy-crystalline or polycrystalline restorations.

1.6.2. The glassy-crystalline group

The glassy-crystalline group consists of a wide variety of glass-ceramic systems: binary [e.g., $Li_2O\text{-}SiO_2$ or $Li_2O\text{-}2SiO_2$], ternary [e.g., $Li_2O\text{-}Al_2O_3\text{-}nSiO_2$ (LAS-System), $MgO\text{-}Al_2O_3\text{-}nSiO_2$ (MAS-System), or $ZnO\text{-}Al_2O_3\text{-}nSiO_2$ (ZAS-System)], and multicomponent [e.g., IPS e.max® Press and IPS e.max® CAD; Ivoclar Vivadent, Schaan, Liechtenstein]. Among the three systems, binary and ternary are the most thoroughly studied systems because of their simplicity and practicality. These glass-ceramic systems exhibit a glass-to-crystal ratio that ranges from 50% to 70% volume fraction of crystallinity [7]. The production of a glass-ceramic is complicated by the inclusion of a crystalline phase. As mentioned in the earlier section, glass-ceramic fabrication can be achieved starting by the preparation of a monolithic glass with appropriate base composition, followed by a glass-forming step to allow processing of complex shapes, and then treated by controlled crystallization. The most popular controlled-crystallization system that is commercially available for dental application is the lithium disilicate glass-ceramic. Alternatively, another way to produce a glass-ceramic is by using the method of dispersion-strengthening, a technique similar to making polymer-based composites, where crystalline fillers are added to the glassy matrix to enhance the physical properties and to fine-tune the translucency or opacity of the FDP [7]. The most common particulates used for dispersion-strengthening reinforcement are the feldspar and leucite crystals (e.g., Vitablocs® Mark II, Vident, Brea, California, USA). In this thesis, the glassy-crystalline group consists of glass-ceramics that are fabricated only by the method of controlled crystallization. This is because the percentage of crystallinity made by the dispersion-strengthening method is typically less than 50%, which is considered as a predominantly glass-based structure.

The idea behind dispersion-strengthening or controlled crystallization is to resist crack advancement and ultimately to stop fracture. Although the actual mechanism of fracture for metals, glass, or glass-ceramics is distinctly different, it is generally perceived that the crack advancement can be restrained by toughening the material through compositional or microstructural modifications. For example, for a metal, prior to its fracture or fatigue failure, its macroscopic deformation is related to its microscopic dislocation plasticity. If dislocation motion or slip processes were hindered, metal materials would be brittle, resulting in metal strengthening. On the other hand, unlike a metal, a glass having a random and non-periodic arrangement of atoms, has neither dislocations nor slip systems. Furthermore, for a glass with a homogeneous phase, its microstructure lacks the stress-relieving characteristics such as grains or grain boundaries. Because of this, glass exhibits a low tolerance for flaws, resulting in the same aforementioned phenomenon as in metal strengthening – brittleness without plasticity.

At room temperature, the glass strength is very much dependent on the intrinsic number of flaws, cracks, or porosities. And, several ways to prevent glass from fracture involve reducing flaws, minimizing crack growth, and hindering porous plasticity. Most importantly, controlling the evolution of grain sizes and grain boundaries, while a glass is being transformed into a glass-ceramic, plays a key role in crack tip shielding. Past studies have shown that either by inducing growth or by inclusion of crystalline grains into the glassy matrix, the grain boundaries can act as crack "pinning agents" since the atomic-scale asymmetry within a grain-boundary region can contribute to the discontinuity of crack growth from one grain to another, thereby strengthening the glass-ceramic [8-10]. Theoretically, the mean-free-path distance between the grains dictates the crack-crystallite interactions. Whether a crack can be pinned or deflected depends on its size relative to the mean-free-path distance. Pinning a crack by the crystalline phase is more effective when the crack size is approximately equal to the mean-free-path distance between the grains. While at larger crack sizes, a grain can act as a barrier, either resulting in crack deflection around the grains or crack propagation through the grains, which altogether requires a large amount of stress. As an unwritten rule, the strength of a glass-ceramic is increased when the mean-free-path distance between grains is decreased relative to the crack size. Alternatively, according to the Hall-Petch equation,

$$\sigma_y = \sigma_0 + k_y d^{-\frac{1}{2}}$$

(where σ_y is the yield stress; σ_0 is a materials constant for the starting stress for dislocation movement; k_y is a constant that is unique to each material; and d is the average grain diameter), the strength of a fine-grained glass-ceramic is higher than a coarse-grained since greater numbers of grain boundaries are found in the fine-grained glass-ceramic, which can help to impede crack motion. However, the Hall-Petch equation no longer holds true when the grain size reaches below ten nanometers. Since nano-scale grains are small enough to act as a collective unit, each grain can start to slip and slide amongst one another, generating slip processes like in the case of a metal.

1.6.3. The polycrystalline group

A polycrystalline ceramic or using the aforementioned terminology, ceramic composite, typically exhibits a 95-99% volume fraction of crystallinity [4]. The conventional view of a polycrystalline-ceramic microstructure is a multiplicity of randomly oriented crystals joined at grain boundaries. These random geometrical orientations and size of the polycrystalline grains play an important role in how a crack propagates and whether the fracture deviates along the grain boundary (inter-granular) or continues through the grain (trans-granular). For example, when the grains within a polycrystalline ceramic happen to be in a favorable orientation for cleavage, the cleavage energy of fracture is at its minimum. Furthermore, since the atomic-scale structure of the grain boundaries can be readily disturbed by interaction with cracks, flaws, porosities, and external fields such as temperature and pressure, a slight variation in the atomistic level of structural order at the grain boundaries can strongly affect crack motion and fracture properties. Despite the complexity of fracture phenomena in poly-crystals, the strength and toughness of the polycrystalline ceramics tends to be better than glasses and glass-ceramics.

With the development of Computer-Aided Design and Computer-Aided Manufacturing, considerable interest in the dental community has piqued in these polycrystalline ceramics for the possible application as posterior FDPs. In addition, recent laboratory and clinical studies have shown promising outcomes for strength, durability, and survival rates [10-12]. However, the advantages of polycrystalline ceramics also come with distinct disadvantages. One major disadvantage is the lack of a glassy phase within the polycrystalline network, which can impair the effectiveness of conventional adhesive luting procedures. Furthermore, as aesthetics become increasingly paramount, the opacity of polycrystalline ceramics can affect the optical translucency, resulting in less than optimal aesthetics. To compensate for this, it has become routine that polycrystalline ceramics are used as core ceramics for veneering with compatible feldspathic porcelain. By doing this, an all-ceramic crown combines the strength of a polycrystalline core with the aesthetics of feldspathic porcelain, but the limited bonding strength exhibited at the interfacial surfaces between polycrystalline substrate, veneering ceramic, or a tooth remain a challenge. Other shortcomings include abrasiveness to the opposing natural dentition. The most popular polycrystalline compositions are alumina, zirconia, and titanium (e.g., Procera™ Alumina, Procera™ Zirconia, and Procera™ Titanium; Nobel Biocare, Zurich, Switzerland).

1.7. Fabricating techniques

1.7.1. Powder-liquid condensation

For years, the use of powder-liquid condensation has been the simplest, most direct, and economical method for layering and veneering dental porcelain. First, the glass-ceramic powders are converted into slips using a diluting agent. Then, custom layering and stacking of the dental porcelain involve the application of these slips, one coating at a time, by using a sculpturing blade or brush while carefully crafting the tooth anatomy. Finally, the stacked porcelain is dried and thermally treated. The key to a quality prosthesis is to maintain proper moisture level and liquid-to-powder ratio so that the packing of the powder particulates remains dense and compact. This method requires not only the technical know-how but also appropriate experiences along with a touch of artistry to succeed. Because the stacked porcelain is artistically crafted and contains feldspar-based silicate glass with minimal crystalline fillers, its appearance and optical translucency deliver excellent aesthetics for custom veneers. However, the porosity profile of the manually stacked porcelain typically shows a high degree of variability, which can impact the strength and toughness of the restoration.

1.7.2. Slip cast

The process of slip casting uses both ceramic slips and glasses. It involves a two-stage heat-treatment. The slips are a liquid suspension of ceramic particles and behave like hydrocolloids for which imbibition, syneresis, and flocculants can change their physical properties. To control the slips' pH, rheology, and osmotic equilibrium, other ingredients such as pH modifiers, binders, and deflocculants are added to prevent alkaline pH interaction, to preserve slips' viscosity, and to avoid leaching of ceramic colloids from the suspension respectively. Besides their principal application in slip casting, slips can also be used when making pressed mixes. In slip casting, the slips are poured into a mold that is designed to absorb water; the mold is contoured to match the desired shape or "jacket" of the master die, which is a perfect replica of the prepared tooth or implant abutment readied for a FDP. After the water from the slips is sodden through the mold's walls, a thin coating of the ceramic particles is condensed tightly against the mold, creating a ceramic skeleton. Next, this "green" skeleton is dried and prepared for its first thermal treatment, where sintering of the ceramic particles takes place. The design of the resultant product is anticipated to be a porous microstructure so that it can be infiltrated by molten glass. Subsequently, following a second firing schedule in which the molten glass penetrates into the porous framework via capillary action, the ceramic skeleton is interlaced with the glassy matrix to form the core of the dental prosthesis. Like the metal framework, feldspathic porcelain can be stacked and glazed onto the glass-ceramic core for its final finish. The glass-infiltrated ceramic cores typically exhibit higher fracture resistance and strength than those fabricated by powder-liquid condensation due to the cores' high polycrystalline contents in their skeleton and less man-made variability.

1.7.3. Heat-pressed

The heat-pressed process is similar to the lost-wax casting method, consisting of designing, investing, burnout, and casting (pressing). In the designing stage, a wax model of the desired FDP is sculptured. Following spruing, the wax model is encased or "invested" in a mold, typically made of gypsum materials. Then, the mold is heated upside-down, and the wax is "lost" or "burnt-out", leaving behind a cavity. Finally in the pressing stage, instead of using metal, glass-ceramic ingot is heated, softened, and pressed or injected into the mold's cavity. The resultant product can be finished either with the staining or cut-back techniques. In the staining technique, the pressed restoration is finished first by the application of stains and glazing materials and followed by characterization firing. In the cut-back technique, the pressed restoration is trimmed, veneered, stained, and glazed to create the illusion of optical translucency and anatomical realism like incisal mamelons.

1.7.4. Computer-Aided Design and Computer-Aided Manufacturing (CAD-CAM)

For this work, we concentrated on studying the physical and kinetic properties of an all-ceramic system made of lithium disilicate glass-ceramic material that is specifically designed for CAD-CAM. The details of the CAD-CAM techniques are discussed in the following sections.

2. Lithium disilicate glass-ceramics

2.1. Background of lithium disilicate glass-ceramics

The most widely used ingredients found in numerous dental glass-ceramics are silicate [$(SiO_4)^{4-}$] and leucite [$KAlSi_2O_6$] crystals, whose growth is often induced within a feldspar-based silicate glass [(Na or K)$AlSi_3O_8$] through the process of devitrification [13]. Besides using leucites as the predominant crystals for fine-tuning thermal expansion, strength reinforcement, and optical enrichment, incorporation of alternative inorganic ingredients like lithium disilicate [$Li_2Si_2O_5$ or Li_2O-$2SiO_2$] and oxide-based compounds (e.g., magnesium oxide, aluminum oxide, or zirconium oxide) into glass precursors is rapidly gaining acceptance as the standard of care [4, 14]. These newer generations of glass-ceramics are differentiated from the feldspar-leucite glass-ceramics by their elevated strength, increased processing temperatures, improved toughness, and tailored properties for milling machines [2, 15, 16]. An example of such a system is IPS e.max® CAD (Ivoclar Vivadent, Schaan, Liechtenstein), a lithium disilicate based glass-ceramic that is intended for CAD-CAM processing. In many cases, lithium disilicate glass-ceramics have exhibited better physical performance than the traditional feldspar-leucite glass-ceramics [15, 17, 18]. These improved properties of lithium disilicate glass-ceramic are likely related to its robust multiphasic composition [19].

2.2. Clinical performance of lithium disilicate glass-ceramics

According to a recent review, the failure rate of single-unit crowns made from lithium disilicate glass-ceramics (i.e., IPS Empress® 2 and IPS e.max® Press; Ivoclar Vivadent, Schaan, Liechtenstein) was reported to be less than 5% at 5 years [20]. Also for the three-unit lithium-disilicate FDPs, the 10-year survival result was 87.9% and was found to demonstrate acceptable longevity as compared with the conventional metal-ceramic gold standards, which usually have a survival rate of 89% [21, 22]. When tooth location was considered, survival rates for both anterior and posterior crowns that were restored with lithium disilicate glass-ceramics were shown to be competitively similar – with only slightly greater success for posterior than anterior crowns [23]. Furthermore, a recent 9-year prospective study found no significant difference in survival rate between anterior and posterior crowns made of lithium-disilicate glass-ceramics [24]. However, crowns restored with feldspar-leucite glass-ceramics showed a greater success for anterior than posterior locations [20]. In general, the most common complications associated with the glass-ceramic FDPs involved: tooth or glass-ceramic fracture, loss of retention, secondary caries, and the need for endodontic treatment [21].

2.3. Materials science of lithium disilicate glass-ceramics

2.3.1. Lithium disilicate glass-ceramics for dentistry

Lithium disilicate glass-ceramics were first introduced into the dental community in 1998 by Ivoclar Vivadent. Since its inception, dental research on the lithium disilicate glass-ceramics have been based on the commercial product, IPS Empress® 2 (Ivoclar Vivadent, Schaan, Liechtenstein). It contained approximately 65% volume fraction of lithium disilicates, 34% volume fraction of residual glass, and 1% volume fraction of porosity after heat treatments [15]. Unlike the binary lithium disilicate system that was first developed by Stookey (1959) [25], the IPS Empress® 2 was derived from a multi-component system, formulated from SiO_2-Li_2O-K_2O-ZnO-Al_2O_3-La_2O_3-P_2O_5 compositions [13, 26]. Scanning electron micrographs of IPS Empress® 2 revealed that the microstructures of lithium disilicates were elongated crystals with a mean grain length and diameter of 5.2 µm and 0.8 µm respectively [15]. In contrast to IPS Classic®, for which uncontrolled devitrification of leucites occurred only on the surface [27, 28], the controlled crystallization of IPS Empress® 2 ensured that nucleation and crystal growth of lithium disilicates propagated uniformly throughout the bulk structure during heat treatments [26, 28]. The nucleation in IPS Empress® 2 was achieved with the aid of special additives (e.g., P_2O_5, TiO_2 and ZrO_2) [29, 30]. Additionally, these additives could alter the eutectic composition and temperature of the IPS Empress® 2 glass-ceramic [31]. According to Headley and Loehman (1984), at low temperature, P_2O_5 amassed and formed the crystalline nuclei of lithium orthophosphates. Then, lithium metasilicates, lithium disilicates, and cristobalites could be crystallized by epitaxial growth on those lithium orthophosphates [32].

2.3.2. The effect of thermal treatment on lithium dislicates

Besides the special additives, the growth of lithium disilicate crystals could also be affected by a one- or two-stage heating schedule. The one-stage heating schedule only involved a single heating rate and holding time. The two-stage heating schedule typically entailed first and second heat treatments for nucleation then crystallization respectively [29, 33]. The initial heat-treatment stage was important to establish a kinetically favorable setting for stabilizing lithium metasilicates [33]. The second heat-treatment stage, usually at a higher temperature range than the initial, supplied the thermal energy to induce growth of lithium disilicates and to thermodynamically destabilize the lithium metasilicates [33]. According to Borom et al. (1975), the growth of lithium disilicate crystals was not dependent on the crystalline nuclei of lithium metasilicates [33]. Rather, lithium metasilicates kinetically competed with lithium disilicates but slowly diminished since it was thermodynamically less stable than lithium disilicates at high temperatures [33]. In contrast, Zheng et al. (2008) suggested an interdependence between lithium metasilicates and lithium disilicates, where lithium disilicates could be epitaxially grown on lithium metasilicates [29]. Past investigations have argued that a two-stage heating schedule precipitated more and larger lithium disilicate crystals than a single-stage heating schedule [29, 33, 34]. Even though the single-stage heating schedule might require less overall processing time, it tended to lack the appropriate thermal enrichment for maturation of lithium disilicate crystals [29, 34]. Because of this, phase separations between lithium metasilicates and lithium disilicates were less distinguishable amidst the glass-ceramic microstructures for the single-stage heating schedule that encourages a fast or ultrafast heating rate.

2.3.3. CAD-CAM lithium disilicate glass-ceramics (IPS e.max® CAD)

With the advent of CAD-CAM technology, newer generations of glass-ceramic blocs were introduced to accommodate the ease of milling, to maximize cutting efficiency, and to prolong the life of the milling tools. Today, the insertion of a chair-side IPS e.max® CAD prosthesis involves three fabricating progressions: industrial casting of the blocs, CAD milling, and final thermal refinement for enriching lithium disilicate crystallization. First, according to the manufacturer, glass compositions (mainly SiO_2, Li_2O, P_2O_5, ZrO_2, ZnO, and K_2O) are incongruently melted, quenched, and annealed to form blue ingots, IPS e.max® CAD blocs [35]. The blue tint, acquired from the added colorants, is evidence that the bloc has undertaken a partially glassy-crystalline transformation and signifies its readiness for the second process, CAD milling. In this partially crystallized state, these intermediates inherit a mild to moderate strength and hardness, which can be easily machined by any popular CAD-CAM system. Often, this second process can be conveniently done in a private dental practice. After milling, it is then transformed by a two-stage heat treatment into a dental prosthesis containing both glassy phase and lithium disilicate crystals. Different heating parameters can upset the driving force for growing lithium disilicates and can alter the overall percentage of residual glasses [15-19, 33]. Theoretically, glass-ceramic prostheses, containing an extra residual glassy phase, are more likely to adversely impact a number of properties including load-bearing capacity, resistance to acidic attacks, and fracture toughness [30]. In contrast, amplifying crystallization lowers the coefficient of thermal expansion, improves the resistance to thermal shock, and increases prosthetic strength [30, 36, 37].

2.3.4. Current challenges

Although many studies have been conducted to evaluate the clinical performance and potential shortcomings of lithium disilicate glass-ceramics in comparison to other popular types of dental materials, only a few focus on the glass-ceramics' properties from an intrinsic perspective of crystallization, phase assembly, thermal history, and kinetics. Additionally, most of that handful of studies has been confined within the erudite realms of the pure or binary Li_2O-SiO_2 systems [29, 38-43]. Exploration on how a "multi-component" CAD-CAM bloc crystallizes has been very limited [44]. Further investigation in describing the intricate interplay between thermal treatments and crystalline architecture exhibited by these materials can offer insights on how their atomic-scale behaviors can transcend to distress or to fortify their macroscopic material properties. Most importantly, clarification on why lithium metasilicates tend to evolve to form lithium disilicates needs to be addressed so their desired clinical properties can be deliberately manifested through the manipulation of heat treatments.

In this thesis, we studied the history-dependent response (thermal versus physical) of a multi-component glass-ceramic, named IPS e.max® CAD that was sold in the form of a partially crystallized precursor, and endeavored to comprehend its kinetic process through analysis of its emergent microstructures and macroscopic physical properties. According to the manufacturer, the heating schedule for inducing crystallization of lithium disilicates within an IPS e.max® CAD bloc consisted of two (double) heating rates and two holding times, each of which was initiated and held at a specific targeted temperature (see Table 1 and Figure 3 for the group labeled as 820-840 °C). Initially, the partially crystallized precursor was heated at a rapid rate of 90 °C/min from 403 °C (furnace stand-by-temperature) to 820 °C and held for 10 seconds at 820 °C (first targeted temperature). This was followed by a slower, second heating rate of 30 °C/min. Then, it was held for a prolonged period of seven minutes at 840 °C (second targeted temperature). In this study, we hypothesized that a slower heating rate before the recommended-first-targeted temperature (820 °C) will allow further crystallization of lithium disilicates. We also hypothesized that a longer holding time at the recommended-second-targeted temperature (840 °C) will allow further crystallization of lithium disilicates, which both are expected to lead to increasing the flexural strength, fracture toughness, elastic modulus, and hardness of the final IPS e.max® CAD samples.

3. Objectives and hypotheses

3.1. Objectives

The aims of this study were:

1) To characterize the transformative behavior, crystallizing kinetics, and microstructural evolution of a partially crystallized glass precursor (IPS e.max® CAD) into lithium disilicate glass-ceramics.
2) To evaluate its physical properties (flexural strength, fracture toughness, elastic modulus, and hardness) at seven unique two-stage heating schedules
3) To find correlations between each stage of the glass precursor's evolutionary phases and microstructures and to contrast the corresponding physical properties of those phases.

3.2. Hypotheses

The null hypotheses are:

1) When IPS e.max® CAD is thermally processed under a two-stage heating schedule, an early onset of the second heating rate at a lower targeted temperature (750 °C) than the recommended (820 °C), which causes a time extension of the heating interval for the second heating stage, will not have an impact on the glass-ceramic's flexural strength, fracture toughness, elastic modulus, and hardness.
2) Protracting the holding time at the isothermal temperature, 840 °C, of the second heating stage will not have an impact on the glass-ceramic's flexural strength, fracture toughness, elastic modulus, and hardness.

The alternative hypotheses are:

1) When the temperature interval at the second heating stage is stretched from 750 to 840 °C versus from 820 to 840 °C, the glass-ceramic's flexural strength, fracture toughness, elastic modulus, and hardness are predicted to have an increase.
2) Increasing the holding time from 7 to 14 minutes at the isothermal temperature, 840 °C, of the second heating stage will increase the glass-ceramic's flexural strength, fracture toughness, elastic modulus, and hardness.

4. Materials and methods

4.1. Heating schedules

Based on past studies and manufacturer recommendations, eight unique two-stage heating schedules (including the not-fired group) were developed to evaluate the IPS e.max® CAD blocs. See Table 1 (Figure 3 is a graphical representation of Table 1). Group 820-840 °C represented the manufacturer's recommended two-stage heating schedule and was the control group. Here, the two-stage heating schedule was designed to thermally process a glass precursor in two successive stages, where each stage consisted of a unique heating rate, holding time, and targeted temperature. The targeted temperature was defined as the terminal temperature point at which the ramping of heat at a particular heating rate was ended and as the start of an additional ramping of heat at a new heating rate. Usually, the first heating rate was ramped much faster than the second heating rate. In this work, we followed the manufacturer's recommendation for which the first and second heating rates were maintained at 90 and 30 °C/min respectively. The reason behind this was for consistency, ease of comparison, and minimizing covariates.

All heating schedules were derivatives of the recommended two-stage heating schedule, but the targeted temperatures and the second holding times were modified. The heating schedules for the 530-590, 590-750, 590-750 (H14), and 750-780 °C groups allowed us to study the evolutionary development of the lithium disilicate system. For the 750-840 °C group, the second heating rate (30 °C/min) began at a lower onset temperature than the control group (750 vs. 820 °C). This would protract the time for the second heat ramping to reach the final temperature of 840 °C since it was ramping at a speed of 30 °C/min instead of 90 °C/min. The control group would take less time to complete its second heat ramping as compared with the 750-840 °C group since it was ramping through a narrower temperature interval of 20 °C scale versus an interval of 90 °C scale for the 750-840 °C group. Because of this, we suspected crystalline growth would be influenced by the prolonged second ramping time. For the 820-840 °C (H14) versus the control group, their difference was the longer holding time of 14 minutes as opposed to the regular seven minutes at 840 °C, where we were expecting the residual crystallization to occur. For this study, furnace stand-by temperature, door closing time, and heating rates were held constant. Additionally, an ultra-short first holding time of 10 seconds was followed by a second holding time of either 7 or 14 minutes. Thus, the overall heating time was calculated by summing the time for closing the furnace door, the two two-stage ramp periods, and the holding times.

4.2. Specimen preparation

Following the ISO Specification 6872 [45], the IPS e.max® CAD blocs were sectioned into bars using a diamond saw (Isomet 1000, Buehler, Lake Forest, IL). See Figure 4. The rectangular bars were randomly but equally divided into the eight groups of various firing schedules. See Table 1. Twelve rectangular bars per group were used (i.e., for the flexural test, n = 96, and for the fracture test, n = 96). After firing, all surfaces of the bar were polished using silicon carbide paper of 600-, 800-, 1000-, and 1200-grit (EXAKT Technologies, Oklahoma City, OK, USA) under running water at 300 rpm on a polishing machine (EXAKT 400 CS, EXAKT Technologies, Oklahoma City, OK, USA). After polishing with each of the various grits, the specimens were rinsed with water. The specimens were stored dry until testing was performed.

4.3. X-ray diffraction (XRD)

The XRD data were collected from three representative specimens per group by using a D8 Discover X-ray diffractometer with two-dimensional VÅNTEC-500 detector (Bruker Instruments, Billerica, MA, USA). Using monochromatic radiation ($\lambda_{K\alpha}$ = 1.5406 Å), each specimen was scanned in bulk over the 2θ range, $16^{\circ} – 82^{\circ}$, with an angular resolution of 0.005° for identifying the crystalline phases.

4.4. Flexural strength

The three-point flexure test was performed as recommended by ISO Specification 6872 [45], and the flexural strengths, σ_{FS} (MPa), were calculated according to the following formula:

$$\sigma_{FS} = \frac{3Fl}{2bd^2}$$

where F was the breaking load (N); l was the test span (mm); b was the width of the specimen (mm); and d was the thickness of the specimen (mm). The three-point flexure test fixture consisted of two cylinders with a radius of 0.8 mm (span distance of 15 mm) and a loading, cylindrical head with a radius of 0.8 mm. The IPS e.max® CAD blocs were prepared into bars (1.3 mm x 4 mm x 18 mm) as described in the sample preparation section. Each specimen was loaded to failure (crosshead speed = 0.5 mm/min) using a universal testing machine (MTS Sintech ReNew 1123, MTS Systems, Eden Prairie, MN, USA), at room temperature. The flexural modulus was acquired from the slope of the best-fitted linear region of the load-deflection curve. The mean and standard deviation were then calculated.

4.5. Fracture toughness

The fracture toughness values were determined by a single-edge notched-beam method, ISO Specification 6872 [45]. See Figure 5. The IPS e.max® CAD blocs were prepared into bars (1.3 mm x 4 mm x 18 mm) as described in the sample preparation section. The notches of the specimens were prepared with a diamond saw (blade thickness = 0.3 mm, EXAKT 300, EXAKT Technologies, Oklahoma City, OK, USA). All root radii of the prepared notches were then manually refined using a single-edged razor blade and diamond polishing paste. The final notch depth and root radius were 1.0 mm ± 0.2 mm and 0.05 mm ± 0.02 mm, respectively, which was verified by using a stereomicroscope (Nikon Measurescope UM-2, Shinjuku, Tokyo, Japan). The K_{IC} (MPa $m^{0.5}$) values were calculated using the following equations:

$$K_{IC} = \left(\frac{P\,S}{b\,w\,\sqrt{w}}\right)\left(\frac{3\,\sqrt{\alpha}}{2(1-\,\alpha)^{1.5}}\right)Y$$

$$Y = 1.9472 - 5.0247\,\alpha + 11.8954\,\alpha^2 - 18.0635\,\alpha^3 + 14.5986\,\alpha^4 - 4.6896\,\alpha^5$$

$$\alpha = \frac{a}{w}$$

where P, S, a, b, and w were peak load (MPa), test span length (m), notch depth (m), specimen thickness (m), and specimen width (m) respectively. The specimens were tested in a similar manner as flexural strength in a universal testing machine at a crosshead speed of 1 mm/min. The mean and standard deviation were then calculated.

4.6. Nanoindentation

A MTS Nanoindenter® XP (MTS Systems, Eden Prairie, MN, USA) equipped with TestWorks® software (MTS Systems, Eden Prairie, MN, USA) and fitted with a tetrahedral Berkovich diamond indenter tip (Serial # TB20128, MTS Systems, Eden Prairie, MN, USA) of 20 nm radius (faces 65.3° from vertical axis) was used to measure all specimens. A linear array of indents (100 indents per group = 10 indents per specimen x 10 specimens per group; total n = 800) was diagonally imprinted on the polished surfaces obtained from the fragments of the three-point flexure test (see Figure 6). Each consecutive indent was spaced 30 μm apart from each other to avoid any interference of residual stresses from adjacent imprints. Force–displacement curves for the indents were used to evaluate the elastic moduli. For each indent, elastic modulus was calculated using the standard methods of Oliver and Pharr [46], where the unloading force-displacement curves were fitted to the upper 50% of the maximum force with a power-law expression,

$$P = B\,(h - h_f)^m$$

where P (mN) and h (nm) were ordered pairs of force-displacement data, and B (mN/nm^m), h_f (nm), and m (no unit) were best-fit constants. Here, P was the contact force exerted by the indenter onto the sample, and h was the penetrating displacement of the indenter into the sample, relative to the position at which the indenter first contacted the sample's surface. The contact stiffness, S (mN/nm), was analytically differentiated with respect to displacement and was evaluated at the maximum displacement,

$$S = \left(\frac{dP}{dh}\right)_{h=h_{max}} = Bm(h_{max} - h_f)^{m-1}\,.$$

The contact area, A (nm^2), was determined using the depth to area calibration for the Berkovich tip. The reduced modulus, E_r (GPa), was calculated using the contact stiffness and contact area at maximum load,

$$E_r = \frac{1}{2}\sqrt{\frac{\pi}{A}}\, S\,.$$

The Elastic modulus, E (GPa), per group was computed from E_r as

$$E = (1 - \nu^2)\left[\frac{1}{E_r} - \frac{{\nu_i}^2}{E_i}\right]^{-1}$$

where ν was the Poisson's ratio of lithium disilicate glass-ceramic [47-49], and ν_i and E_i were the Poisson's ratio (0.07) and elastic modulus (1141 GPa) of the Berkovich indenter, respectively. The nanoindentation hardness was obtained from the indentation load divided by the projected contact area, A (nm^2),

$$Hardness = \frac{P}{A}$$

where the A and P were determined as described earlier.

4.7. Scanning electron microscopy (SEM)

Microstructural analyses were performed using a Field Emission-SEM (Sigma VP, Carl Zeiss, Oberkochen, Germany). To study the microstructures of lithium disilicate crystals, the polished surfaces of the glass-ceramic specimens were etched with an aqueous 9% hydrofluoric acid (HF) for one minute. This etching procedure was necessary to partially remove the glassy phase, thereby enhancing the image contrast between the crystalline and glassy phases under SEM. After the chemical etching, the specimens were washed several times using acetone and distilled water. Next, they were placed in an ultrasonic bath at room temperature for 10 minutes to remove residuals of HF and external particles adhering to the surfaces. Then, they were imaged under SEM after being sputter-coated with gold (Denton Vacuum Desk II, Denton Vacuum, Moorestown, NJ, USA).

4.8. Differential scanning calorimetry (DSC)

A differential scanning calorimeter (DSC822e, Mettler-Toledo, Columbus, OH, USA) was used to investigate the non-isothermal crystallization kinetics of the IPS e.max® CAD. Temperature and sensitivity calibrations were done in the same experimental conditions as those used for the actual samples. The non-isothermal experiments were performed on a total of forty IPS e.max® CAD specimens (10 specimens per heating rate) that were without any previous thermal treatment. Four variable heating rates (5, 10, 15, 20 °C/min) in the temperature range of 500 °C to 880 °C were done. Each specimen's dimension was 2 mm x 3 mm x 4 mm (see Figure 7) and was tested in a platinum crucible for better thermal conductivity and under nitrogen atmosphere to prevent extensive thermal degradation.

Several approaches were available to characterize the crystallization kinetics of IPS e.max® CAD. To determine the activation energy, the approach used in this study was based on the theoretical model formulated by Kissinger (1957) [50-52]. Using the Kissinger model, the relationship between a particular heating rate, β_i (e.g., 5, 10, 15, or 20 K/min), and the peak exothermic (crystallization) temperature, T_p (K), could be expressed as the following,

$$ln\left(\frac{\beta_i}{T_p}\right) = \frac{E}{R\,T_p} + constant$$

where E (kJ/mole) was the crystallization activation energy, and R was the gas constant [8.3145 J/(K mole)]. A plot of $ln\left(\frac{\beta_i}{T_p}\right)$ versus $\frac{1}{T_p}$ would then yield a straight line with slope *E/R*, whose terms could be rearranged to obtain the activation energy, E [53].

Also, ten IPS e.max® CAD specimens, again without any previous thermal treatment, were heated in the differential scanning calorimeter that strictly adhered to the manufacturer's recommended two-stage heating schedule, where each of the partially crystallized precursors was heated at a rapid rate of 90 °C/min from 403 °C (furnace stand-by-temperature) to 820 °C and held for 10 seconds at 820 °C (first targeted temperature), was followed by a slower, second heating rate of 30 °C/min, and then was held for a prolonged period of seven minutes at 840 °C (second targeted temperature). Each specimen's dimension was 2 mm x 3 mm x 4 mm (see Figure 7) and was also tested in a platinum crucible and under nitrogen atmosphere for the same reasons as explained earlier. The exothermic energies (peak area normalized against mass) were acquired from the DSC curves, and the mean and standard deviation were then calculated.

4.9. Statistical methods

The statistics of the measured properties was analyzed by the Kruskal-Wallis, one-way analysis of variance (ANOVA), and Tukey's post-hoc tests at alpha = 0.05 significance using SAS® 9.4 statistical software (SAS Institute Inc., Cary, NC, USA). Prior to conducting the multiple comparisons of means, the Kolmogorov-Smirnov test was applied to ensure that our dataset could be modeled by a normal distribution, and the Levene's test was used to assess that our dataset demonstrated homogeneity of variances. If the dataset did not meet the criteria of normal distribution, Kruskal-Wallis with Tukey's post-hoc test was used to compare groups' means. If the assumption of equal variances were not fulfilled, we would then proceed with an adjusted F statistic (Welch test) for determining whether a post-hoc test could be executed prior to comparing groups' means.

5. Results

5.1. XRD patterns

5.1.1. The not-fired, 530-590, 590-750, and 590-750 °C H14 groups

The XRD patterns for the eight groups are presented in Figure 8, and they are organized by their temperature intervals at the second heating stage of a two-stage heating schedule, from the lowest to the highest temperature intervals. Starting with the "not-fired" group at the bottom of Figure 8, the diffraction pattern near the baseline, ranging from the 2-theta scale of 16 to 38 degrees, shows a widely distributed "hump", which represents the glassy phase within the IPS e.max® CAD blocs. As the temperature was gradually elevated and the "glassy hump" slowly dwindled but did not disappear, its continual presence across all eight of the XRD patterns demonstrates the tenacity of residual glasses within the glass-ceramic matrix. This justifies that the heat-treated IPS e.max® CAD material can be categorized according to the aforementioned classification as a glassy-crystalline group. Groups that were treated within the second-stage thermal interval of 530-750 °C (i.e., 530-590, 590-750, and 590-750 °C H14) exhibited similar XRD patterns as compared to the not-fired group. Their major XRD peaks are identified to be the lithium metasilicate [Li_2SiO_3 or Li_2O-SiO_2] and lithium orthophosphates [Li_3PO_4].

The detection of Li_2SiO_3 was made by the diffraction angles at 18.82, 26.89, 32.96, 38.5, 51.59, 55.25, 58.88, 69.53, 72.64, and 75.61, using ICCD 029-0829. The identification of Li_3PO_4 was made by the diffraction angles at 29.68, 34.57, 41.43, and 44.13 using ICCD 025-1030.

5.1.2. The 750-780 °C group

As shown in Figure 8, the different peaks that appeared in the 750-780 °C XRD pattern were indicative signs of a glass-ceramic that consisted of three major phases: lithium disilicates, cristobalite, and lithium orthophosphates. For lithium disilicates and cristobalites [SiO_2], their identification was made by the diffraction angles at 23.81, 24.35, and 24.86, using ICCD 040-0376 and 015-0637, and by the diffraction angles at 21.75 and 35.78, using ICCD 039-1425, respectively, while lithium orthophosphates was identified by the diffraction angles as described in the previous section.

When the five XRD patterns, ranging from the bottom of Figure 8 up to the 750-780 °C group, were simultaneously surveyed, they revealed a glass-ceramic that was being transformed from predominantly lithium metasilicates' contents into a heterogeneous mixture of different phases. Since the XRD peak intensities have been used to qualitatively estimate the relative proportions of different phases in a glass-ceramic system by comparing peak intensities attributed to the identified phases [54], the relative peak intensities between the three major phases in the 750-780 °C group suggested that lithium metasilicates continued to thrive within the glass-ceramic network while lithium disilicate and cristobalite crystals started to amass. Hence, for groups treated with temperature below 780 °C, including the not-fired group, lithium metasilicates were observed as the main crystalline phase, which verified the manufacturer's claim that the IPS e.max® CAD bloc was a partially glassy-crystalline material.

Besides comparing relative XRD peak intensities within a group, peak intensities between groups were also evaluated. For example, the same crystalline phases that appeared at the same 2-theta positions in the XRD patterns of the not-fired, 530-590, 590-750, and 590-750

H14, and 750-780 °C groups showed peak-intensity variation. Perhaps, lithium metasilicate and lithium orthophosphate phases were the two best examples for demonstrating peak-intensity variation. For instance, the XRD peaks of lithium orthophosphate phase (marked as ■ in Figure 8) for the not-fired and 750-780 °C groups were more prominent as compared to the 590-750, and 590-750 °C H14 groups. There are two possible reasons that could lead to the peak-intensity variation for the lithium orthophosphates between groups. One, the presence of lithium orthophosphates was expected for the not-fired group since it was included as a nucleating agent according to the manufacturer. Its disappearance in the 530-590 °C group and the gradual reemergence through heating from 590 to 780 °C (see Figure 8, g, f, e, and d) were indicative that the growth of lithium orthophosphates could be induced, where its development was postulated to depend on how the phosphate ions could act as a lithium ion scavenger, resulting in the formation of lithium orthophosphate [34]. The XRD peaks of lithium metasilicate phase (marked as ❖ in Figure 8) for the 530-590, 590-750, and 590-750 °C H14 groups were less prominent than the not-fired and 750-780 °C groups. Again, this gradual enlargement of the lithium metasilicates' peak intensities indicated that the development of lithium metasilicates was postulated to be temperature dependent and to involve the epitaxial growth of lithium metasilicate on a lithium orthophosphate crystal [32, 55].

5.1.3. The 750-840, 820-840, and 820-840 °C (H14) groups

For groups treated with the thermal ranges above 780 °C, the precipitations of lithium disilicates [$Li_2Si_2O_5$ or Li_2O-$2SiO_2$] were seen as the main crystalline phase. The crystallization of lithium disilicates for the 820-840 °C (recommended) group was observed at diffraction angles of 22.35, 23.81, 24.35, 24.86, 30.60, 37.61, 38.12, 39.29, 43.98, 45.24, 46.13, 49.26, 50.51, 50.87, 60.51, 63.56, 64.71, 65.52, 68.23, and 75.97 for which the intensities of its three strongest peaks (23.81, 24.35, and 24.86) represented the (130), (040), and (111) crystallographic planes of the Li_2O-$2SiO_2$ monoclinic phase as predicated from ICCD 040-0376 and 015-0637. In addition, the intensities for these three strongest peaks demonstrated a gradual increase in comparison to their infancy state when treated with the temperature interval between 750 and 780 °C. This showed that a greater amount of lithium disilicate crystallization developed for groups treated with the temperature intervals above 780 °C than the 750-780 °C group. Also, the XRD patterns exhibited other minor chemical species. For example, a discernable peak, fused at its baseline and comprised of three local maxima, settled at the 21.75 next to the 22.35 peak; this peak denoted the presence of cristobalite. Furthermore, the thermodynamically less stable remnants, lithium metasilicates and lithium orthophosphates, persisted at 41.43 and 72.61 degrees respectively. The 820-840 (H14) and 750-840 °C groups have diffraction angles matching the recommended group, demonstrating a steady amount of Li_2O-$2SiO_2$ crystalline growth as well as the presence of lithium metasilicate remnants. Thus, the XRD patterns have revealed that the transformation from lithium metasilicates to lithium disilicates was dependent on the heating temperature but independent of the overall heating time. A minimum threshold of 780 °C has to be crossed for growth and maturation of lithium disilicates.

5.2. Physical properties

Significant differences were found between groups per physical property. Table 2 summarizes the measured results and statistics for all physical properties, and Figures 9-13 represent the graphical summary of Table 2. Except for fracture toughness and nano-hardness, groups treated with temperatures surpassing 780 °C, which were 750-840, 820-840, and 820-840 °C (H14), significantly outperformed the groups treated with temperatures below 780 °C in every aspect of the tested properties. For this study, the abscissae for Figures 9-13 are displayed as ordinal scales, where the temperatures were not continuously scaled but rather incrementally segmented from room temperature to 840 °C, and this made correlation between the physical properties and temperatures difficult. However, a generalized upward trend existed for Figures 9-11, such that the flexural strength, flexural modulus, and fracture toughness started at a minimum, then, gradually sloped upward, and finally reached a plateau. Furthermore, in Figures 9-13, the temperature interval, 750-780 °C, demarcated a transitional point, where a change, for better or worse, in physical properties was about to commence.

5.2.1. Flexural strength, flexural modulus, and fracture toughness

The glass-ceramic, IPS e.max® CAD, exhibited significant differences in flexural strength at three distinctive thermal ranges: below 590 °C, between 590-780 °C, and above 780 °C. The three highest flexural strength values were 350.46 ± 43.01, 366.61 ± 43.28, and 362.08 ± 78.62 MPa for groups, 750-840, 820-840, 820-840 °C (H14) respectively. See Table 2.

For the physical property of flexural modulus, the 820-840 °C group (66.58 ± 5.52 GPa) demonstrated significantly higher flexural modulus than all other groups while the next two highest were the groups of 750-840 °C (60.90 ± 6.46 GPa) and 820-840 °C (H14) (57.57 ± 2.28 GPa). For groups that were intentionally not heated above 780 °C, they displayed no statistically significant differences from each other. But, interestingly, the flexural moduli of the 590-750 and 750-780 °C groups are not significantly different from the 820-840 °C (H14) modulus.

Figure 11 presents the changes in glass-ceramic's ability to resist fracture as a function of its heat-treatment temperatures. Statistically, groups with the same letter are not significantly different than each other. The overlapping of the same letter with its adjacent group makes interpretation of Figure 11 challenging. However, Figure 11 illustrates a gradual shift from the letter, "a", to the letter, "e", demonstrating that fracture toughness could be significantly improved via heat treatment. Furthermore, the 820-840 °C (H14) (4.07 ± 0.73 GPa) and 820-840 °C (3.55 ± 0.57 GPa) groups exhibited significantly higher toughness than all other groups, while the 590-750 (H14), 750-780, and 750-840 °C groups were not significantly different from one another in terms of their ability to resist fractures. Similarly, groups like 590-750 °C (H14) and 820-840 °C (H14) that were held at the second targeted temperature for a prolonged period of 14 minutes portrayed similar fracture resistance as those groups without the extra 14 minutes of heat treatment, specifically the 590-750 °C and 820-840 °C group respectively.

5.2.2. Nanoindentation – elastic modulus

Figure 12 shows how elastic modulus could be tailored via various two-stage heating schedules. The two best temperature intervals for achieving the two highest elastic modulus values were the 750-840 °C and 820-840 °C (H14) groups, having the values of 98.97 ± 1.29 GPa and 98.94 ± 2.82 GPa respectively. See Table 2. Even though these two groups were not statistically different than each other, they performed significantly better than all other groups, including the recommended group whose elastic modulus was ranked the next highest in comparison with all groups. For those groups that were deprived of heating above 780 °C, the 750-780 °C group exhibited a significantly lower elastic modulus (75.86 ± 6.99 GPa) than all groups. Interestingly, the one trait that the 750-780 and 530-590 °C groups have in common was their large standard deviations, which resulted in the spreading of their 95% confidence intervals (74.39-77.33 and 82.84-84.30 GPa respectively) in comparison with the other groups. This variability in elastic moduli depicted that the microstructures of the 750-780 and 530-590 °C groups could be composed of heterogeneous phases rather than a homogeneous distribution of a single crystalline phase. Furthermore, these two temperature intervals could be considered as critical transitions in the overall development of lithium disilicate crystals.

5.2.3. Nanoindentation – hardness

Figure 13 discloses the relationship between nanoindentation hardness and various two-stage heating schedules. Unlike Figures 9-11, where a generalized upward trend exists, the surface hardness for the lithium disilicate glass-ceramics started at a maximum at low temperatures but decreased across-the-board with increasing temperatures. We will revisit the reasons behind this trend of decreasing hardness versus increasing temperature in the discussion section (6.3. Glass-ceramic's crystalline-density-saturation-gradient composition and its hardness). Figure 13 also shows that the 590-750 °C group exhibited a higher surface hardness than all the other tested groups, while the surface hardness for the specimens in the 750-780 °C group was the lowest when compared to all the other groups. In addition, due to the presence of heterogeneous phases, the 750-780 °C group resulted in the largest standard deviation in comparison to all other groups.

5.3. Microstructural evolution

For this study, the strengthening of the glass-ceramic physical properties corresponded to the appearance and disappearance of lithium disilicate and lithium metasilicate crystals respectively. After HF etching and in the absence of the surrounding glassy continuum, the SEM micrographs (Figures 14 A-H) identified three major microstructures: (1) the porous and finely knitted mesh of lithium metasilicates existed below the 590 °C thermal range; (2) the ovoid- and spherical-like configurations of Li_2SiO_3 and Li_3PO_4 emerged within the thermal range of 590-780 °C; and (3) the irregularly rod-shaped or oblate-like crystals of lithium disilicates appeared above the 780 °C thermal range. For the two groups treated with the thermal ranges below 590 °C, both exhibited similar, less dense, mesh-like microstructures, in which lithium disilicate precipitates were not seen (Figures 14 A-B). For the thermal ranges between 590-780 °C, the spherical-like morphologies of the 590-750 and 750-780 °C groups appeared to be larger in size and more maturely grown than the 590-750 °C (H14) group. Even though the 590-750 (H14) and 750-780 °C groups were both held at the second targeted temperature for a prolonged period of 14 minutes, the 590-750 °C (H14) group acquired more of the knitted-mesh network, which could be possible remnants persisting from the thermal range below 590 °C, when compared with the 750-780 °C whose morphology was mostly spherical. However, the mesh-like network of 590-750 °C (H14) group appeared to be less porous and much denser than the not-fired and 530-590 °C groups. Although the 590-750 °C (H14) and 750-780 °C groups had the two longest overall heating times, they received a thermal range below the minimum temperature threshold. This delivering of the insufficient thermal energy merely elicited a response of densification rather than crystallization. For the three groups treated with the thermal ranges above 780 °C, lithium disilicates were clearly observed as rod-like crystals (Figures 14 F-H), and their orientations were random, making the overall bulk properties behave in an isotropic manner.

For these groups, the rod-shaped crystals not only interlocked with each other but also intertwined amongst the mesh-like, dendritic cavities, which were once occupied by the glassy and lithium metasilicate phases that were etched away for increasing SEM image contrast; and, these isotropic crystals played a significant role in modifying the bulk properties like flexural strength, fracture toughness, elastic modulus, and hardness of the material.

5.4. Non-isothermal kinetics for lithium disilicate crystallization

5.4.1. Defining terminologies for DSC curves and tables

Four DSC curves were selected as representatives for all the single-stage heating schedules. See Figure 15. Also, the representatives for the DSC curves of the recommended two-stage heating (820-840 °C group) are illustrated in Figure 16. These DSC curves are summarized in Table 3A-C, which contain additional information such as the specimens' masses, peak areas (labeled as integrals), peak areas normalized against mass (labeled as normalized), heights, widths, peak temperatures, and extrapolated peak temperatures for all fifty DSC curves. Here, the peak temperature is not the same as extrapolated peak temperature and is the temperature point, whose peak height is at its maximum, while the extrapolated peak temperature is acquired by orthogonally projecting its maximum peak-height point onto the temperature abscissa. Also, the peak heights and widths were directly associated to the number of nuclei and crystals and the time that it takes for crystallization to reach completion.

5.4.2. Single-stage DSC heating curves

Figures 15 and 16 show two exothermic peaks for each of the single- and two-stage DSC heating curves respectively, but only one peak is observed for each of the 20 °C/min heating curves in Figure 15. Starting with the one-stage heating, for the 5 °C/min rate, its first peak mostly happened in the temperature interval between 807 °C and 835 °C with its extrapolated peak temperature located at 821.11 ± 0.84 °C. Its second peak predominantly occurred between 846 °C and 868 °C with its extrapolated peak temperature positioned at 857.03 ± 1.11 °C. As the heating rates were increased from 5 to 20 °C/min, the extrapolated peak temperatures were also increased, shifting to the right of the abscissae in Figure 15. For example, when the heating rate of 5 °C/min was elevated to 15 °C/min, the extrapolated peak temperature for peak-1 shifted from 821.11 ± 0.84 °C to 848.95 ± 1.62 °C respectively. For peak-2, a similar trend was observed, in which the extrapolated peak temperatures boosted from 857.03 ± 1.11 °C to 877.49 ± 2.78 °C for increasing the heating rates from 5 to 20 °C/min respectively.

5.4.3. Two-stage DSC heating curves

Next, the two-stage heating was evaluated. For the double heating rates, its extrapolated peak temperature was 814.65 ± 1.17 °C (having a peak width = 39.51 ± 16.19 °C) and 854.59 ± 0.44 °C (having a peak width = 8.07 ± 2.31 °C) for peak-1 and peak-2 respectively. This indicated that the onset and ending of its first peak was most likely to occur in the temperature interval of 775-854°C. Its second peak was likely to appear in the temperature interval of 847-863 °C. A cross comparison between the two-stage DSC heating curves with those XRD patterns and SEM images, whose temperature intervals encompassed the onset-and-ending temperatures of 775-863 °C, suggested that the possible phases for peak-1 and peak-2 were lithium metasilicates, lithium orthophosphate, cristobalites, and lithium disilicates. Therefore, we suspected that the two exothermic peaks signified the result of two processes: (1) the nucleation and crystallization of an unstable intermediate, lithium metasilicates, and (2) the nucleation and crystallization of a stable product, lithium disilicates.

5.4.4. Relationship between heating rates and exothermic peak temperatures

Also, Figure 15 reveals the gradual union of peak-1 and peak-2. Even though separation of peak-1 from peak-2 was readily distinguishable for the heating rate of 5, 10, and 15 °C/min, signs of merger at the baseline was beginning to take shape, especially at the rate of 15 °C/min. At the 20 °C/min rate, the overlapping between peak-1 and peak-2 had commenced, and peak-1 was dwarfed next to peak-2. We suspected that if the heating rates were to continuously surge, peak-2 would remain to be the only peak and would resume shifting to higher temperatures until it coincided with its melting point. Furthermore, if the extrapolated peak temperatures were plotted against heating rates (Figure 17), their relationship was inversely proportional with each other. However, this inversely proportional relationship might not be valid for the two-stage heating schedule, since the two-stage heating schedule, whose first and second heating rates were 90 and 30 °C/min respectively, demonstrated a slightly lower average extrapolated peak temperature than the value of the slowest heating rate (i.e., 5 °C/min) for all single-stage heating schedules. In other words, in the presence of double heating rates, the "shifting" of peaks to higher temperatures were less likely since they were purposely controlled and segregated by their respective heating rate. Additionally, this separation of peak-1 from peak-2 made by the double heating rates provided two different environments: one for the nourishment of nucleation and the other for the enrichment of crystallization.

5.4.5. Effective activation energy

For this thesis, the most popular approximation developed by Kissinger (1957) was used to model the kinetics of lithium metasilicates and lithium disilicates [50-52]. The lines in Figures 18A and B, attained from the statistical linear regression, were the best fits between $ln\left(\frac{\beta_i}{T_p}\right)$ and $\frac{1}{T_p}$, whose slopes (*E/R*, no unit) yielded the values of 45.769 for peak-1 and 80.276 for peak-2. These slopes were multiplied by the gas constant (8.3144621 J K^{-1} $mole^{-1}$) to obtain the effective activation energies of peak-1 (380.55 ± 8.20 kJ/mole) and peak-2 (667.45±28.97 kJ/mole), which were the minimum energy barriers that must be overcome for nucleation and crystallization of lithium metasilicates and lithium disilicates within an IPS e.max® CAD bloc to happen. Finally, past studies have shown that the release of the exothermic energies (peak area normalized against mass) was directly proportional to the number of nuclei and crystals that were formed. Figure 19 demonstrates that the exothermic energies released by a glass-ceramic processed through the two-stage heating method were significantly more than the single-stage heating process.

6. Discussion

6.1. Assessment of our null and alternative hypotheses

Within the limits of this study, we have found that the premature onset of the second heating rate at the targeted temperature of 750 °C rather than 820 °C did not have a statistically significant impact on the glass-ceramic's flexural strength and fracture toughness. Given this evidence, we would be inclined to reject the first null hypothesis, but our other outcomes such as the glass-ceramic's flexural modulus, elastic modulus, and hardness were significantly altered by the perturbation provoked from our imposed condition. For example, the glass-ceramic's elastic modulus and hardness were significantly enhanced for the 750-840 °C temperature interval versus those for the recommended heating interval (820-840 °C). However, the flexural modulus of the 750-840 °C interval was significantly lowered than the value of the recommended heating interval, portraying no distinctive improvement in its ability to resist bending deformation than the 820-840 °C specimens. Thus, we could neither fully reject nor accept our first null and alternative hypotheses.

Similarly for the 820-840 °C group versus the 820-840 °C (H14) group, our evidence suggested that protracting the holding time at the isothermal temperature, 840 °C, of the second heating stage did not have a statistically significant impact on the glass-ceramic's flexural strength and fracture toughness, but we did find statistically significant differences in flexural modulus, elastic modulus, and hardness between those two groups. Furthermore, the glass-ceramic's elastic modulus and hardness for the 820-840 °C (H14) group were significantly improved in comparison with the recommended group. However, when only flexural modulus was assessed, a significant decrease was observed between the two groups, demonstrating that protracting the holding time from 7 to 14 minutes at the isothermal temperature, 840 °C, of the second heating stage did have an impact. Therefore, we could neither fully reject nor accept our second null and alternative hypotheses.

6.2. Relationship between heating schedules, microstructures, and physical properties

Although we could only partially reject the null and alternative hypotheses, our study did demonstrate that the evolutionary process from lithium metasilicates into the lithium disilicate glass-ceramics was closely related to how their partially crystallized glass precursor responded to thermal exposure. This concept that the macroscopic behavior of the lithium disilicate glass-ceramics was dependent on its thermal history was not new to the existing literature, and we will further defend this concept with two viewpoints along with supportive data that were collected from this study.

First, we found that the macroscopic physical properties of glass-ceramic were highly dependent on the microstructural evolution of lithium disilicates, whose growth was intricately related to our imposed heating schedules. For example, the wax and wane of each specific microstructure (finely knitted mesh, spherical-like intermediates, and irregularly oblate-like crystals) were respectively associated with the three successive thermal intervals (below 590 °C, between 590-780 °C, and above 780 °C). Furthermore, a significant trend of gradual improvement in physical properties was seen for each of those three thermal intervals. Amongst the microstructural phases, the three groups treated above 780 °C have the most distinctive microstructural separation of all other groups and contributed the highest statistically significant average values in flexural strength, flexural modulus, fracture toughness, and elastic modulus. Thus, the multi-component glass-ceramics were dependent on our imposed heating conditions whose thermal energies transcended into developing different mixtures of microstructural phases, which were further manifested into different macroscopic glass-ceramic solids that offered a combination of physical properties based on the benefits of those heterogeneous phases.

Second, the improved physical properties for the glass-ceramics containing lithium disilicates may be interpreted from a perspective of a hierarchical structure. Like enamel or bone, the glass-ceramic continuum that develops after thermal processing exhibits a structural hierarchy featuring the macro-scale voids between the glass-crystal interfaces, the micro-scale shape and size of the crystals, and the nano-scale defects in the crystalline lattice. Because of this wide scale range, these structural configurations play a vital role in influencing the physical properties of a glass-ceramic [36, 56]. As shown by our SEM images, the complexity of the spatial distribution of Li_2O-$2SiO_2$ crystals for groups above 780 °C significantly contributed to the enhanced strength, modulus, and fracture toughness of the CAD blocs. For groups below 780 °C, their weak physical properties were associated with the absence of the high Li_2O-$2SiO_2$ volume fraction. These results appeared to be in good agreement with the fracture theory proposed by Hasselman and Fulrath, which stated: the strength of a glass-ceramic with a high volume fraction of a continuous glassy matrix is only dependent on the volume fraction of its crystallinity, but the strength of a glass-ceramic with a high crystalline volume fraction is a function of both the volume fraction and size of its crystalline phase [56]. Furthermore, the average distance between crystals dispersed in the matrix could have an impact on governing the average flaw size and on how crack propagation could have been barricaded or possibly stopped to avoid crack bridging [56]. Although we were not able to attest as to how the different sizes of lithium disilicates could influence the glass-ceramic properties, we were able to easily distinguish the "crowded" distribution and isotropic orientation of the Li_2O-$2SiO_2$ crystals as opposed to the more porous and mesh-like network of lithium metasilicates. According to the aforementioned concepts, these random configurations could be the deterrents against fracture and a source of strength for the lithium disilicate glass-ceramics, which were reflected from our tested properties.

6.3. Glass-ceramic's crystalline-density-saturation-gradient composition and its hardness

The trend of decreasing hardness versus increasing temperature was atypical and could be explained by the process of nucleation and crystallization (i.e., devitrification). For example, the orientation and saturation of crystals within a glass-ceramic relied on the proximity between the nucleating sites and on the locations and numbers of nucleating agents, whose development could be induced at random or at the glass-ceramic's center of mass or its periphery and whose distribution might or might not be homogenous in bulk [26, 57, 58]. Therefore, quite possibly, a crystalline-density-saturation gradient, defined as the stratification of different glassy-crystalline ratios at different depths or regions in a glass-ceramic, could have been developed across from the glass-ceramic's center to its periphery. Furthermore, since nucleating agents were believed to be the precursors for epitaxial crystallization to occur, the mapping of where crystallization initiated and where the crystallites distributed in the glass-ceramic ought to mirror the positions of the nucleating sites. Additionally, because the epitaxial growth at the nucleation center was dependent on the diffusivity of chemical species, any type of fluctuations such as temperature, pressure, or composition could potentially perturb and could jeopardize the movement of molecular concentration gradient from obeying Fick's law. Thus, each two-stage heating schedule could yield a unique glassy-crystalline ratio across the glass-ceramic's peripheral surfaces and throughout its outer-to-inner core, resulting in distinct surface-indentation-hardness values amongst the various two-stage heat treatments and quite possibly resulting in distinct indentation-hardness values per depth (i.e., depth across from the glass-ceramic's periphery to its core) and per two-stage heat treatment.

According to past studies, the indentation-hardness value of a glass-ceramic was related to the glass-crystalline ratio, and polycrystalline ceramics generally exhibited greater surface-hardness values when compared to glass ceramics that contained a high percentage of glass [59], and a glass-ceramic with a high hardness value is equivalent to having a higher number of crystals on its surfaces than a glass-ceramic with a low hardness value. Because of this, we suspected that the number of crystals on the glass-ceramic's surfaces for groups treated with temperature intervals above 780 °C to be fewer than those treated below 780 °C. This was because the groups above 780 °C demonstrated a significant decrease in hardness value than those treated below 780 °C.

Furthermore, based on our hardness, XRD, DSC, and SEM results, we hypothesized that: at low heating temperature intervals (e.g., 530-590 and 590-750 °C), the transformation from lithium metasilicates to lithium disilicates was immature; the separation between nucleating-, crystallizing-, and glassy-phases was indistinct; and, crystalline-density-saturation gradient through compositional segregation via epitaxial crystallization was not yet apparent. Thereby, glass-ceramics that were processed at low heating temperature intervals should generate similar saturations of un-evolved lithium metasilicates to that of unfired glass-ceramics. And, surface hardness remained less altered for the not-fired, 530-590, and 590-750 °C groups than those groups treated above 780 °C because compositional segregation between lithium metasilicates, lithium disilicates, and residual glass was expected to be absent, and the surfaces of not-fired, 530-590, and 590-750 °C glass-ceramic specimens consisted of relatively similar surface hardness – perhaps these groups also contain similar ratios of lithium-metasilicate-to-glassy components due to hardness-to-crystallinity proportionality. While at high heating temperatures, due to thermodynamic influence on the diffusivity of chemical species, compositional segregation would be more evident, producing more condensations of lithium disilicate crystals at the glass-ceramic core than at its surfaces, which resulted in more glass than crystals being present on the glass-ceramic surfaces, thereby yielding low hardness value.

However, for the 590-750 °C group, we saw a significant increase in surface hardness when compared with all other groups. We believe that at this temperature interval, a greater fraction of atoms and molecules did not have sufficient energy to "make it over" the activation energy barrier for growth of lithium disilicates to occur but did have enough energy to increase the probability of nucleation. And, as nucleation progressed, the mobility and collisional reactivity of atoms and molecules could be impeded through the action of densification by viscous sintering. Then, we suspected that this action of densification would permeate throughout the glass-ceramic. Because of this, the 590-750 °C group had the significantly higher hardness value than the other groups.

In contrast, protracting the holding time from 7 to 14 minutes at the isothermal temperature, 750 °C, did not improve the diffusivity of atoms and possibly the action of densification but might have encouraged the action of compositional segregation, which could be the reason behind the lower hardness value for the 590-750 °C (H14) than the 590-750 °C group. As the heating temperatures were raised from 750 to 780 °C, we theorized that bulk crystallization within an IPS e.max® CAD bloc began its nucleation and crystalline growth near the glass-ceramic's core (e.g., center of mass). However, the propagation of crystalline growth from the glass-ceramic's core to its periphery was stopped short due to insufficient delivering of thermal energy, and the glass-ceramic system ended with more crystalline condensation in the central zone than near its peripheral surfaces, thereby, increasing the glassy phases on the surfaces of the 750-780 °C group (decreasing surface hardness value). Because of this, the 750-780 °C group showed the greatest statistically significant surface softening and had the largest standard deviation of all the groups. This was no surprise, since, like the large standard deviation that was observed for its elastic modulus, the surface hardness for the 750-780 °C group was influenced by its heterogeneous phases due to compositional segregation.

6.4. Comparison with past studies

Similar to past studies [26, 41, 44], our SEM indicated that the crystallizing scheme of the IPS e.max® CAD began with the glassy-crystalline separation. When the temperature was gradually raised from 530 °C to 590 °C, the lithium metasilicate continued to be the dominant phase with no new type of crystalline precipitate. Other studies have reported the presence of a mixture of lithium metasilicate and lithium orthophosphate at a temperature range of 500-560 °C, where the precipitations of Li_3PO_4 acted as the first nano-particles or sites for crystallization prior to the manifestation of lithium disilicates [26, 32]. For our case, the XRD patterns showed that Li_3PO_4 was already incorporated into the not-fired glass-ceramic blocs, but interestingly it disappeared when treating with the heating schedules of 530-590, 590-750, and 590-750 °C (H14). On the contrary, when heating was elevated to and beyond 750 °C, only then Li_3PO_4 precipitates reappeared and remained as a residual phase in the three glass-ceramic groups, 750-840, 820-840, and 820-840 °C (H14), that had the highest treated thermal ranges. One possible explanation to the occurrence of Li_3PO_4 at dissimilar thermal settings was owing to the difference in stoichiometric and elemental compositions between IPS e.max® CAD and the earlier glass-ceramics. Only specific stoichiometric compositions of alkali- and alkaline earth-metal silicate crystals were considered as suitable formulations for designing a glass-ceramic system with crystalline assemblage [30, 60]. An alternative reason was that at the intermediate temperature intervals (530-750 °C), the Li_3PO_4 structures began reorganization, forming amorphous nano-size particles, and consequently escaped the XRD detection [61]. When the temperature surged beyond 780 °C, both our

SEM images and XRD patterns revealed that the growth of lithium disilicates was abrupt, and this phenomenon was accompanied by the presence of lithium orthophosphates, possibly started as intermediates and ended as residual remnants. As mentioned in the earlier section, Headley and Loehman (1984) have shown that the success of lithium disilicate crystalline growth was powerfully influenced by their ability to epitaxy on the Li_3PO_4 nuclei, whose assemblage was built by amassing with the agglomeration of nucleating agents like P_2O_5, TiO_2, and ZrO_2 along with the appropriate heating condition [32]. We could only suspect that Li_3PO_4 could have played a role in the development of lithium disilicates. Finally, stable lithium disilicate assemblage was observed over the 750-840 °C range while lithium metasilicates disintegrated. See Figure 20 for the possible reaction mechanisms when IPS e.max® CAD was heat-treated. This activity was in accordance with earlier findings [26].

Generally, explosive growth of lithium disilicates occurs only when the maximum formation of lithium metasilicates has ended [26]. Numerous authors have postulated that lithium metasilicates serve as catalysts for lithium disilicate crystallization, while others argue that lithium metasilicates are unstable intermediates, and their nuclei serve as centers for epitaxial growth of lithium disilicate crystals [38, 40, 42]. For this study, we were unable to prove or disprove whether the lithium disilicates within a heat-treated IPS e.max® CAD bloc have nucleated on their own accord or whether their precipitations have been influenced by lithium metasilicates. However, our DSC data strongly suggest that the nucleation and crystallization are two events that are dependent on one another. In summary, our glass-ceramic system in its initial equilibrium state would respond and seek a new equilibrium state under the influence of the sudden change in one of the variables (e.g., temperature, pressure, composition, etc.). Typically when the crystallizing reaction reaches an equilibrium with its glassy component, a glass-ceramic exhibits partial crystalline assemblage with its microstructure possessing approximately 50-95% crystalline volume fraction and its remainder being residual glass [30, 60].

If the glass-ceramic continuum is viewed under the nano-scale perspective, the forces and energies that are needed to disrupt the mixed ionic-covalent bonds between atoms have a direct connection with the “bulk” nature of flexing and bowing for a glass-ceramic under compressive and tensile stresses. Specifically, flexural and elastic moduli of lithium disilicates and lithium metasilicates could be used to predict the stability of the atomic bonding forces. For example, knowing that the glass-ceramic groups like 750-840, 820-840, and 820-840 °C (H14) (mainly composed of lithium disilicate crystals) significantly outperformed all other groups (mainly composed of lithium metasilicates) in nearly every aspect of the tested properties, one could anticipate that more energy or forces were required in order to break the atomic bonds for lithium disilicates than lithium metasilicates. Contrariwise, less thermal energy was needed in favor of growing Li_2SiO_3 crystals, while an ample amount of thermal energy was compulsory to surpass the steep activation energy of the glassy-to-crystalline reaction so Li_2O-$2SiO_2$ growths could occur. As shown by our data, only temperatures exceeding beyond 780 °C could induce growth of Li_2O-$2SiO_2$ crystals, while formation of Li_2SiO_3 crystals necessitated less thermal energy, approximately in the temperature range of 530-750 °C.

6.5. Future research

For this study, the key challenge was to identify appropriate thermal gradients that could predict the microstructural changes of the IPS e.max® CAD blocs. Alternative heating schedules that involved different combinations of thermal gradients, curtailed-or-prolonged heating rates, and temperature holding times could have been evaluated to further understand the thermal responses of our materials. However, the heating schedule selection decisions should ideally have clinical performance in mind so that the optimal heating schedule would result in a final product that would offer the best survival probability for our glass-ceramic prosthesis. Also, further investigation on the crystallization activation energy might explain why lithium metasilicates could only achieve structural densification, as shown in Figures 14 C-E, but failed to form lithium disilicates. We have not addressed the effect of restrictions other than temperature such as pressure and concentrations of the constituent components, which could also impose microstructural alterations. Another limitation has to do with the reliability of our laboratory measurements. In this study, we have chosen fracture toughness, flexural strength, and elastic modulus as reliable parameters because they have been commonly known as good clinical predictors from past literature even though there was no proven association, at least in clinical dentistry, between these parameters and their clinical outcomes [62, 63].

7. Conclusions

The heat treatments carried out in this study fell into three categories, temperature ranges below 590 °C, between 590-780 °C, and above 780 °C. Consequently, from these three thermal categories, three major microstructures were identified: the finely knitted mesh [Li_2SiO_3] predominated below 590 °C; the spherical-like intermediates [Li_2SiO_3, Li_2O-$2SiO_2$, and Li_3PO_4] emerged between 590-780 °C; and, irregularly oblate-like crystals [Li_2O-$2SiO_2$] arose above 780 °C. The possible evolutionary process of the IPS e.max® CAD from the partial lithium metasilicate-based glass-precursor to the partial lithium disilicate-based glass-ceramic is summarized in Table 4. At each of these three evolutionary stages, a glass-ceramic that was formed through controlled devitrification via distinctive heating schedules often yielded a principal microstructure that possessed interesting, sometimes peculiar, combinations of glassy-crystalline properties. Furthermore, the wax and wane of the IPS e.max® CAD's physical properties significantly correlated with the presence and absence of the lithium disilicate precipitations. Additionally, the growth of Li_2O-$2SiO_2$ crystals within the IPS e.max® CAD blocs was independent of the overall heating time but dependent on a minimum temperature threshold (780 °C). Finally, the effective activation energy of crystallization calculated from the non-isothermal measurements for the IPS e.max® CAD blocs was 667.45 ± 28.97 kJ/mole. In summary, we have demonstrated that through unique heat tailoring of an IPS e.max® CAD bloc, its physical properties could be altered.

8. Tables

	G_1		G_2		G_3		G_4		G_5		G_6		G_7		G_8	
	Not Fired		530 - 590 °C		590 - 750 °C		590 - 750 °C (H14)		750 - 780°C		750 - 840 °C		Recommended 820 - 840 °C		820 - 840 °C (H14)	
	Stage 1	Stage 2	Stage 1	Stage 2	Stage 1	Stage 2	Stage 1	Stage 2	Stage 1	Stage 2	Stage 1	Stage 2	Stage 1	Stage 2	Stage 1	Stage 2
B (°C)			403		403		403		403		403		403		403	
S (min)			0.3		0.3		0.3		0.3		0.3		0.3		0.3	
t ↗ (°C/min)			90	30	90	30	90	30	90	30	90	30	90	30	90	30
T (°C)	(Not Applicable)		530	590	590	750	590	750	750	780	750	840	820	840	820	840
H (min)			0:10	7	0:10	7	0:10	14	5	14	0:10	7	0:10	7	0:10	14
V1 (°C)			450	530	450	590	450	590	550	750	450	750	550	820	550	820
V2 (°C)			530	590	590	750	590	750	750	780	750	840	820	840	820	840
Heating Time (min)	(Not Applicable)		10.88		14.88		21.88		24.16		14.32		12.77		19.77	

B (°C) = Furnace Stand-By-Temperature
S (min) = Furnace Door Closing Time
t ↗ (°C/min) = Heating or Ramp Rate
T (°C) = Holding Temperature
H (min) = Holding Time
V1 (°C) = Vacuum-On Temperature
V2 (°C) = Vacuum-Off Temperature
(H14) = Hold for 14 min

Table 1: Two-stage heating schedules.

Group	Flexural Strength (MPa)						Flexural Modulus (GPa)					
	Average	SD	Z	Margin of Error	Upper	Lower	Average	SD	Z	Margin of Error	Upper	Lower
Not-Fired	163.26	24.89	1.96	14.08	177.35	149.18	50.37	3.64	1.96	2.06	52.43	48.31
530-590 °C	161.37	31.86	1.96	18.02	179.39	143.35	50.21	4.53	1.96	2.56	52.78	47.65
590-750 °C	268.57	46.11	1.96	26.09	294.66	242.48	52.38	3.72	1.96	2.11	54.49	50.28
590-750 °C (H14)	237.42	40.47	1.96	22.90	260.32	214.52	49.71	3.61	1.96	2.04	51.76	47.67
750-780 °C	277.19	49.38	1.96	27.94	305.13	249.25	52.20	3.22	1.96	1.82	54.03	50.38
750-840 °C	350.46	43.01	1.96	24.33	374.79	326.12	60.90	6.36	1.96	3.60	64.51	57.30
820-840 °C	366.61	43.28	1.96	20.57	387.18	346.03	66.58	5.52	1.96	2.62	69.20	63.96
820-840 °C (H14)	362.08	78.62	1.96	44.48	406.56	317.59	57.57	2.28	1.96	1.29	58.87	56.28

Group	K_{IC} (MPa $m^{0.5}$)					
	Average	SD	Z	Margin of Error	Upper	Lower
Not-Fired	1.71	0.26	1.96	0.15	1.86	1.57
530-590 °C	1.80	0.39	1.96	0.22	2.02	1.58
590-750 °C	2.25	0.52	1.96	0.30	2.55	1.96
590-750 °C (H14)	2.75	0.76	1.96	0.43	3.18	2.32
750-780 °C	2.74	0.89	1.96	0.50	3.24	2.24
750-840 °C	3.25	0.68	1.96	0.39	3.64	2.87
820-840 °C	3.55	0.57	1.96	0.31	3.86	3.24
820-840 °C (H14)	4.07	0.73	1.96	0.41	4.48	3.65

Group	Elastic Modulus (GPa)						Hardness (GPa)					
	Average	SD	Z	Margin of Error	Upper	Lower	Average	SD	Z	Margin of Error	Upper	Lower
Not-Fired	85.95	1.22	1.96	0.24	86.19	85.71	8.01	0.26	1.96	0.05	8.06	7.96
530-590 °C	83.57	3.81	1.96	0.73	84.30	82.84	8.14	0.37	1.96	0.07	8.21	8.07
590-750 °C	85.42	1.82	1.96	0.32	85.75	85.10	8.24	0.13	1.96	0.02	8.26	8.22
590-750 °C (H14)	84.34	3.65	1.96	0.71	85.05	83.62	7.79	0.37	1.96	0.07	7.86	7.72
750-780 °C	75.86	6.99	1.96	1.47	77.33	74.39	6.85	0.78	1.96	0.16	7.02	6.69
750-840 °C	98.97	1.29	1.96	0.26	99.23	98.71	7.74	0.14	1.96	0.03	7.77	7.71
820-840 °C	96.94	2.30	1.96	0.53	97.47	96.41	7.54	0.15	1.96	0.04	7.58	7.51
820-840 °C (H14)	98.94	2.82	1.96	0.50	99.45	98.44	7.76	0.21	1.96	0.04	7.80	7.73

Table 2: Descriptive statistics for all tested physical properties.

	Peak 1								Peak 2					
	Mass	n	Integral	Normalized	Peak Height	Temperature Peak	Extrapolated Temperature Peak	Peak Width	Integral	Normalized	Peak Height	Temperature Peak	Extrapolated Temperature Peak	Peak Width
	mg		mJ	J/g	mW	°C	°C	°C	mJ	J/g	mW	°C	°C	°C
5 °C/min	69.51	1	475.16	6.84	2.81	820.67	820.12	13.97	1046.64	15.06	7.83	856.38	856.79	10.62
	126.65	2	1012.68	8.00	5.42	821.23	820.90	15.48	2040.90	16.11	14.01	858.51	858.65	11.36
	128.68	3	901.69	7.01	5.08	820.78	820.21	14.62	2182.88	16.96	14.45	857.49	857.62	11.62
	131.10	4	885.18	6.75	4.89	821.24	820.90	14.94	1996.25	15.23	14.12	856.99	857.16	11.02
	106.77	5	655.55	6.14	4.24	821.75	821.84	12.58	1871.69	17.53	13.47	854.71	854.90	10.81
	133.40	6	857.90	6.43	4.76	821.04	820.57	14.97	2036.72	15.27	14.25	857.74	857.93	11.18
	90.16	7	565.98	6.28	3.64	822.80	822.39	12.73	1626.57	18.04	11.59	856.42	856.65	10.98
	131.16	8	789.38	6.02	4.64	822.55	822.10	13.92	1977.61	15.08	13.90	857.97	857.93	11.20
	130.33	9	787.35	6.04	4.89	821.66	821.74	13.09	1943.30	14.91	13.81	855.33	855.70	11.08
	86.67	10	708.98	8.18	4.01	820.63	820.35	14.48	1402.54	16.18	9.96	856.65	856.96	11.03
Average	113.44		763.99	6.77	4.44	821.44	821.11	14.08	1812.51	16.04	12.74	856.82	857.03	11.09
SD	23.45		164.29	0.78	0.78	0.76	0.84	1.00	351.26	1.13	2.23	1.18	1.11	0.28
10 °C/min	140.16	1	1219.37	8.70	12.28	841.64	840.68	40.20	2759.39	19.70	33.12	864.32	864.62	12.84
	101.44	2	545.09	5.37	5.97	836.46	837.11	15.07	1797.77	17.72	23.51	867.48	867.63	11.91
	73.55	3	619.98	8.43	6.36	836.56	836.50	16.17	1181.82	16.07	16.31	868.62	868.71	11.36
	105.41	4	596.87	5.66	6.57	837.05	837.35	15.05	1428.15	13.55	19.65	868.63	868.60	11.36
	132.19	5	632.19	4.78	6.87	837.28	837.79	15.25	1618.91	12.25	22.81	868.61	868.57	11.20
	135.06	6	758.21	5.61	7.82	837.61	837.99	16.07	1770.99	13.11	24.12	868.97	869.04	11.48
	101.54	7	717.26	7.06	6.69	838.06	837.25	44.13	1899.99	18.71	22.82	863.51	863.65	12.85
	131.38	8	569.90	4.34	6.26	839.78	839.57	14.57	1944.01	14.80	25.26	867.63	867.72	11.88
	94.28	9	722.12	7.66	7.16	837.36	837.71	16.14	1732.86	18.38	21.10	868.97	869.06	12.59
	140.00	10	1008.69	7.20	10.39	840.34	839.90	40.75	2307.12	16.48	28.20	864.36	864.61	12.77
Average	115.50		738.97	6.48	7.64	838.21	838.19	23.34	1844.10	16.08	23.69	867.11	867.22	12.02
SD	23.16		215.14	1.53	2.06	1.76	1.38	12.72	440.64	2.58	4.61	2.17	2.09	0.68

Table 3A: DSC exothermic peak values for 5 and 10 °C/min.

	Peak 1								Peak 2					
	Mass	n	Integral	Normalized	Peak Height	Temperature Peak	Extrapolated Temperature Peak	Peak Width	Integral	Normalized	Peak Height	Temperature Peak	Extrapolated Temperature Peak	Peak Width
	mg		mJ	J/g	mW	°C	°C	°C	mJ	J/g	mW	°C	°C	°C
15 °C/min	52.71	1	461.64	8.76	6.72	849.28	848.05	42.52	994.71	18.87	16.79	872.31	872.44	13.93
	78.32	2	458.51	5.85	6.67	847.88	848.07	17.06	1112.46	14.20	20.71	874.27	874.45	12.42
	78.34	3	803.60	10.25	12.88	855.00	850.74	37.27	1761.07	22.48	29.41	870.86	871.21	14.99
	93.40	4	421.65	4.51	7.12	846.93	847.14	14.47	1052.53	11.27	22.02	875.10	875.10	11.35
	62.23	5	562.74	9.04	9.03	853.40	850.43	36.29	1159.28	18.63	21.10	869.98	870.53	13.62
	70.91	6	328.97	4.64	4.93	851.32	851.32	17.08	800.46	11.29	15.73	875.65	875.69	11.88
	73.18	7	603.70	8.25	10.68	853.61	850.59	35.15	1388.58	18.97	24.56	869.73	870.22	13.47
	92.69	8	381.10	4.11	6.28	847.06	847.26	15.02	989.22	10.67	21.66	875.07	875.13	10.88
	84.84	9	414.41	4.88	6.90	846.93	847.54	14.75	861.76	10.16	19.07	875.15	875.27	10.77
	90.52	10	641.06	7.08	9.31	849.73	848.39	40.49	1321.87	14.60	24.60	871.47	871.84	12.48
Average	77.71		507.74	6.74	8.05	850.11	848.95	27.01	1144.19	15.11	21.57	872.96	873.19	12.58
SD	13.41		143.84	2.23	2.39	3.05	1.62	12.15	283.97	4.35	4.00	2.34	2.15	1.40
20 °C/min	122.84	Not Applicable							2656.45	21.63	36.79	879.32	879.88	15.58
	128.10								3795.30	29.63	57.50	871.95	871.28	21.86
	136.00								3616.14	26.59	48.72	878.60	878.99	26.51
	90.12								2168.55	24.06	29.32	880.33	880.05	14.89
	92.01								2824.44	30.70	38.57	879.43	879.39	15.57
	72.76								2221.99	30.54	30.52	879.27	878.99	15.14
	53.73								1951.58	36.32	26.76	878.64	878.27	15.92
	75.61								2875.88	38.04	37.75	877.26	877.45	26.31
	52.97								1968.00	37.15	25.63	875.40	875.92	26.62
	56.27								2254.94	40.07	29.32	874.55	874.70	26.17
Average	88.04								2633.33	31.47	36.09	877.48	877.49	20.46
SD	31.52								653.86	6.27	10.25	2.68	2.78	5.49

Table 3B: DSC exothermic peak values for 15 and 20 °C/min.

	Peak 1								Peak 2					
	Mass	n	Integral	Normalized	Peak Height	Temperature Peak	Extrapolated Temperature Peak	Peak Width	Integral	Normalized	Peak Height	Temperature Peak	Extrapolated Temperature Peak	Peak Width
	mg		mJ	J/g	mW	°C	°C	°C	mJ	J/g	mW	°C	°C	°C
Two-Stage Heating Schedule (1st-stage, 90 °C/min) (2nd-stage, 30 °C/min)	158.40	1	560.88	3.54	18.74	812.07	814.27	20.80	10130.00	63.94	69.17	855.05	855.00	4.86
	93.91	2	294.66	3.14	10.32	817.48	817.34	19.20	5793.32	61.69	37.19	854.49	854.26	7.06
	197.38	3	955.84	4.84	30.10	811.89	813.52	23.00	13920.00	70.52	78.39	854.56	854.13	7.54
	159.42	4	1202.58	7.54	33.54	812.80	813.55	53.08	14760.00	92.58	78.13	854.83	854.59	9.42
	168.45	5	1366.84	8.11	37.72	815.31	814.04	52.72	17170.00	101.92	89.37	854.35	854.08	11.49
	185.46	6	1414.17	7.63	37.96	815.08	813.81	52.80	17620.00	94.98	100.85	855.09	855.05	8.29
	132.11	7	566.24	4.29	19.16	812.87	814.32	20.04	8697.60	65.84	62.00	855.11	855.07	4.43
	142.54	8	1024.79	7.19	28.64	815.95	814.82	51.66	12800.00	89.83	70.89	854.35	854.20	11.11
	118.83	9	973.49	8.19	26.65	816.92	815.49	51.22	11300.00	95.07	73.48	855.08	855.18	7.76
	137.60	10	716.51	5.21	21.28	816.06	815.34	50.62	10860.00	78.90	62.18	854.55	854.36	8.69
Average	149.41		907.60	5.97	26.41	814.64	814.65	39.51	12305.09	81.53	72.17	854.75	854.59	8.07
SD	30.99		368.76	1.97	8.99	2.06	1.17	16.19	3712.47	15.09	17.10	0.32	0.44	2.31

Table 3C: DSC exothermic peak values for the two-stage heating schedule (820-840 °C).

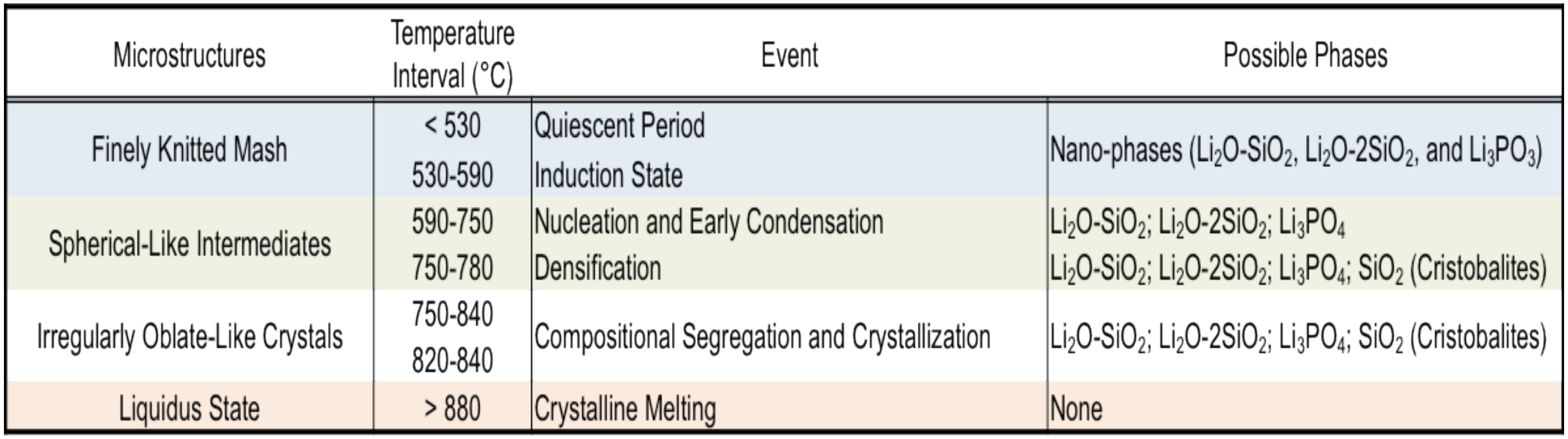

Microstructures	Temperature Interval (°C)	Event	Possible Phases
Finely Knitted Mash	< 530	Quiescent Period	Nano-phases (Li_2O-SiO_2, Li_2O-$2SiO_2$, and Li_3PO_3)
	530-590	Induction State	
Spherical-Like Intermediates	590-750	Nucleation and Early Condensation	Li_2O-SiO_2; Li_2O-$2SiO_2$; Li_3PO_4
	750-780	Densification	Li_2O-SiO_2; Li_2O-$2SiO_2$; Li_3PO_4; SiO_2 (Cristobalites)
Irregularly Oblate-Like Crystals	750-840 820-840	Compositional Segregation and Crystallization	Li_2O-SiO_2; Li_2O-$2SiO_2$; Li_3PO_4; SiO_2 (Cristobalites)
Liquidus State	> 880	Crystalline Melting	None

Table 4: The evolutionary process of IPS e.max® CAD.

9. Figures

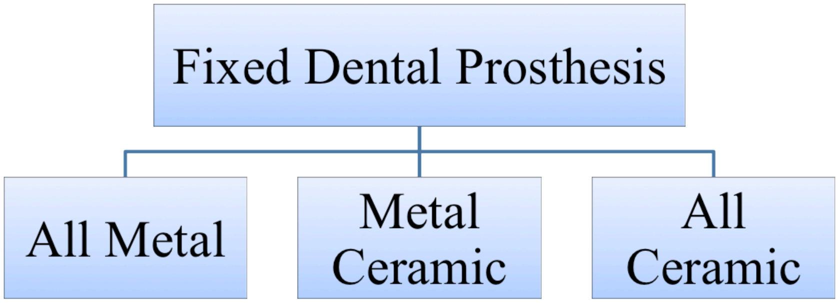

Figure 1: Classification of fixed dental prosthesis.

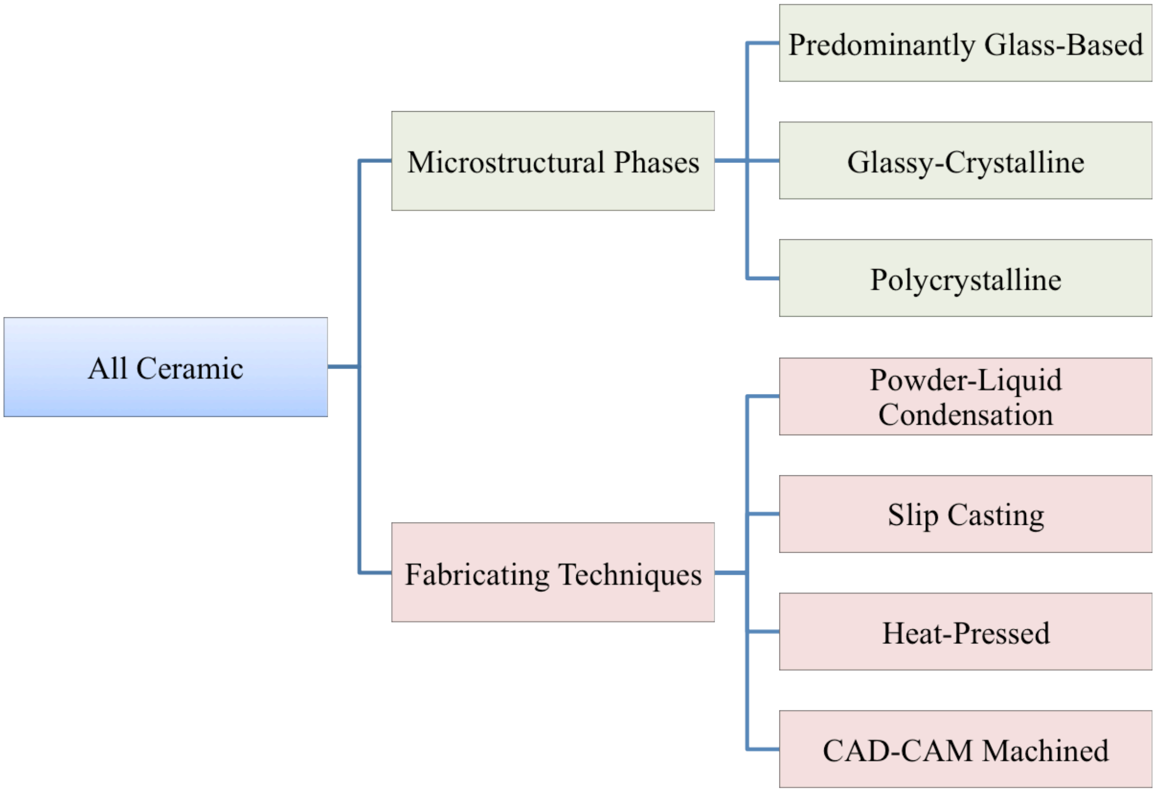

Figure 2: Classification of all ceramic fixed dental prosthesis.

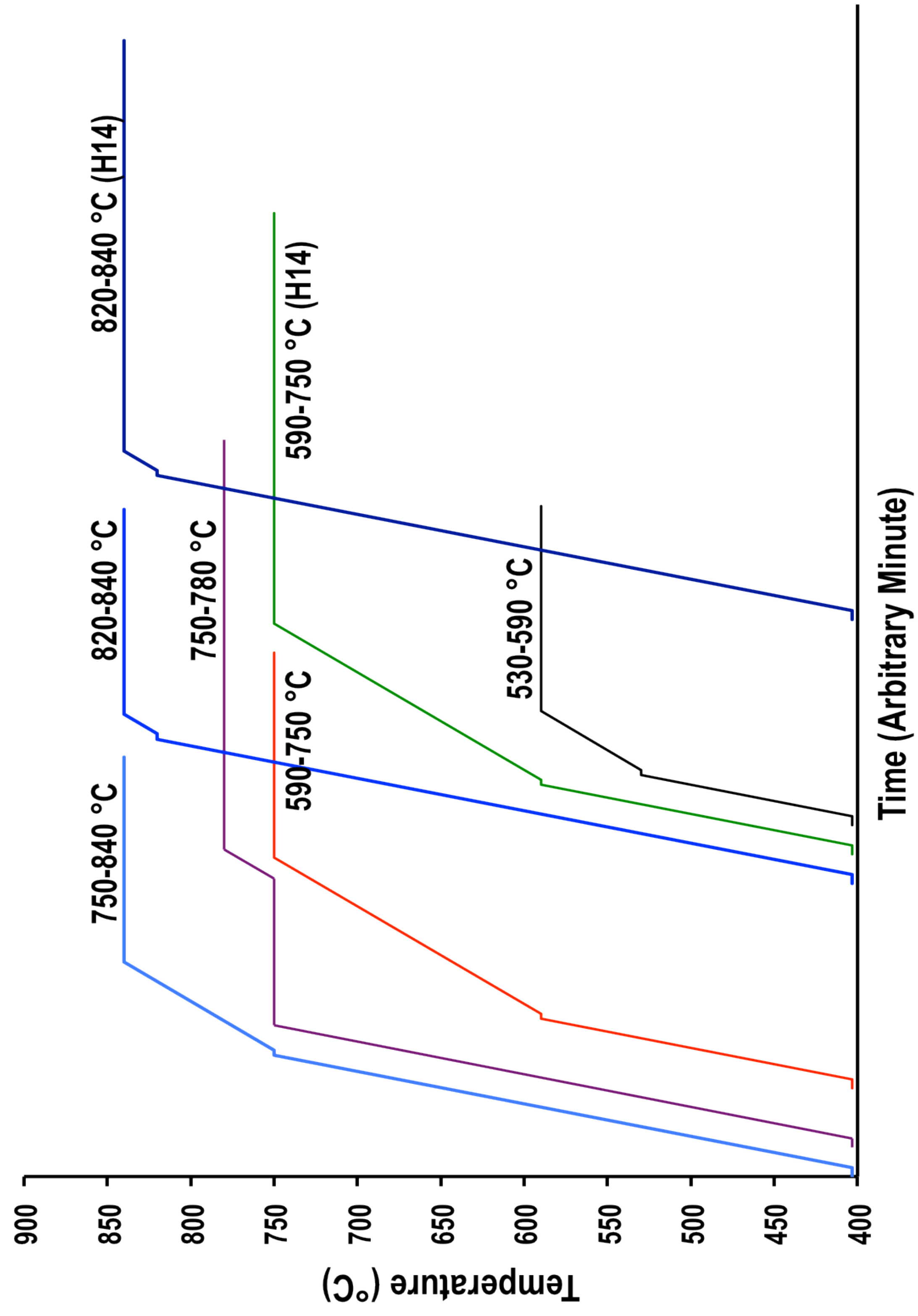

Figure 3: Graphical representation of Table 1.

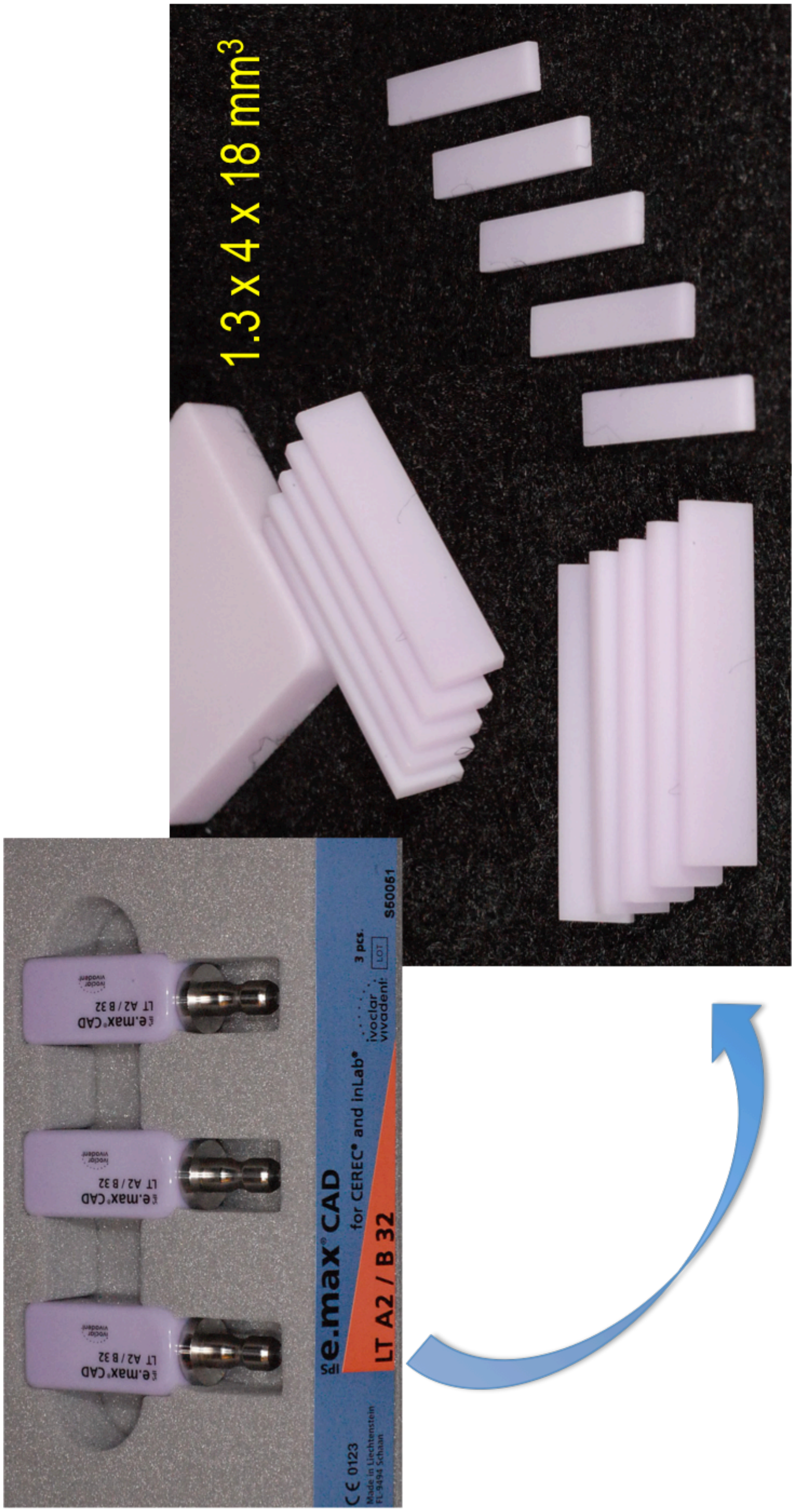

Figure 4: Prepared specimens from the IPS e.max® CAD blocs.

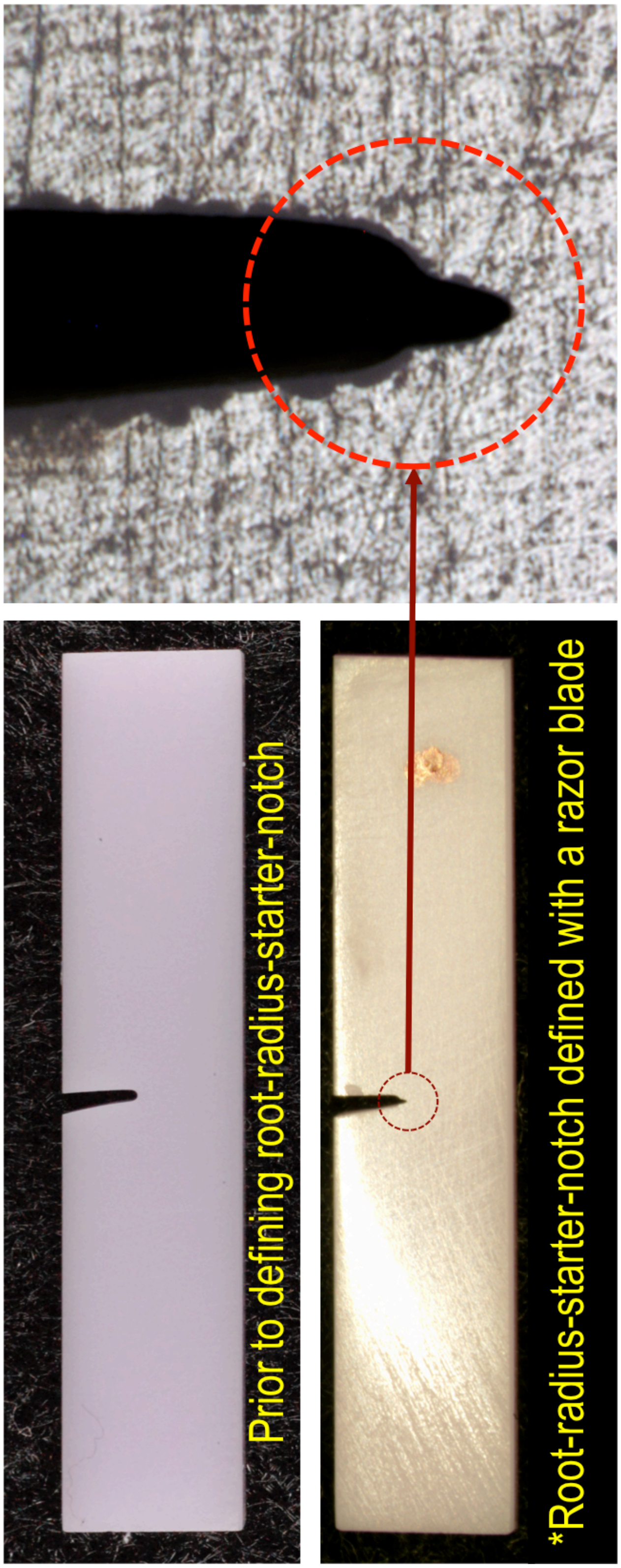

Figure 5: Examples of prepared specimens for fracture toughness testing. The enlarged red circle showed root radius with defined starter notch. *Starter notch was created prior to any heat treatment.

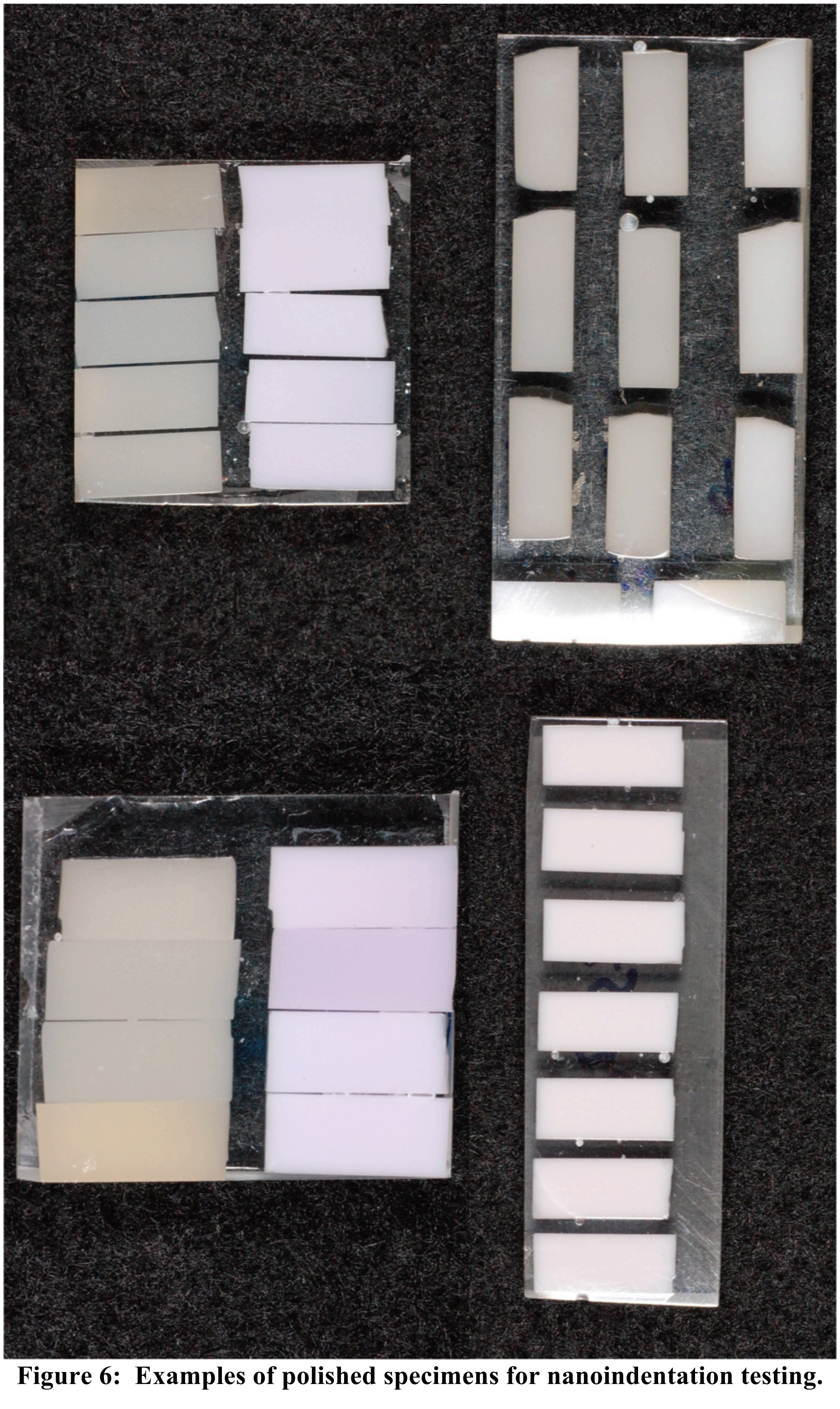

Figure 6: Examples of polished specimens for nanoindentation testing.

Figure 7: Examples of specimens prepared for DSC testing.

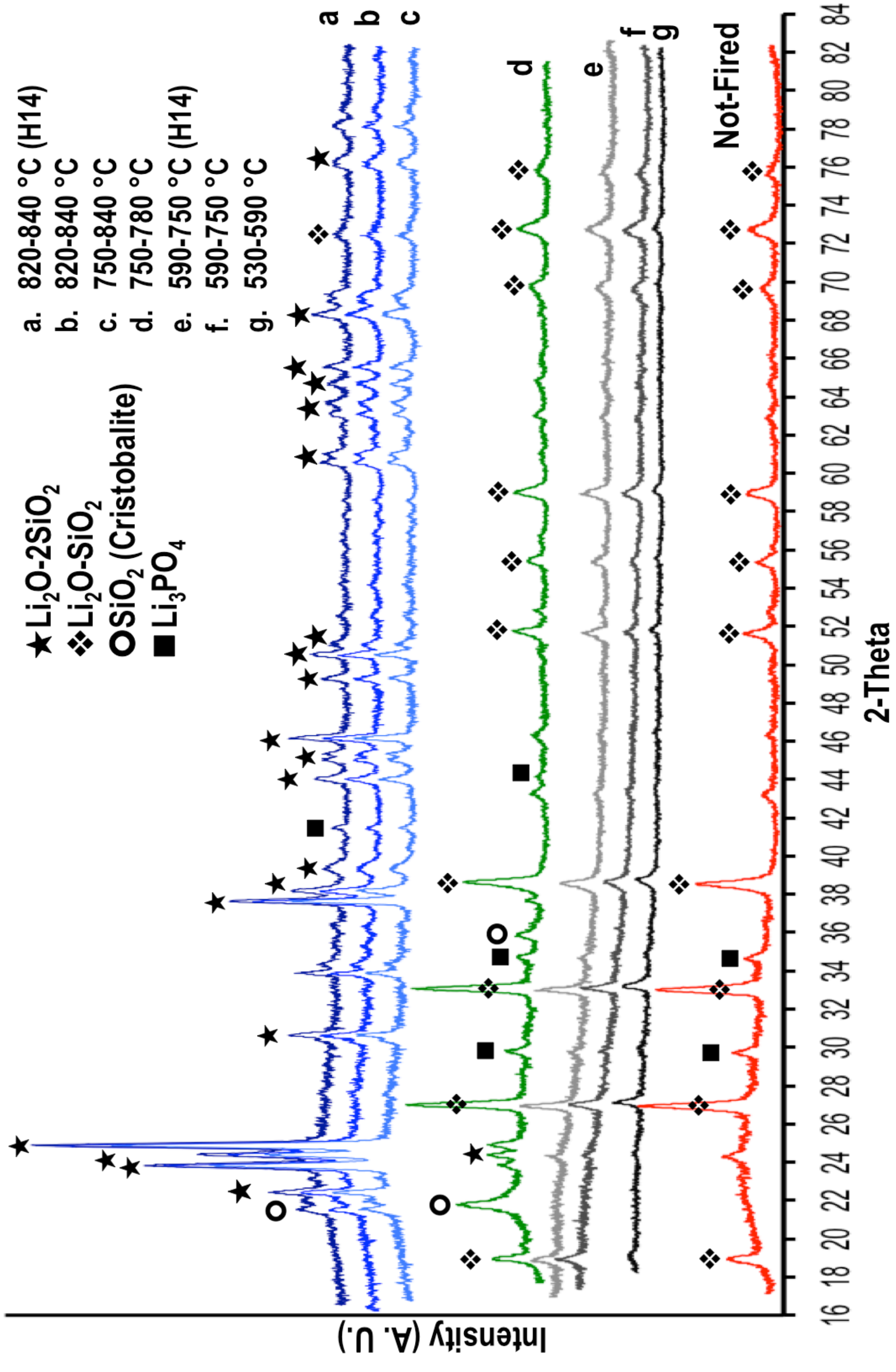

Figure 8: X-ray- diffraction.

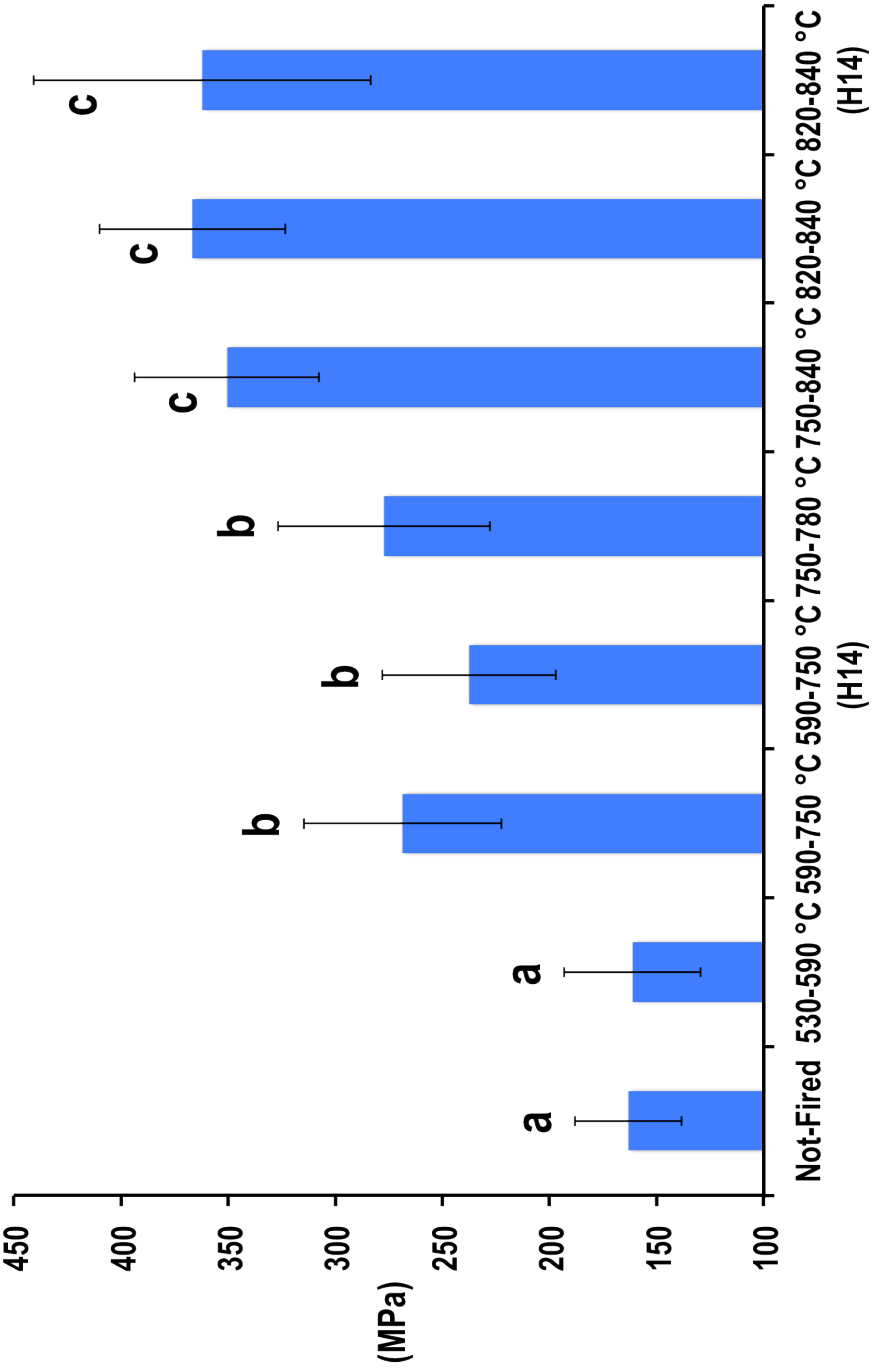

Figure 9: Flexural strength (n = 12 per group).
Groups with the same letter per column are not significantly different (p>0.05).

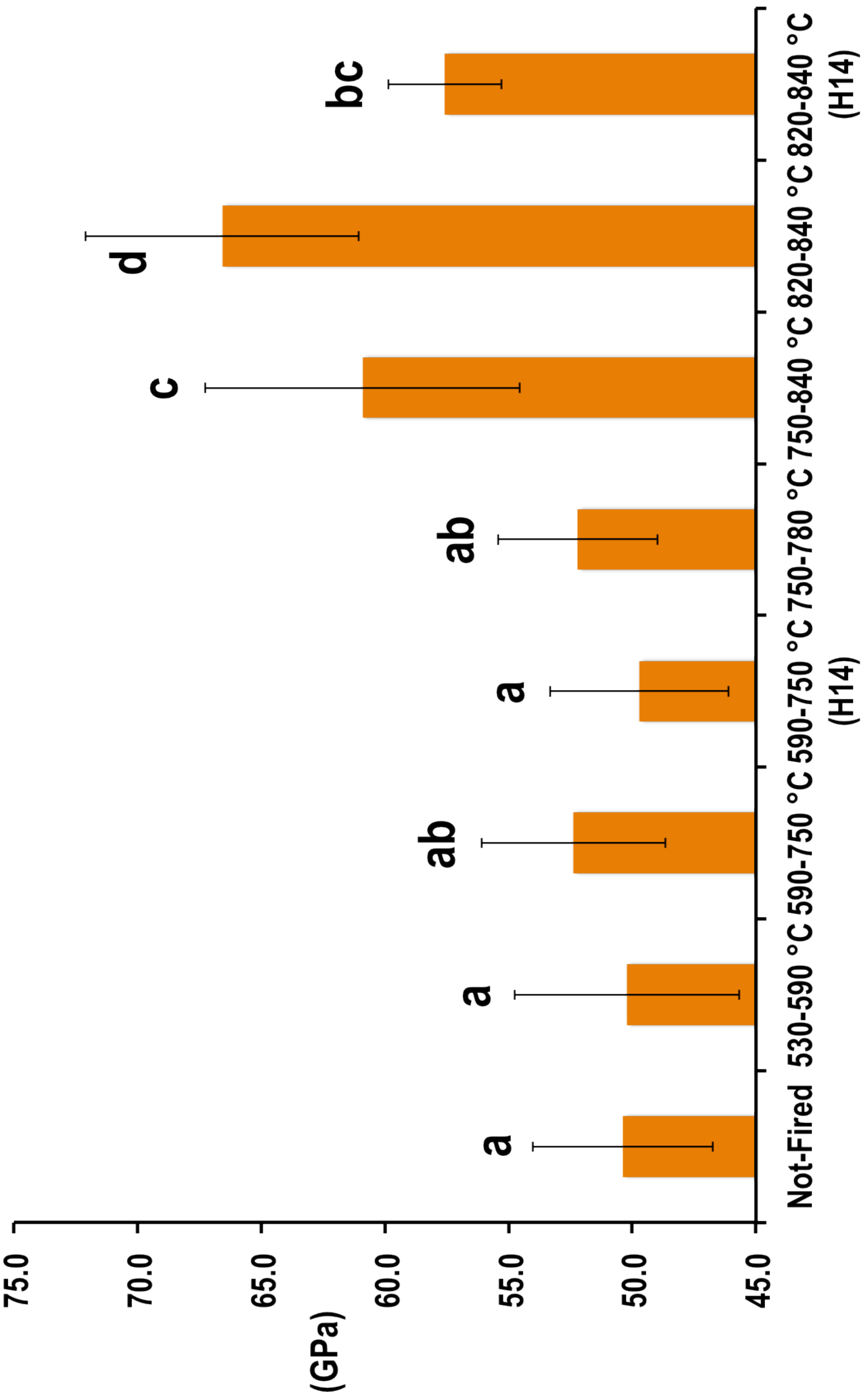

Figure 10: Flexural modulus (n = 12 per group).
Groups with the same letter per column are not significantly different (p>0.05).

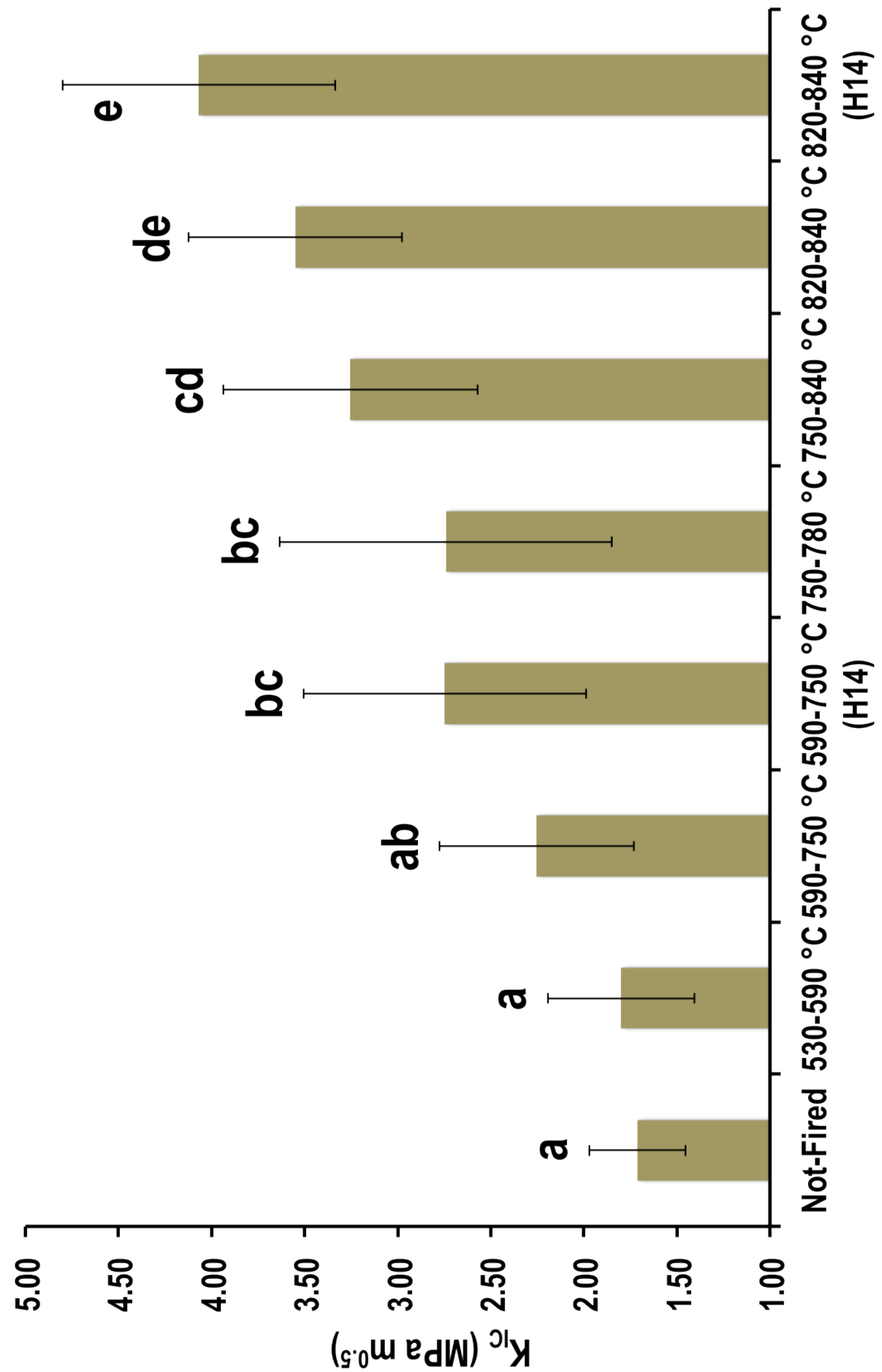

Figure 11: Fracture toughness (n = 12 per group).
Groups with the same letter per column are not significantly different (p>0.05).

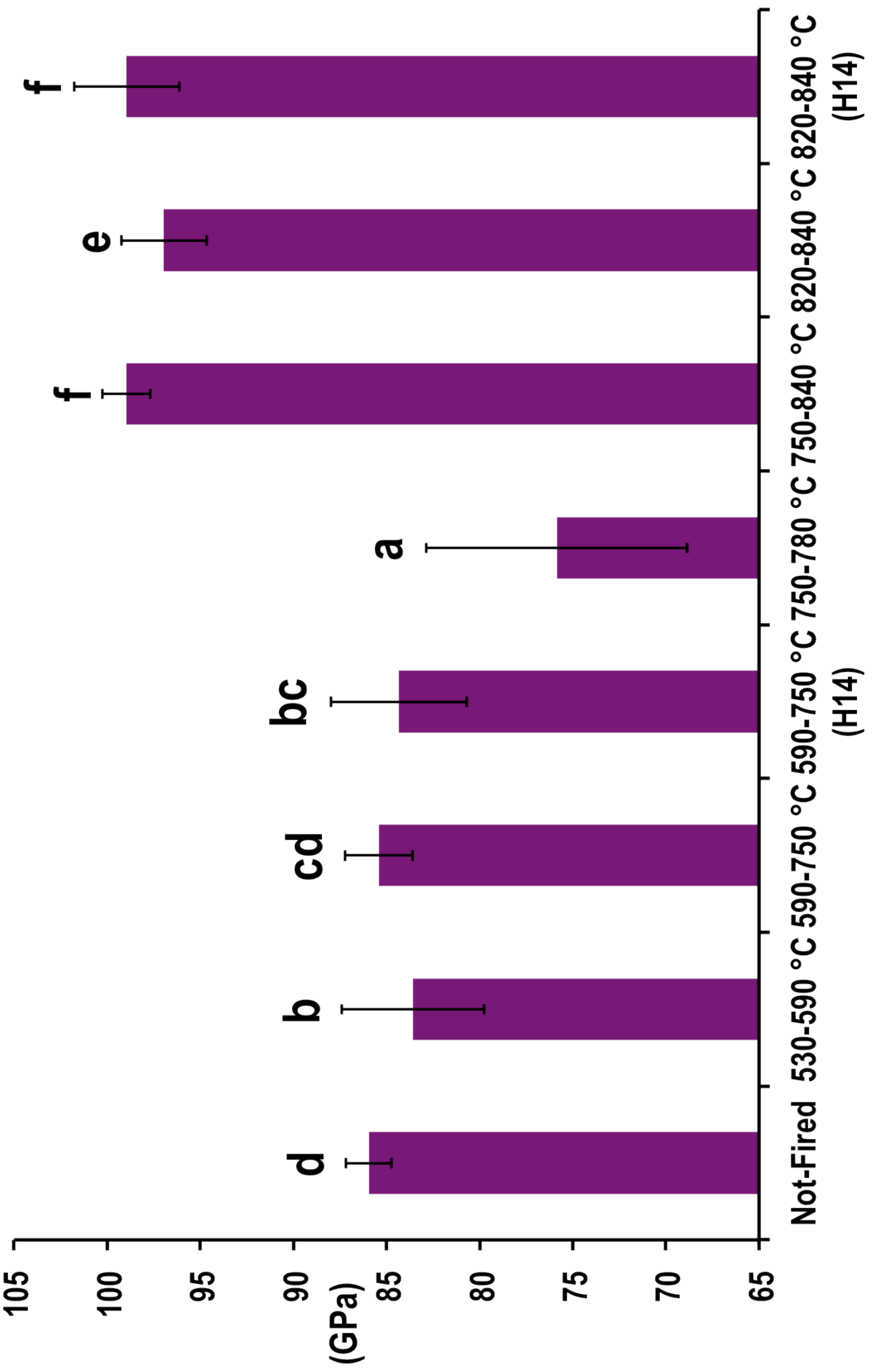

Figure 12: Elastic modulus – nanoindentation (n = 100 per group).
Groups with the same letter per column are not significantly different (p>0.05).

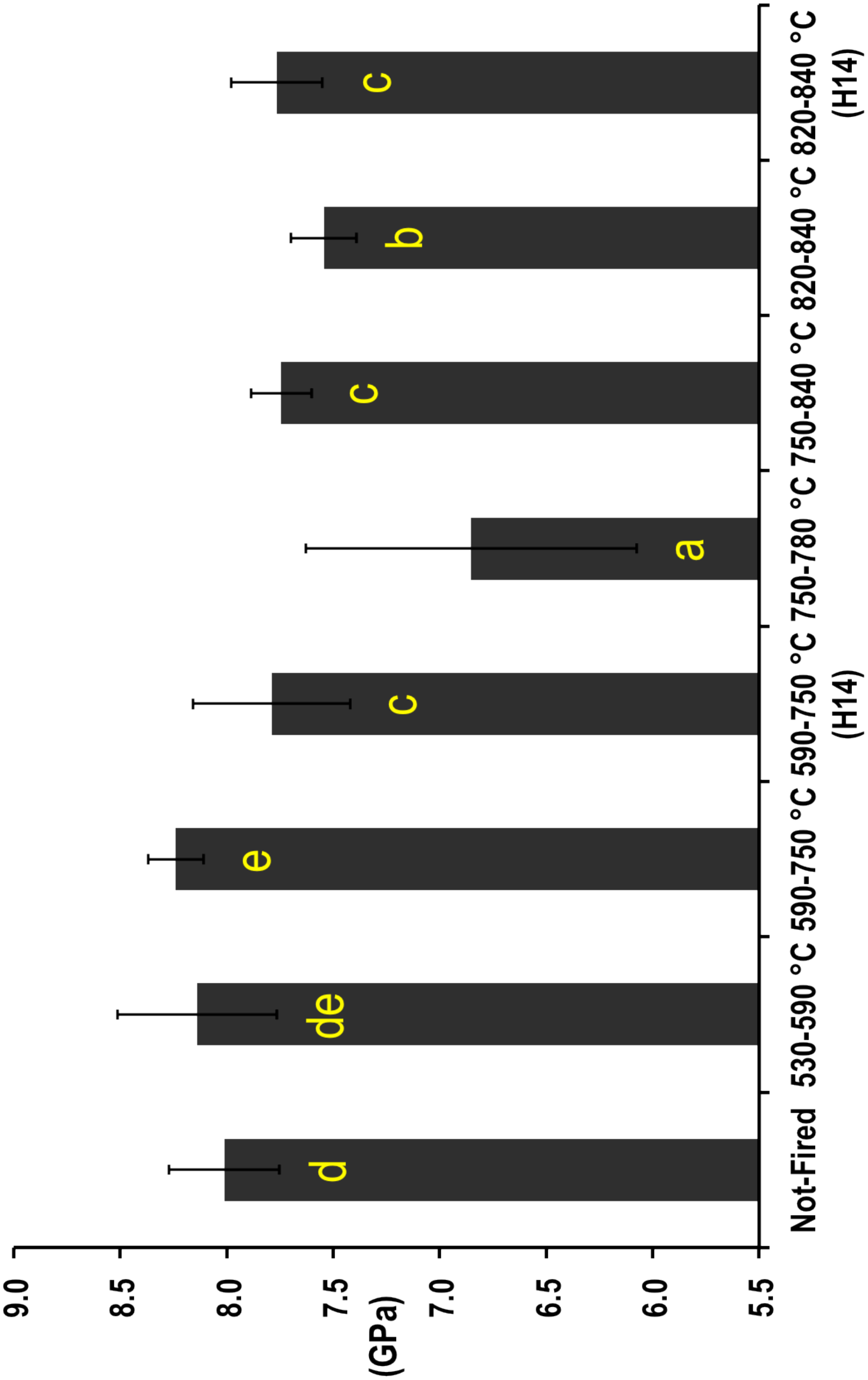

Figure 13: Surface hardness – nanoindentation (n = 100 per group).
Groups with the same letter per column are not significantly different (p>0.05).

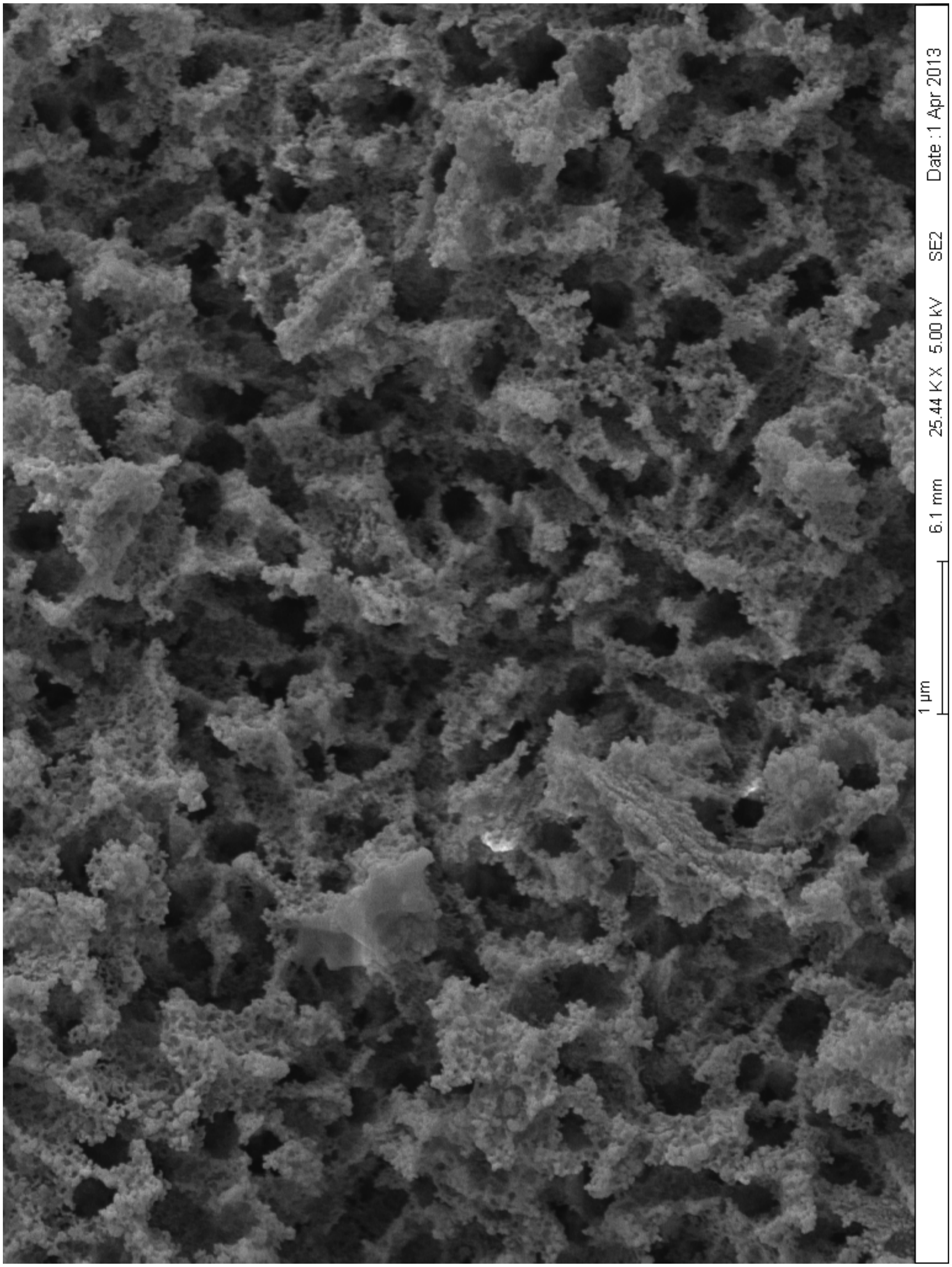

Figure 14A: A representative SEM image of the Not-Fired group.

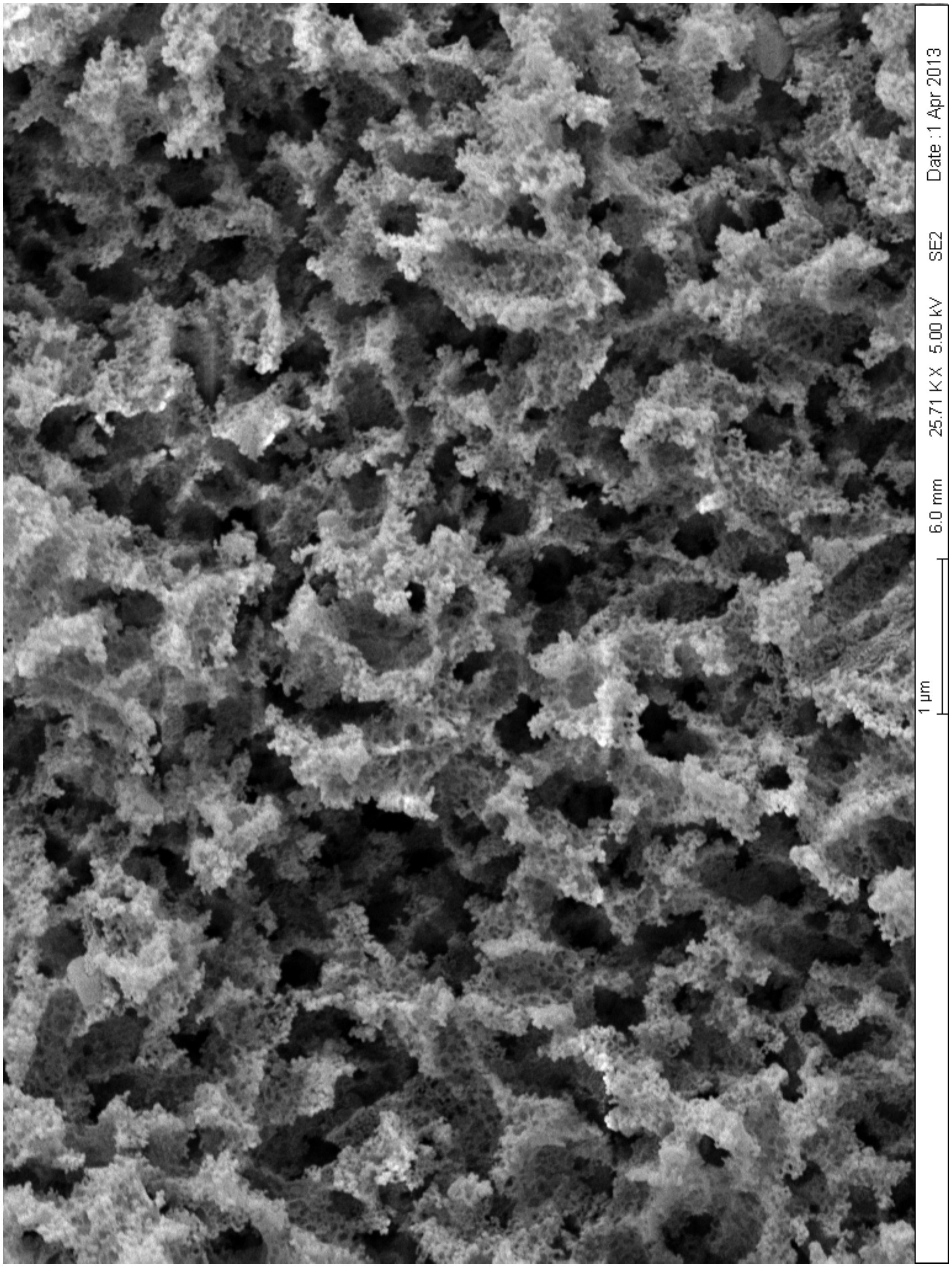

Figure 14B: A representative SEM image of the 530-590 °C group.

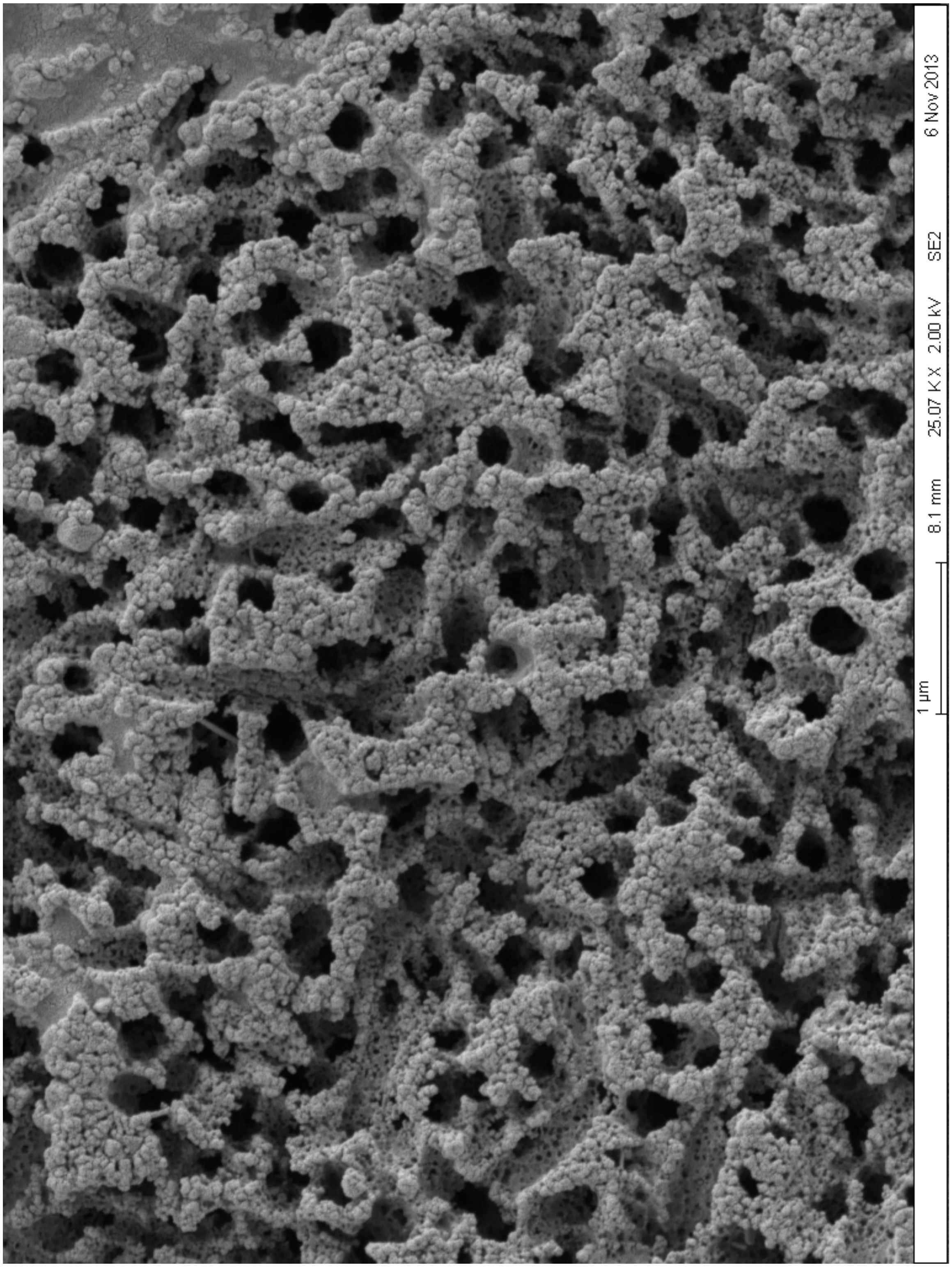

Figure 14C: A representative SEM image of the 590-750 °C group.

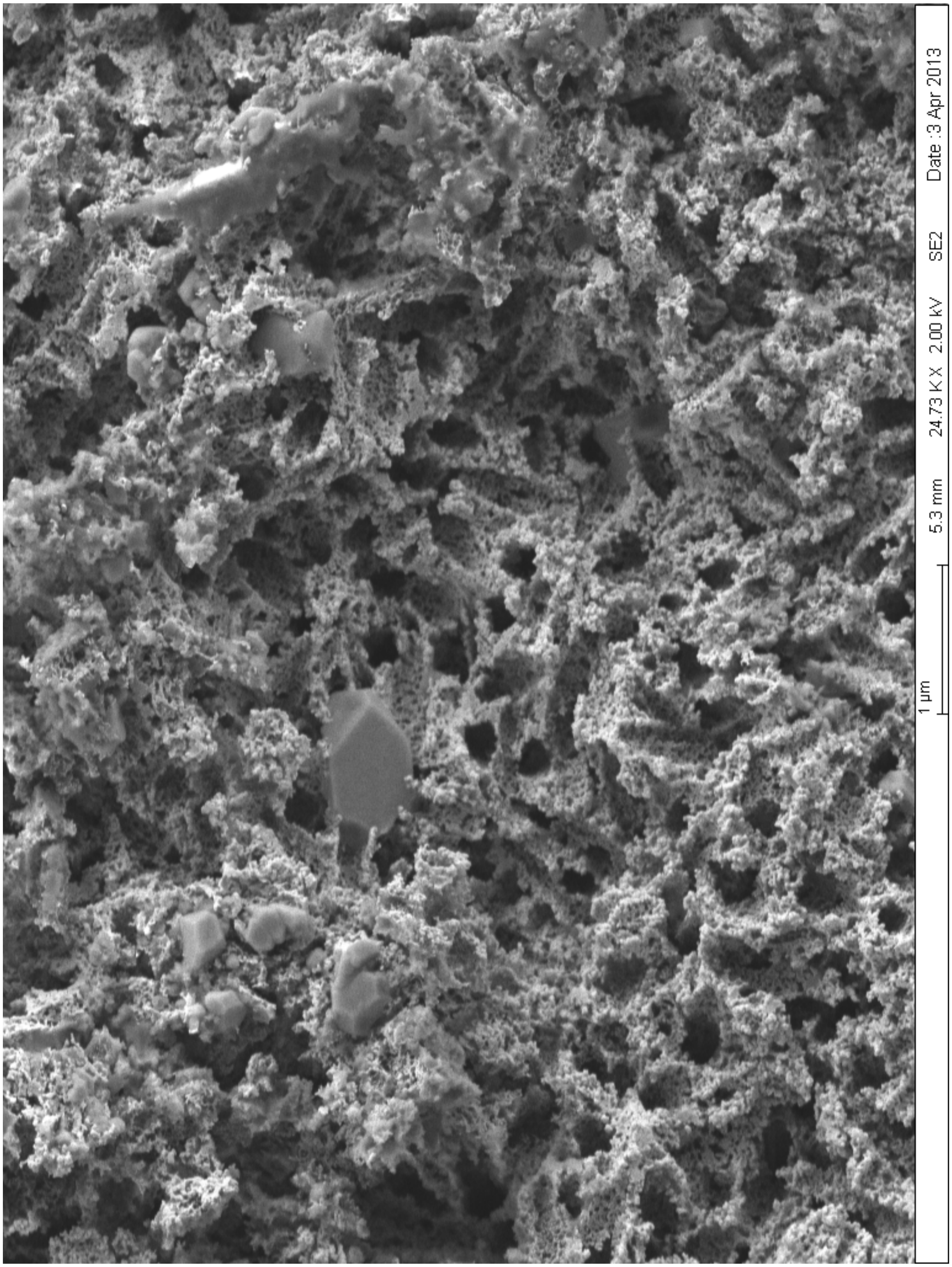

Figure 14D: A representative SEM image of the 590-750 °C (H14) group.

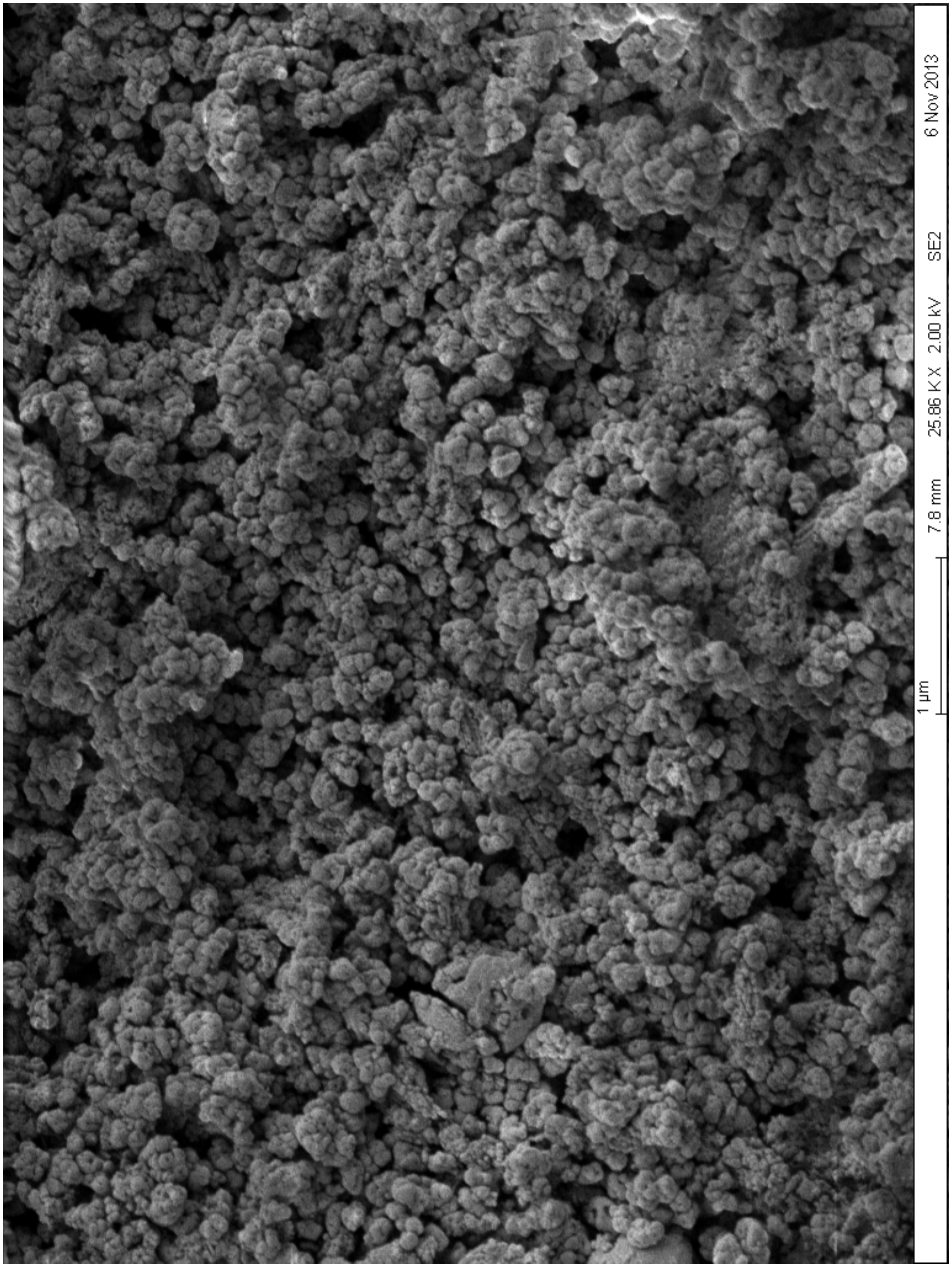

Figure 14E(1): First representative SEM image of the 750-780 °C group.

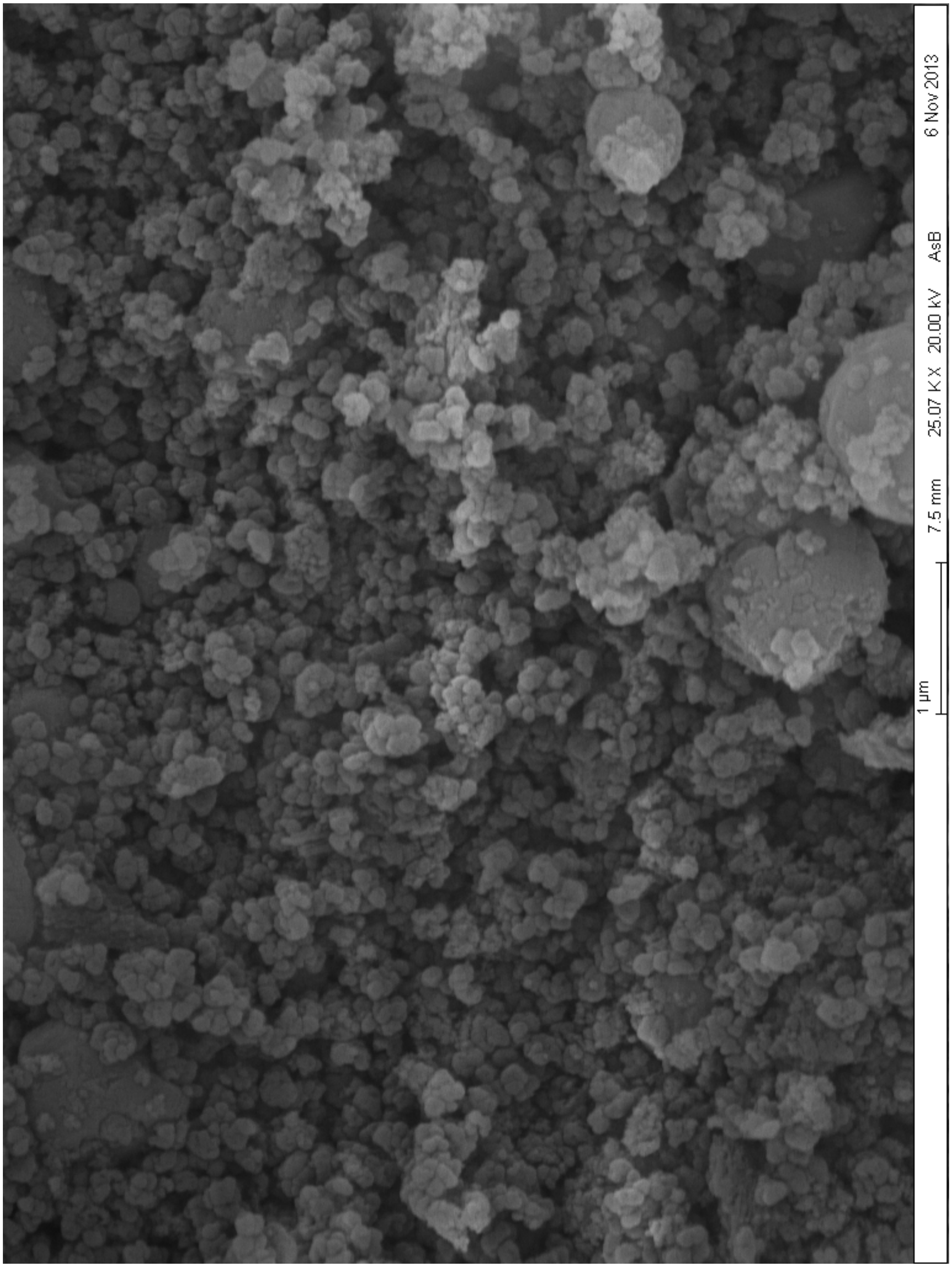

Figure 14E(2): Second representative SEM image of the 750-780 °C group.

Figure 14F: A representative SEM image of the 750-840 °C group.

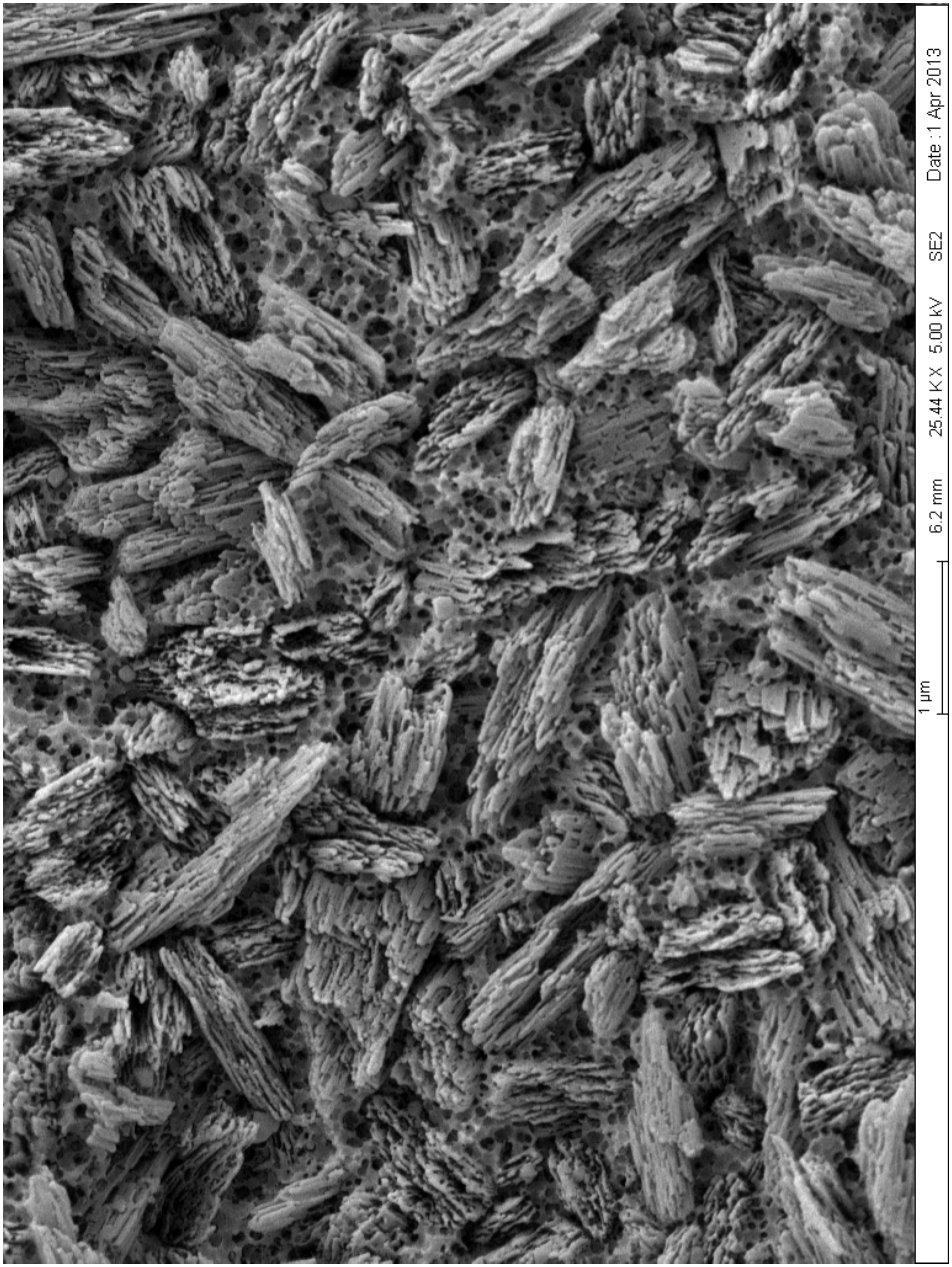

Figure 14G: A representative SEM image of the 820-840 °C (recommended) group.

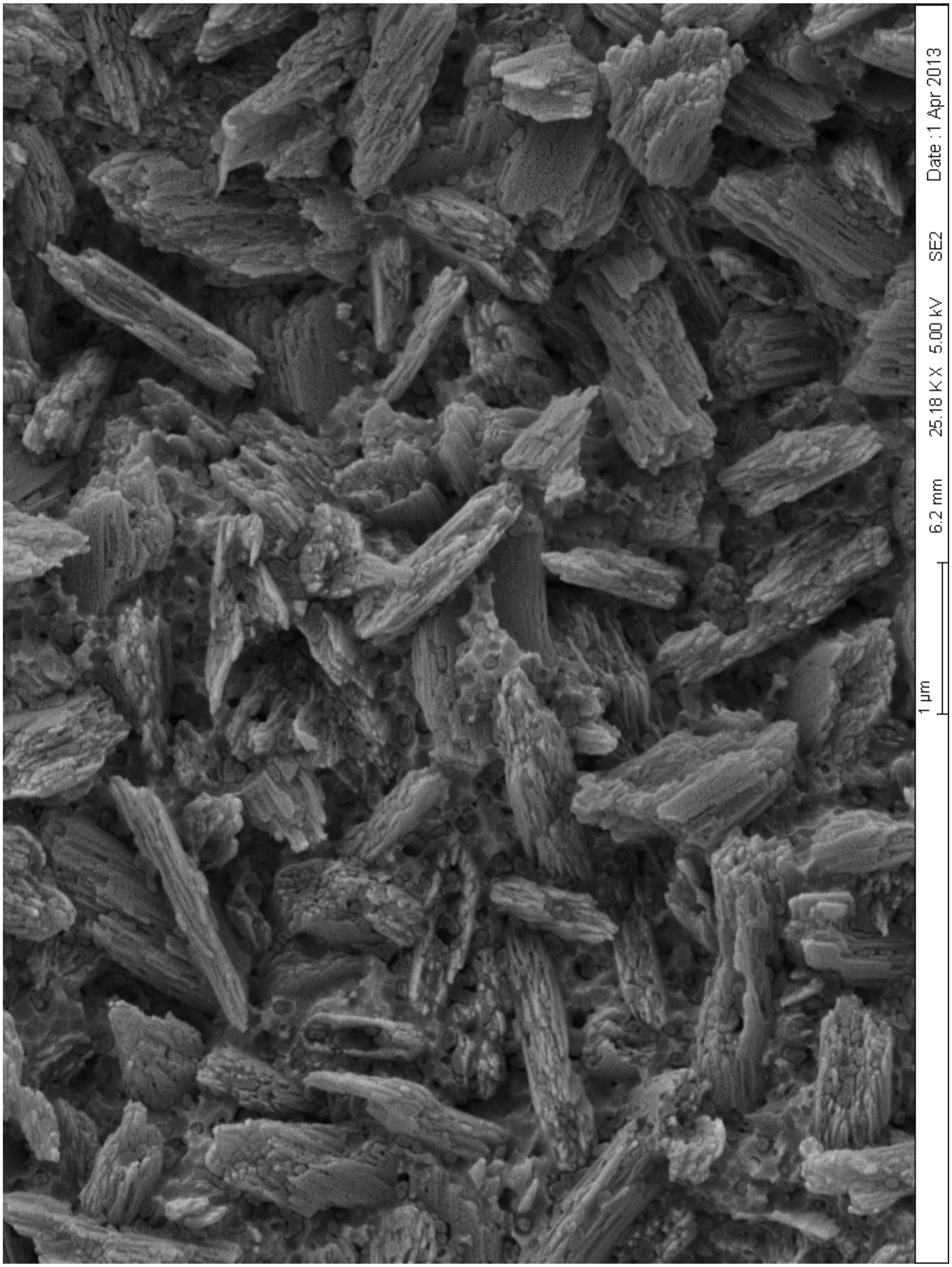

Figure 14H: A representative SEM image of the 820-840 °C (H14) group.

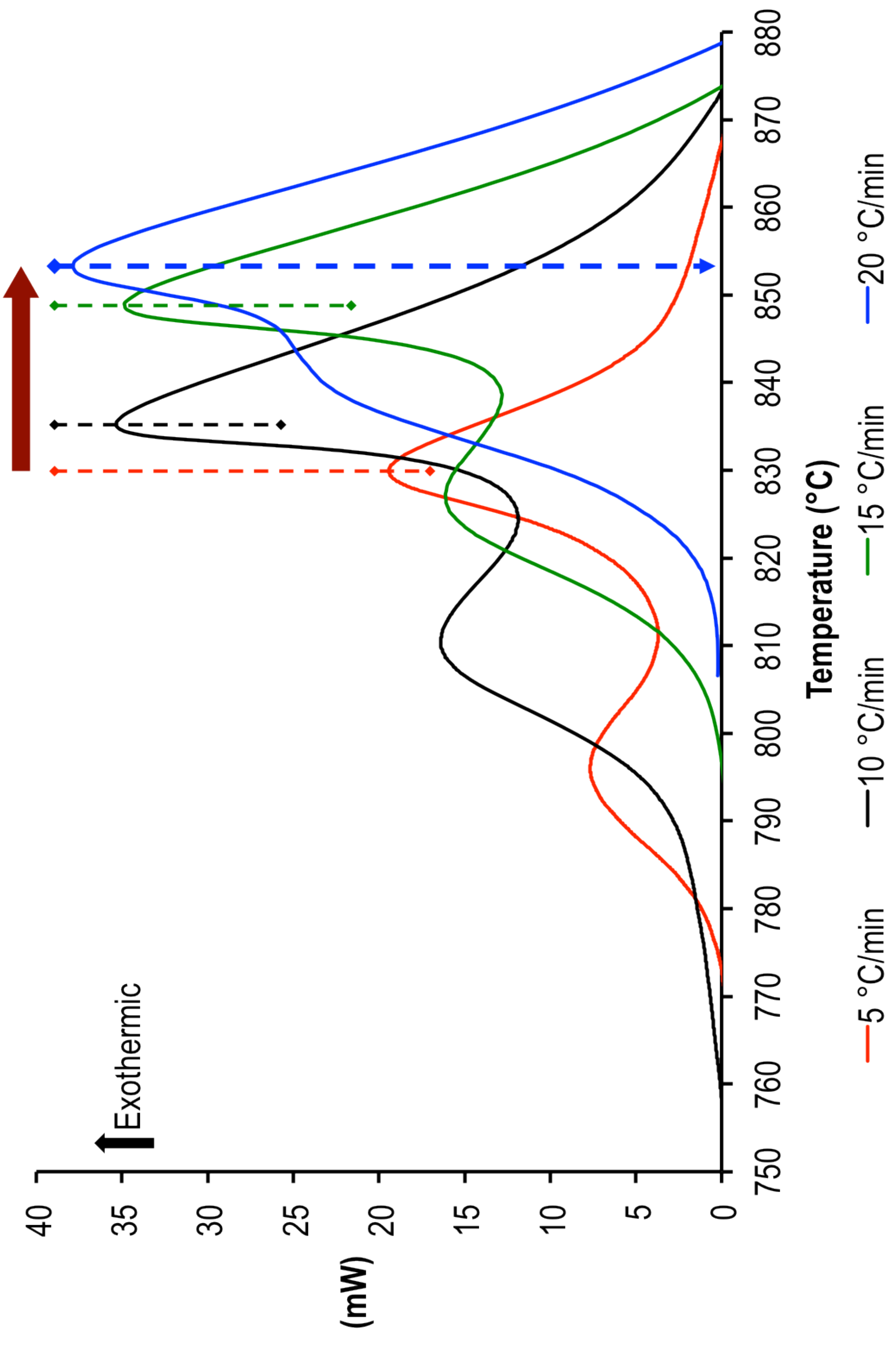

Figure 15: Representative DSC curves for heating rates: 5, 10, 15, & 20 °C/min. The maroon arrow showed shifting of the successive peak-2 temperatures to the right as the heating rate was increased.

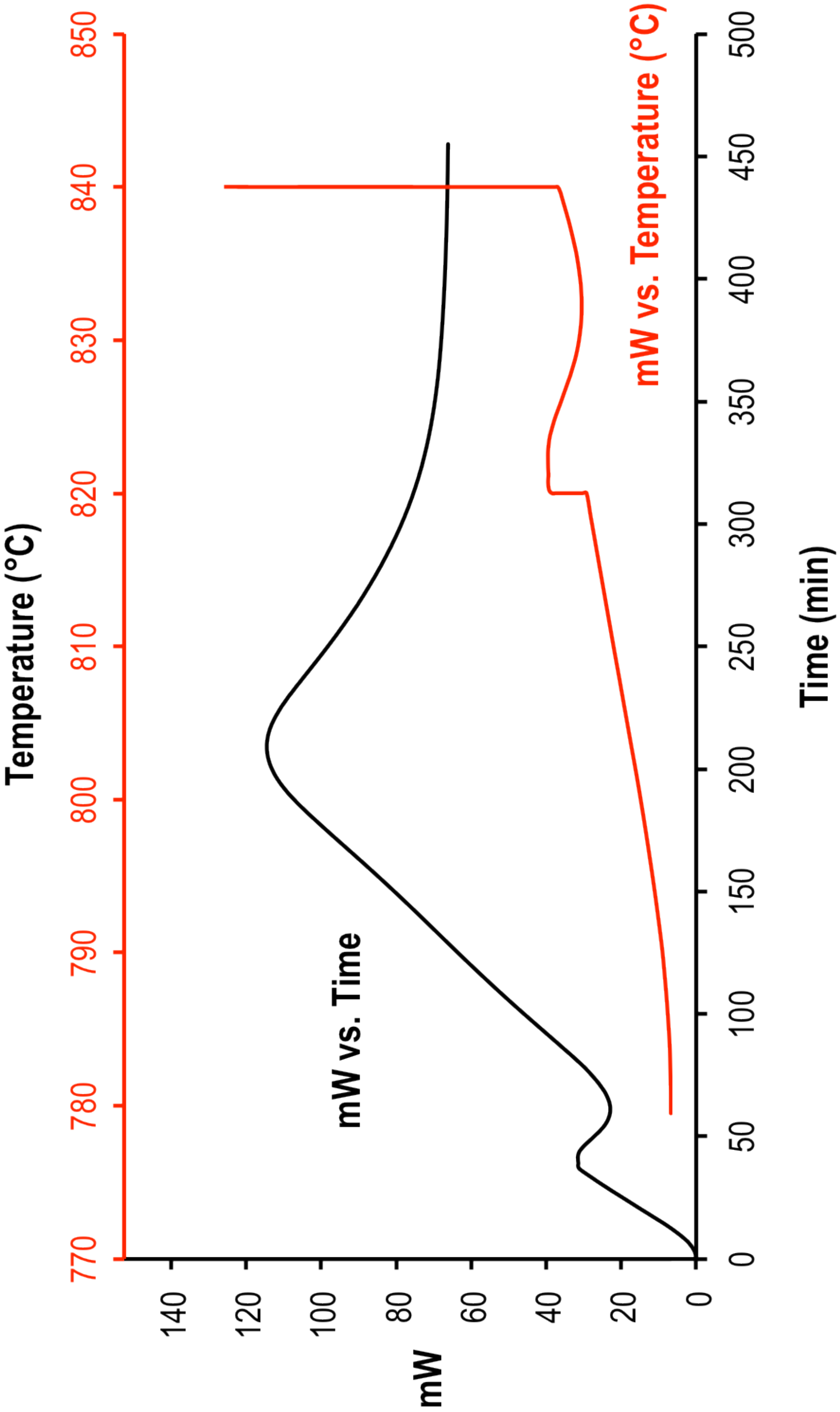

Figure 16: Representative DSC curves for the manufacturer's two-stage heating schedule. The black and red curves are the same except the red curve was plotted against temperature instead of time.

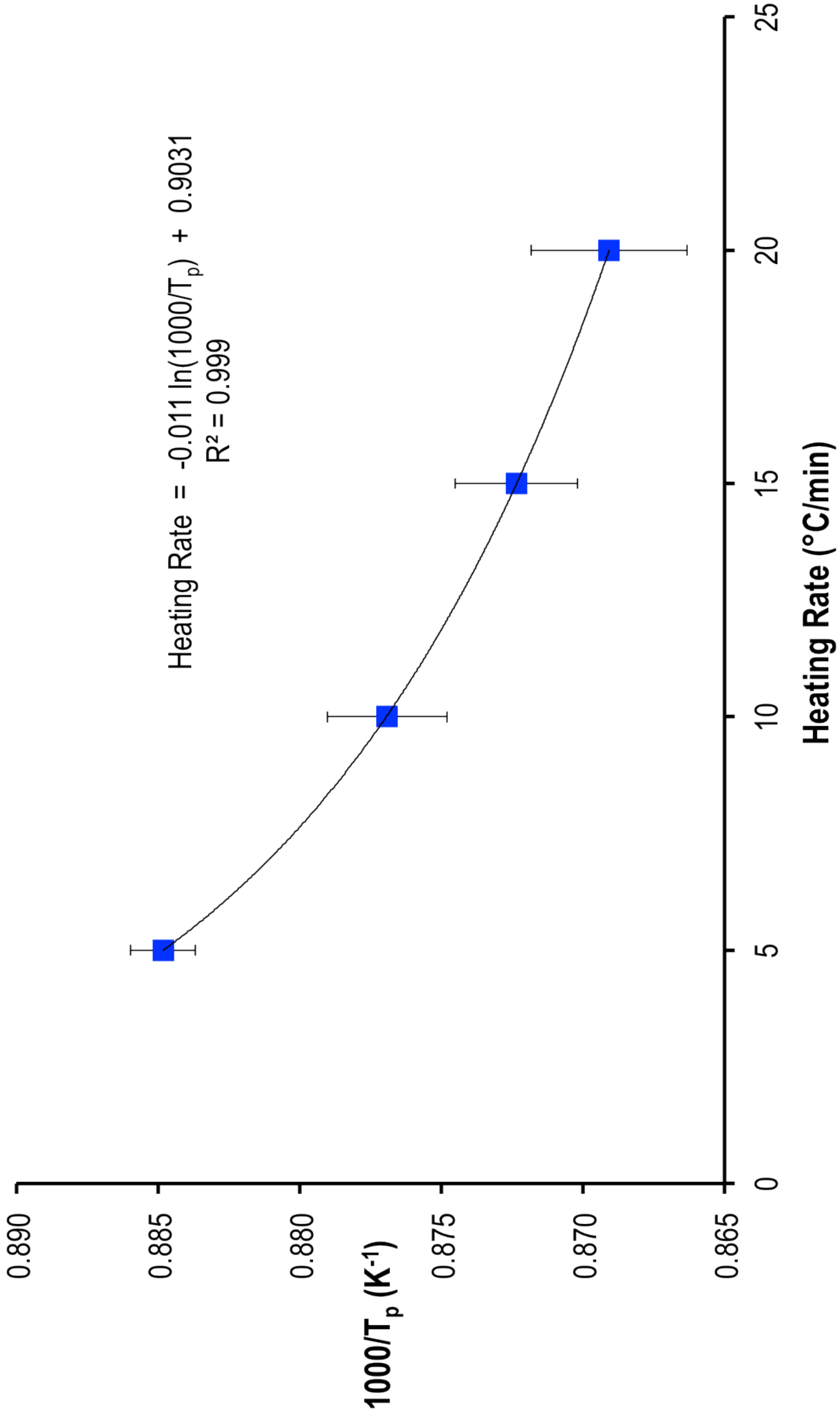

Figure 17: Relationship between heating rates and extrapolated peak-2 temperatures.

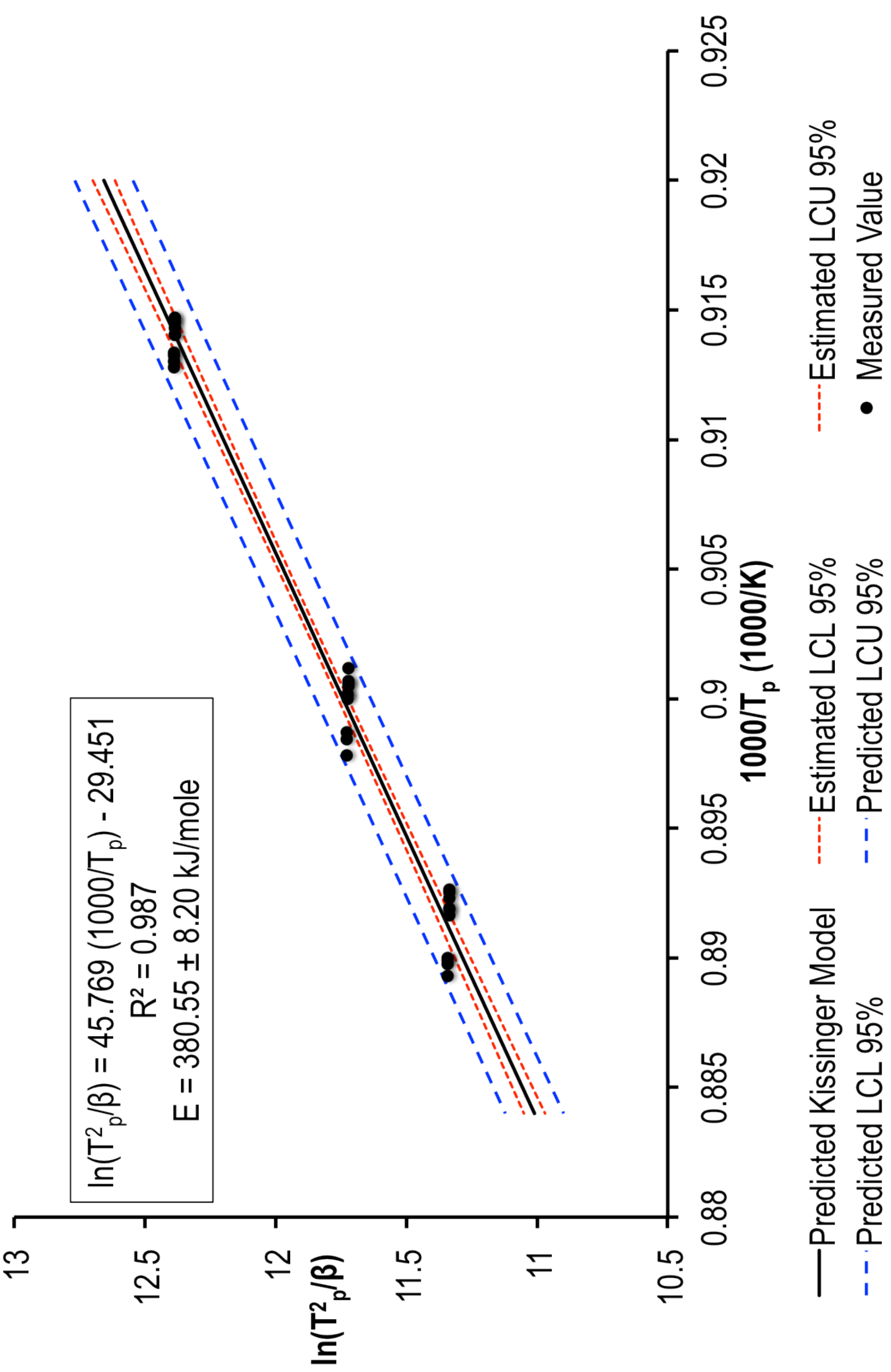

Figure 18A: Non-isothermal kinetics for lithium metasilicate crystallization (peak-1).

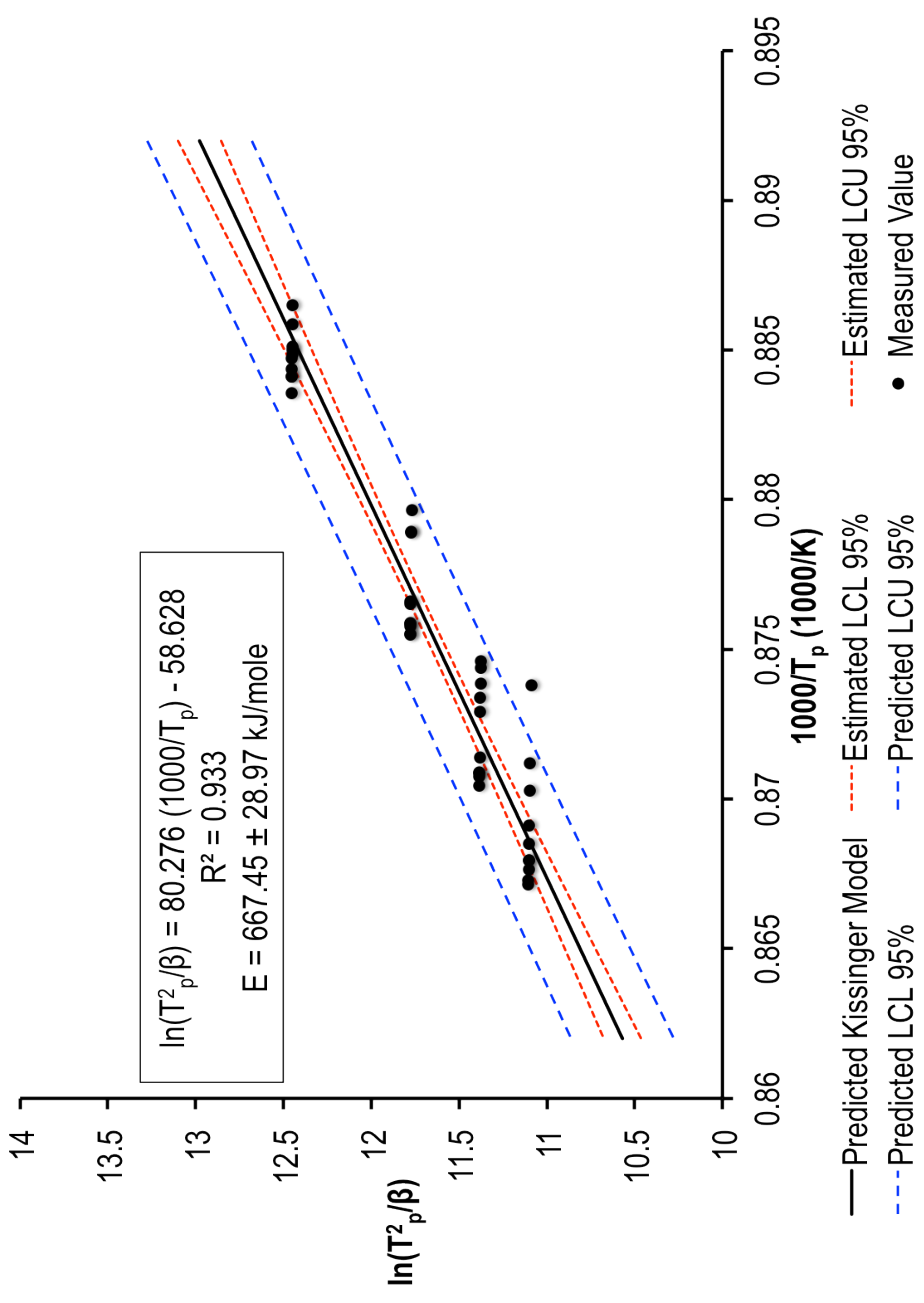

Figure 18B: Non-isothermal kinetics for lithium disilicate crystallization (peak-2).

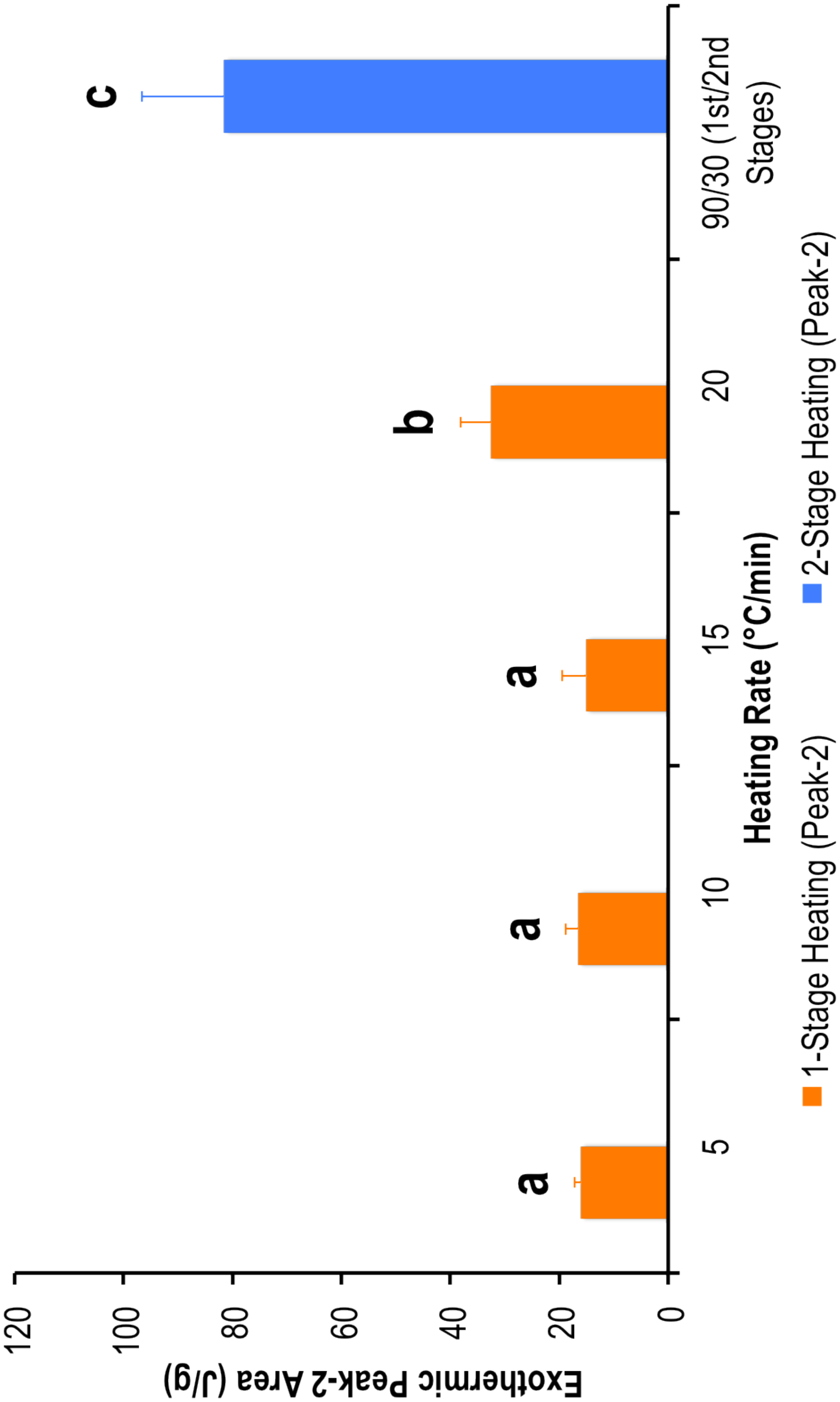

Figure 19: Exothermic peak-2 areas of single-stage vs. two-stage heating schedules. Groups with the same letter per column are not significantly different (p>0.05).

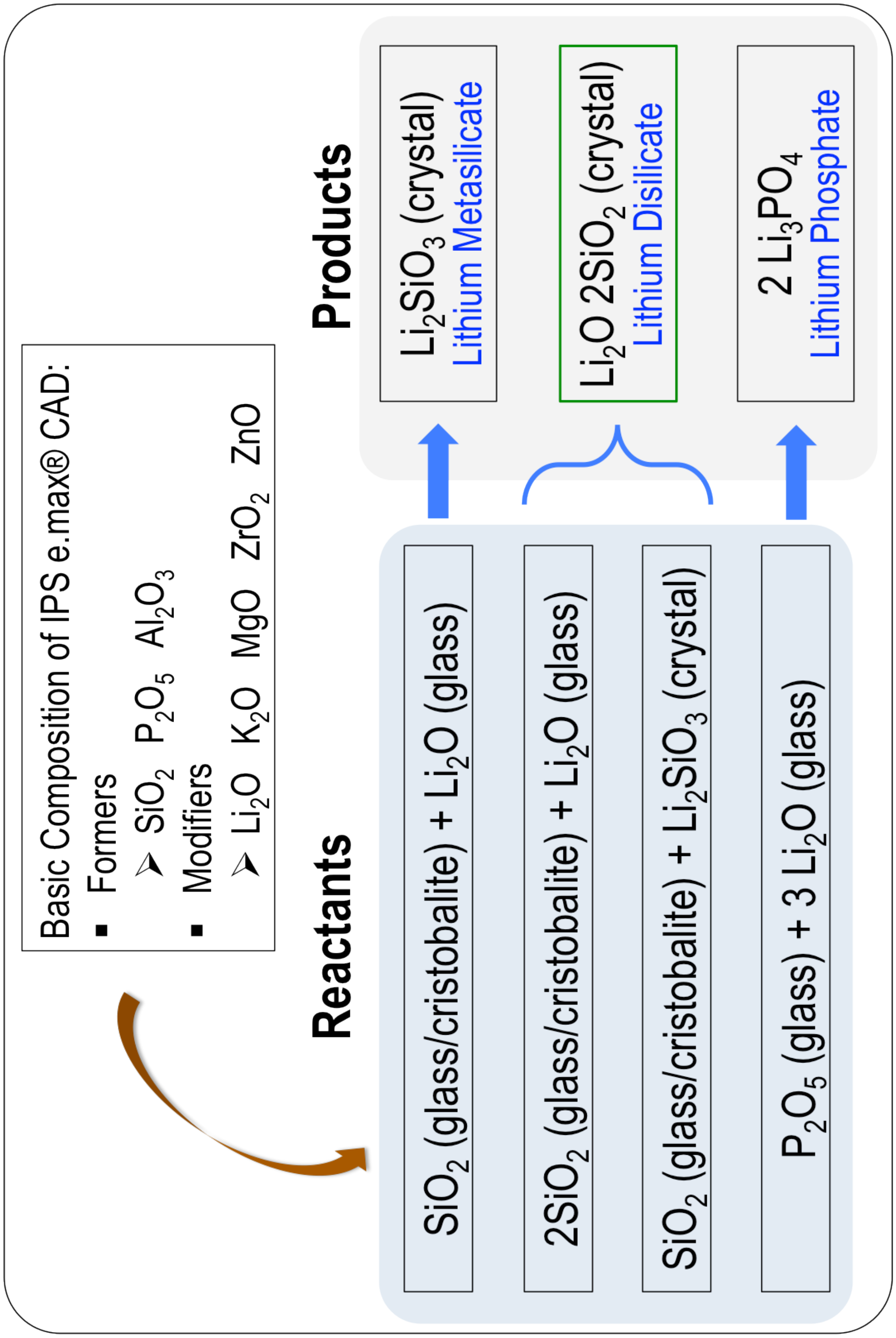

Figure 20: Possible reaction mechanisms when IPS e.mx® CAD is heat-treated.

10. References

[1] Carter B, Norton G. Ceramic materials: science and engineering. [S.l.]: Springer; 2012.
[2] Sakaguchi RL, Powers JM. Craig's restorative dental materials. St. Louis, Mo: Elsevier/Mosby; 2012.
[3] Kelly J. Dental ceramics: What is this stuff anyway? J Am Dent Assoc. 2008;139:4S-7S.
[4] Denry I, Holloway JA. Ceramics for Dental Applications: A Review. Materials. 2010;3:351-68.
[5] Griggs JA. Recent advances in materials for all-ceramic restorations. Dental Clinics of North America. 2007;51:713-27.
[6] Zachariasen WH. The atomic arrangement in glass. Journal of the American Chemical Society. 1932;54:3841-51.
[7] Kelly J. Dental ceramics: current thinking and trends. Dental Clinics of North America. 2004;48:513-30.
[8] Chen X, Chadwick TC, Wilson RM, Hill R, Cattell MJ. Crystallization of High-strength Fine-sized Leucite Glass-ceramics. Journal of Dental Research. 2010;89:1510-6.
[9] Zhang Y, Rao P, Lu M, Wu J. Mechanical properties of dental porcelain with different leucite particle sizes. Journal of the American Ceramic Society. 2008;91:527-34.
[10] Tinschert J, Zwez D, Marx R, Anusavice KJ. Structural reliability of alumina-, feldspar-, leucite-, mica- and zirconia-based ceramics. Journal of Dentistry. 2000;28:529-35.
[11] Conrad HJ, Seong W-J, Pesun GJ. Current ceramic materials and systems with clinical recommendations: A systematic review. Journal of Prosthetic Dentistry. 2007;98:389-404.
[12] Odén A, Andersson M, Krystek-Ondracek I, Magnusson D. Five-year clinical evaluation of Procera AllCeram crowns. The Journal of Prosthetic Dentistry. 1998;80:450-6.
[13] Höland W, Beall G. Glass-ceramic technology. Hoboken, N.J.: Wiley: American Ceramic Society; 2012.
[14] Holand W, Schweiger M, Watzke R, Peschke A, Kappert H. Ceramics as biomaterials for dental restoration. Expert Review of Medical Devices. 2008;5:729-45.
[15] Guazzato M, Albakry M, Ringer SP, Swain MV. Strength, fracture toughness and microstructure of a selection of all-ceramic materials. Part I. Pressable and alumina glass-infiltrated ceramics. Dental Materials. 2004;20:441-8.
[16] Tinschert J, Natt G, Mautsch W, Augthun M, Spiekermann H. Fracture resistance of lithium disilicate-, alumina-, and zirconia-based three-unit fixed partial dentures: A laboratory study. International Journal of Prosthodontics. 2001;14:231-8.
[17] Albakry M, Guazzato M, Swain MV. Fracture toughness and hardness evaluation of three pressable all-ceramic dental materials. Journal of Dentistry. 2003;31:181-8.
[18] Albakry M, Guazzato M, Swain MV. Biaxial flexural strength, elastic moduli, and x-ray diffraction characterization of three pressable all-ceramic materials. Journal of Prosthetic Dentistry. 2003;89:374-80.
[19] Gao J, Chen J-h, Wang F, Deng Z-x, Li F, Wu D. Effect of Heat-Pressing on the Microstructure and Properties of a Novel Lithium Disilicate Glass-ceramic. Advanced Materials Research. 2011;177:441-6.
[20] Della Bona A, Kelly JR. The clinical success of all-ceramic restorations. J Am Dent Assoc. 2008;139:8S-13S.
[21] Goodacre CJ, Bernal G, Rungcharassaeng K, Kan JYK. Clinical complications in fixed prosthodontics. Journal of Prosthetic Dentistry. 2003;90:31-41.
[22] Kern M, Sasse M, Wolfart S. Ten-year outcome of three-unit fixed dental prostheses made from monolithic lithium disilicate ceramic. J Am Dent Assoc. 2012;143:234-40.
[23] Valenti M, Valenti A. Retrospective survival analysis of 261 lithium disilicate crowns in a private general practice. Quintessence Int. 2009;40:573-9.

[24] Gehrt M, Wolfart S, Rafai N, Reich S, Edelhoff D. Clinical results of lithium-disilicate crowns after up to 9 years of service. Clin Oral Invest. 2013;17:275-84.

[25] Stookey SD. Catalyzed Crystallization of Glass in Theory and Practice. Industrial & Engineering Chemistry. 1959;51:805-8.

[26] Höland W, Apel E, van 't Hoen C, Rheinberger V. Studies of crystal phase formations in high-strength lithium disilicate glass–ceramics. Journal of Non-Crystalline Solids. 2006;352:4041-50.

[27] Höland W, Frank M, Rheinberger V. Surface crystallization of leucite in glasses. Journal of Non-Crystalline Solids. 1995;180:292-307.

[28] Höland W, Rheinberger V, Apel E, van't Hoen C. Principles and phenomena of bioengineering with glass-ceramics for dental restoration. Journal of the European Ceramic Society. 2007;27:1521-6.

[29] Zheng X, Wen G, Song L, Huang XX. Effects of P2O5 and heat treatment on crystallization and microstructure in lithium disilicate glass ceramics. Acta Materialia. 2008;56:549-58.

[30] Beall G. Design and properties of glass-ceramics. Annual Review of Materials Science. 1992;22:91-119.

[31] Xiao Z, Zhou J, Wang Y, Luo M. Microstructure and Properties of Li2O-Al2O3-SiO2-P2O5 Glass-Ceramics. Open Materials Science Journal. 2011;5:45-50.

[32] Headley TJ, Loehman RE. Crystallization of a glass-ceramic by epitaxial growth. Journal of the American Ceramic Society. 1984;67:620-5.

[33] Borom MP, Turkalo AM, Doremus RH. Strength and Microstructure in Lithium Disilicate Glass-Ceramics. Journal of the American Ceramic Society. 1975;58:385-91.

[34] Bischoff C, Eckert H, Apel E, Rheinberger VM, Holand W. Phase evolution in lithium disilicate glass-ceramics based on non-stoichiometric compositions of a multi-component system: structural studies by 29Si single and double resonance solid state NMR. Physical Chemistry Chemical Physics. 2011;13:4540-51.

[35] Scientific Documentation IPS e.max® CAD. In: Ivoclar Vivadent AG RD, editor. FL-9494 Schaan, Liechtenstein 2005.

[36] Chen X, Chadwick TC, Wilson RM, Hill RG, Cattell MJ. Crystallization and flexural strength optimization of fine-grained leucite glass-ceramics for dentistry. Dental Materials. 2011;27:1153-61.

[37] Denry IL, Mackert JR, Holloway JA, Rosenstiel SF. Effect of cubic leucite stabilization on the flexural strength of feldspathic dental porcelain. Journal of Dental Research. 1996;75:1928-35.

[38] Burgner LL, Lucas P, Weinberg MC, Soares PC, Zanotto ED. On the persistence of metastable crystal phases in lithium disilicate glass. Journal of Non-Crystalline Solids. 2000;274:188-94.

[39] Deubener J, Bruckner R, Sternitzke M. Induction time analysis of nucleation and crystal growth in di- and metasilicate glasses. Journal of Non-Crystalline Solids. 1993;163:1-12.

[40] Iqbal Y, Lee WE, Holland D, James PF. Metastable phase formation in the early stage crystallisation of lithium disilicate glass. Journal of Non-Crystalline Solids. 1998;224:1-16.

[41] Soares PC, Zanotto ED, Fokin VM, Jain H. TEM and XRD study of early crystallization of lithium disilicate glasses. Journal of Non-Crystalline Solids. 2003;331:217-27.

[42] Zanotto ED. Metastable phases in lithium disilicate glasses. Journal of Non-Crystalline Solids. 1997;219:42-8.

[43] Wen G, Zheng X, Song L. Effects of P2O5 and sintering temperature on microstructure and mechanical properties of lithium disilicate glass-ceramics. Acta Materialia. 2007;55:3583-91.

[44] Huang SF, Zhang B, Huang ZH, Gao W, Cao P. Crystalline phase formation, microstructure and mechanical properties of a lithium disilicate glass-ceramic. J Mater Sci. 2013;48:251-7.

[45] ISO 6872: 2008(E) Dentistry - Ceramic Materials, 3rd Ed. Geneva, Switzerland International Organization for Standardization; 2008.

[46] Oliver WC, Pharr GM. Improved technique for determining hardness and elastic modulus using load and displacement sensing indentation experiments. Journal of Materials Research. 1992;7:1564-83.

[47] Schmelzer JWP, Potapov OV, Fokin VM, Muller R, Reinsch S. The effect of elastic stress and relaxation on crystal nucleation in lithium disilicate glass. Journal of Non-Crystalline Solids. 2004;333:150-60.

[48] Albakry M, Guazzato M, Swain MV. Biaxial flexural strength and microstructure changes of two recycled pressable glass ceramics. Journal of prosthodontics. 2004;13:141-9.

[49] Della Bona A, Mecholsky JJ, Jr., Anusavice KJ. Fracture behavior of lithia disilicate- and leucite-based ceramics. Dental materials : official publication of the Academy of Dental Materials. 2004;20:956-62.

[50] Kissinger HE. Reaction kinetics in differential thermal analysis. Analytical chemistry. 1957;29:1702-6.

[51] Ozawa T. Kinetics of non-isothermal crystallization. Polymer. 1971;12:150-8.

[52] Matusita K, Sakka S. Kinetic study on non-isothermal crystallization of glass by thermal analysis. Bulletin of the Institute for Chemical Research, Kyoto University. 1981;59:159-71.

[53] Xingzhong G, Wenyan L, Hui Y, Jiajie Z, Wenda Z. Effect of Neodymium on the Crystallization, Microstructure and Colorization of Li2O-Al2O3-SiO2 Glass Ceramics. New Journal of Glass and Ceramics. 2012;2:98-103.

[54] Spurr RA, Myers H. Quantitative Analysis of Anatase-Rutile Mixtures with an X-Ray Diffractometer. Analytical chemistry. 1957;29:760-2.

[55] Höland W, Rheinberger V, Schweiger M. Control of nucleation in glass ceramics. Philosophical Transactions of the Royal Society of London Series A: Mathematical, Physical and Engineering Sciences. 2003;361:575-89.

[56] Hasselman DPH, Fulrath RM. Proposed Fracture Theory of a Dispersion-Strengthened Glass Matrix. Journal of the American Ceramic Society. 1966;49:68-72.

[57] El-Meliegy E, Noort R. Lithium Disilicate Glass Ceramics. Glasses and Glass Ceramics for Medical Applications: Springer New York; 2012. p. 209-18.

[58] Iqbal Y, Lee WE, Holland D, James PF. Crystal nucleation in P2O5-doped lithium disilicate glasses. J Mater Sci. 1999;34:4399-411.

[59] Seghi RR, Denry IL, Rosenstiel SF. Relative fracture toughness and hardness of new dental ceramics. The Journal of Prosthetic Dentistry. 1995;74:145-50.

[60] Pinckney LR, Beall GH. Microstructural evolution in some silicate glass-ceramics: A review. Journal of the American Ceramic Society. 2008;91:773-9.

[61] Huang S, Cao P, Li Y, Huang Z, Gao W. Nucleation and Crystallization Kinetics of a Multicomponent Lithium Disilicate Glass by in Situ and Real-Time Synchrotron X-ray Diffraction. Crystal Growth & Design. 2013;13:4031-8.

[62] Anusavice KJ. Standardizing failure, success, and survival decisions in clinical studies of ceramic and metal-ceramic fixed dental prostheses. Dental Materials. 2012;28:102-11.

[63] Kelly J. Clinically relevant approach to failure testing of all-ceramic restorations. Journal of Prosthetic Dentistry. 1999;81:652-61.

11. Curriculum Vitae

WEN LIEN

PROFESSIONAL DENTAL LICENSURE

Dental Licensure	State of Oregon	2001 – Present
Dental Licensure	State of Texas	2010 – Present

PROFESSIONAL EXPERIENCE

Assistant Professor, Uniformed Services University of the Health Sciences United States Air Force Postgraduate Dental School, Dental Crop	1/2010 – 6/2012
Dental Researcher, Dental and Trauma Research Detachment Institute of Surgical Research, United States Army	10/2009 – 6/2012
Comprehensive General Dentist, Lackland Dental Clinic 59th Medical Wing, United States Air Force, Dental Corp	7/2007 – 6/2012
General Dentist, Wright-Patterson Dental Clinic 88th Air Base Wing, United States Air Force, Dental Corp	8/2006 – 5/2007
General Dentist, Hanscom Dental Clinic 66th Air Base Wing, United States Air Force, Dental Corp	9/2004 – 8/2006
General Dentist, Yokota Dental Clinic 374th Airlift Wing, United States Air Force, Dental Corp	6/2001 – 8/2004

EDUCATION

Indiana University Indianapolis, Indiana (USAF Sponsored Fellowship)	Dental Materials	MS	May 2014
USAF Wilford Hall Medical Center Join-Base, San Antonio, Texas	General Dentistry Residency	Certificate	7/2007 – 6/2009
Case Western Reserve University Cleveland, Ohio (USAF HPSP Scholarship)	Dental Medicine	DMD	May 2001
University of Minnesota Twin Cities Minneapolis/ST Paul, Minnesota	Medical Physics	MS	May 1996
University of California Irvine Irvine, California	Chemistry	BS	June 1994

MILITARY EDUCATION

Air Command & Staff College (By Correspondence)	April 2007
Squadron Officer School (By Correspondence)	June 2004
Officer Training School (Maxwell AFB, Alabama)	July 2001

PUBLICATION

Journals

- Lien W, VanDeWalle KS. Physical Properties of a New Silorane-Based Restorative System. Dent Mater 2010; 26(4): 337-44.
- Hamilton M, Roberts HW, VanDeWalle KS, Hamilton G, Lien W. Microtomographic Porosity Determination in Alginate Mixed with Various Methods. J Prosthodont 2010; 19(6): 478-81.
- Blackham J, VanDeWalle KS, Lien W. Properties of Hybrid Resin Composite Systems Containing Prepolymerized Filler Particles. Oper Dent 2009; 34(6): 697-702.
- Geise RA, Schueler BA, Lien W, Jones SC. Suitability of laser stimulated TLD arrays as patient dose monitors in high dose x-ray imaging. Med Phys 1997; 24(10): 1643-6.
- Lien W, Geise RA. Temperature response of two photographic films and TLDs suitable for patient dosimetry of high dose fluoroscopic procedures. Health Phys 1997; 73(3): 483-7.

Conferences & Presentations

- Lien W, Roberts HW, Chu TG. Optimization of Crystalline Kinetics, Thermal Processing, and Strength of a Dental Lithium Disilicate Glass-Ceramic. Presented at AADR, Charlotte, NC, 2014.
- Connor JO, Lien W, Meyers EJ, Vandewalle KS. Effect of Surface Treatments on Mechanical Properties of Desiccated Glass-Ionomers. Presented at AADR, Charlotte, NC, 2014.
- Chu TG, Lien W, Liu WC, Bennett JD, Patel R, Smith T, Voytik-Harbin SL, Goebel WS. Stem Cells Loaded 3D Scaffolds for Craniofacial Bone Repair. Presented at AADR, Charlotte, NC, 2014.
- Lien W, Chu TG, Li D, Liu WC, Campbell AL. Microstructural Evolution and Physical Behavior of a Lithium Disilicate Glass-Ceramic. Presented at IADR, Seattle, WA, 2013.
- Ibarra ET, Lien W, Vandewalle KS, Casey JA, Dixon SA. Physical Properties of a New Sonically Activated Composite Restorative Material. Presented at IADR, Seattle, WA, 2013.
- Wilson BM, Lien W, Lincoln TA, and Vandewalle KS. Post-Irradiation Polymerization of a Silorane-Based Composite. Presented at IADR, Seattle, WA, 2013.
- Dickson WJ, Lien W, Vandewalle KS, Kim EK, Dixon SA, Summitt JB. Effects of Cyclic Loading and Toothbrush Abrasion on Cervical-Lesion Formation. Presented at AADR, Tampa, FL, 2012.
- Presicci A, Lien W, Vandewalle KS, Harding AB. Microtomographic Evaluation of Porosity Formation in Composite Restorations. Presented at AADR, Tampa, FL, 2012.
- Stoy AJ, Lien W, Vandewalle KS, Speck SH, Sabey KA. Physical Properties of Newer Glass-Ionomer Restorative Materials. Presented at AADR Tampa, FL, 2012.
- Dickson PL, Lien W, Vandewalle KS, Wajdowicz MN, Santos MD. Effects of Pre-heating on the Properties of a Silorane-Based Composite. Presented at AADR Tampa, FL, 2012.
- Lien W, Ong ES, VanDeWalle KS. Effect of High-Heat Storage on the Properties of Composite Resin. Presented at IADR, San Diego, CA, 2011.
- Brown Baer PR, Silliman DT, Guda T, Lien W, Hale RG. Clinical Modeling for Lateral Mandibular Body Reconstruction: Initial Results from a Pig Mandible Model. Presented at Military Health System Research Symposium, Fort Lauderdale, FL, 2012.
- Hines JD, Lien W, Brown Baer PR, Silliman DT, Hale RG. Clinical Modeling for Lateral Mandibular Body Reconstruction: Goat versus Pig. Paper presented at Armed Forces Institute of Regenerative Medicine (AFIRM) All Hands, Clearwater, FL, 2011.
- Lien W, VanDeWalle KS. Properties of a composite resin with new monomer technology. Presented at AADR, Washington DC, 2010.
- Lien W, VanDeWalle KS. Mechanical Properties of a New Silorane-Based Restorative System. Presented at IADR, Miami, FL, 2009.
- Lien W. Molar Uprighting with a Mini-Screw Implant. Presented at the annual scientific meeting of Academy of Operative Dentistry, Chicago, IL, 2009.
- Lien W. New Dental Composites. Presenter for the continuing education at the University of Texas Health Science Center, San Antonio, TX, 2009.

- VanDeWalle KS, Lien W. Accuracy of a New Self-Calibrating Radiometer. Presented at IADR, Miami, FL, 2009.
- Hamilton M, Roberts HW, VanDeWalle KS, Hamilton G, Lien W. Microtomographic Porosity Determination in Alginate Mixed with Various Methods. Presented at IADR, Miami, FL, 2009.
- Douglas WH, Lien W, Nguyen TT, Ko CC, Pintado WR. Quantification of digital dental plaque indices using color transformation. J Dent Res 77(SI): 222, abstract #936, 1998. Presented at AADR, Minneapolis, MN, 1998.
- O'Dea TJ, Lien W, Lu H, Schueler BA, Geise RA. Use of an automated dosimetry system for analyzing dose reduction methods in neuroradiology. Presented at RSNA, Chicago, IL, 1996.
- Geise RA, Fajardo LC, Lien W, Ong HS. Sources of uncertainty in using fine grain film to determine skin dose in x-ray interventional procedures. Presented at AAPM, Boston, MA, 1995.

MILITARY PROMOTION

Lieutenant Colonel	2011
Major	2005
Captain	2001
2nd Lieutenant	1999

AWARDS

USAF Dental Materials Fellowship Scholarship	2012 – 2014
USAF Meritorious Service Medal	2012
USAF Commendation Medal (Two Devices)	2007
USAF Achievement Medal	2003
USAF Health Professional Scholarship	1998 – 2001
Graduate Research Assistantship, University of Minnesota	1994 – 1997
Graduate Scholarship, University of Minnesota	1994 – 1997
Bank of America Computer Science Scholarship	1990

PROFESSIONAL AFFILIATIONS

Academy of General Dentistry
American Dental Association
American Association of Physicists in Medicine (1996 – 1997)